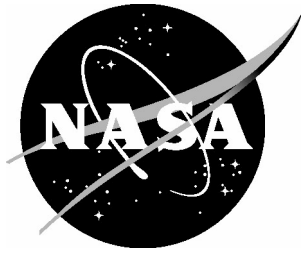


NASA/CR-2005-213748



# Motion Cueing Algorithm Development: Piloted Performance Testing of the Cueing Algorithms

*Robert J. Telban and Frank M. Cardullo  
State University of New York, Binghamton, New York*

*Lon C. Kelly  
Unisys Corporation, Hampton, Virginia*

---

May 2005

## The NASA STI Program Office . . . in Profile

Since its founding, NASA has been dedicated to the advancement of aeronautics and space science. The NASA Scientific and Technical Information (STI) Program Office plays a key part in helping NASA maintain this important role.

The NASA STI Program Office is operated by Langley Research Center, the lead center for NASA's scientific and technical information. The NASA STI Program Office provides access to the NASA STI Database, the largest collection of aeronautical and space science STI in the world. The Program Office is also NASA's institutional mechanism for disseminating the results of its research and development activities. These results are published by NASA in the NASA STI Report Series, which includes the following report types:

- **TECHNICAL PUBLICATION.** Reports of completed research or a major significant phase of research that present the results of NASA programs and include extensive data or theoretical analysis. Includes compilations of significant scientific and technical data and information deemed to be of continuing reference value. NASA counterpart of peer-reviewed formal professional papers, but having less stringent limitations on manuscript length and extent of graphic presentations.
- **TECHNICAL MEMORANDUM.** Scientific and technical findings that are preliminary or of specialized interest, e.g., quick release reports, working papers, and bibliographies that contain minimal annotation. Does not contain extensive analysis.
- **CONTRACTOR REPORT.** Scientific and technical findings by NASA-sponsored contractors and grantees.

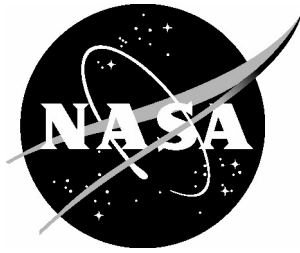
- **CONFERENCE PUBLICATION.** Collected papers from scientific and technical conferences, symposia, seminars, or other meetings sponsored or co-sponsored by NASA.
- **SPECIAL PUBLICATION.** Scientific, technical, or historical information from NASA programs, projects, and missions, often concerned with subjects having substantial public interest.
- **TECHNICAL TRANSLATION.** English-language translations of foreign scientific and technical material pertinent to NASA's mission.

Specialized services that complement the STI Program Office's diverse offerings include creating custom thesauri, building customized databases, organizing and publishing research results ... even providing videos.

For more information about the NASA STI Program Office, see the following:

- Access the NASA STI Program Home Page at <http://www.sti.nasa.gov>
- E-mail your question via the Internet to [help@sti.nasa.gov](mailto:help@sti.nasa.gov)
- Fax your question to the NASA STI Help Desk at (301) 621-0134
- Phone the NASA STI Help Desk at (301) 621-0390
- Write to:  
NASA STI Help Desk  
NASA Center for AeroSpace Information  
7121 Standard Drive  
Hanover, MD 21076-1320

NASA/CR-2005-213748



# Motion Cueing Algorithm Development: Piloted Performance Testing of the Cueing Algorithms

*Robert J. Telban and Frank M. Cardullo  
State University of New York, Binghamton, New York*

*Lon C. Kelly  
Unisys Corporation, Hampton, Virginia*

National Aeronautics and  
Space Administration

Langley Research Center  
Hampton, Virginia 23681-2199

Prepared for Langley Research Center  
under Purchase Order L70823D

May 2005

## **Acknowledgments**

Jacob Houck of the Flight Simulation and Software Branch at the NASA Langley Research Center assisted in the preparation of this report.

Available from:

NASA Center for AeroSpace Information (CASI)  
7121 Standard Drive  
Hanover, MD 21076-1320  
(301) 621-0390

National Technical Information Service (NTIS)  
5285 Port Royal Road  
Springfield, VA 22161-2171  
(703) 605-6000

## **Abstract**

The relative effectiveness in simulating aircraft maneuvers with both current and newly developed motion cueing algorithms was assessed with an eleven-subject piloted performance evaluation conducted on the NASA Langley Visual Motion Simulator (VMS). In addition to the current NASA adaptive algorithm, two new cueing algorithms were evaluated: the optimal algorithm and the nonlinear algorithm. The test maneuvers included a straight-in approach with a rotating wind vector, an offset approach with severe turbulence and an on/off lateral gust that occurs as the aircraft approaches the runway threshold, and a takeoff both with and without engine failure after liftoff. The maneuvers were executed with each cueing algorithm with added visual display delay conditions ranging from zero to 200 msec.

Two methods, the quasi-objective NASA Task Load Index (TLX), and power spectral density analysis of pilot control, were used to assess pilot workload. Piloted performance parameters for the approach maneuvers, the vertical velocity upon touchdown and the runway touchdown position, were also analyzed but did not show any noticeable difference among the cueing algorithms. TLX analysis reveals, in most cases, less workload and variation among pilots with the nonlinear algorithm. Control input analysis shows pilot-induced oscillations on a straight-in approach were less prevalent compared to the optimal algorithm. The augmented turbulence cues increased workload on an offset approach that the pilots deemed more realistic compared to the NASA adaptive algorithm. The takeoff with engine failure showed the least roll activity for the nonlinear algorithm, with the least rudder pedal activity for the optimal algorithm.

This page intentionally left blank.

# Table of Contents

Abstract .....	iii
Table of Contents .....	v
List of Tables .....	vi
List of Figures .....	vii
1. Introduction.....	1
2. Background Information.....	3
2.1. NASA Langley Visual Motion Simulator (VMS) .....	3
2.2. Coordinated Adaptive Washout Algorithm .....	5
2.3. Optimal Algorithm.....	7
2.4. Nonlinear Algorithm.....	9
2.5. Nonlinear Input Scaling .....	11
2.6. Augmented Turbulence Cue .....	13
2.7. Pilot Tuning of the Cueing Algorithms .....	14
3. Test Procedure .....	19
4. Methods of Analysis .....	23
4.1. NASA Task Load Index (TLX) .....	23
4.2. Pilot Control Input Analysis .....	24
4.3. Simulator Coherence Analysis.....	25
5. Analysis Results.....	29
5.1. NASA Task Load Index.....	30
5.2. PSD Analysis .....	35
5.2.1. Straight-In Approach .....	35
5.2.2. Offset Approach.....	41
5.2.3. Takeoff without Engine Failure .....	47
5.2.4. Takeoff with Engine Failure .....	50
5.3. Simulator Attitude Coherence.....	54
6. Summary of Results.....	59
7. Conclusions.....	63
Appendix A. Pilot Test Runs and Conditions.....	67
Appendix B. Pilot Group Average PSD and Coherence.....	73
References.....	91

## List of Tables

Table 2.1. Nonlinear Gain Coefficients for the Cueing Algorithms.....	17
Table 5.1. Pilot Groups by Control Technique and Instrument Scan Pattern.....	29

## List of Figures

Figure 2.1. NASA Langley Visual Motion Simulator (VMS). NASA Langley Research Center, Hampton, Virginia.....	3
Figure 2.2. Visual Motion Simulator Cockpit. NASA Langley Research Center, Hampton, Virginia. ....	4
Figure 2.3. Coordinated Adaptive Washout (NASA Adaptive) Algorithm.....	5
Figure 2.4. Optimal Algorithm Implementation.....	8
Figure 2.5. Nonlinear Algorithm Implementation with Unity-Gain Pitch Filter.....	9
Figure 2.6. Nonlinear Input Scaling.....	12
Figure 2.7. Optimal Algorithm Vertical Mode with Augmented Turbulence Channel...	13
Figure 3.1. Schematic Diagram of Offset Approach Maneuver Flight Path. ....	20
Figure 4.1. Single-Degree-of-Freedom Manual Control System with Remnant.....	26
Figure 5.1. TLX for Approach Maneuvers by Pilot Group with No Delay.....	31
Figure 5.2. TLX for Takeoff Maneuvers by Pilot Group with No Delay.....	32
Figure 5.3. TLX for Approach Maneuvers with Delay, Pilot Groups 1 and 2. ....	33
Figure 5.4. TLX for Takeoff Maneuvers with Delay, Pilot Groups 1 and 2. ....	34
Figure 5.5. Straight-In Approach, Control Input Integral Power, Pilot Group 1.....	35
Figure 5.6. Straight-In Approach, Aircraft Angle Average PSD with Zero Delay, Pilot Group 1. ....	36
Figure 5.7. Straight-In Approach, Control Input Integral Power, Pilot Group 2.....	37
Figure 5.8. Straight-In Approach, Aircraft Angle Average PSD with Zero Delay, Pilot Group 2. ....	38
Figure 5.9. Straight-In Approach, Vertical Rate at Touchdown.....	39
Figure 5.10. Touchdown Coordinates, Straight-In Approach, Pilot Group 1.....	40
Figure 5.11. Touchdown Coordinates, Straight-In Approach, Pilot Group 2.....	40
Figure 5.12. Offset Approach, Control Input Integral Power, Pilot Group 1. ....	41
Figure 5.13. Offset Approach, Aircraft Angle Average PSD, Pilot Group 1 with Zero Delay.....	42
Figure 5.14. Offset Approach, Control Input Integral Power, Pilot Group 2. ....	43
Figure 5.15. Offset Approach, Vertical Rate at Touchdown. ....	44
Figure 5.16. Touchdown Coordinates, Offset Approach, Pilot Group 1. ....	45
Figure 5.17. Touchdown Coordinates, Offset Approach, Pilot Group 2. ....	45
Figure 5.18. Simulator Z-Axis Average PSD for Approach Maneuvers, Pilot Group 1. 46	
Figure 5.19. Takeoff without Engine Failure, Control Input Integral Power, Pilot Group 1.....	47
Figure 5.20. Takeoff without Engine Failure, Control Input Integral Power, Pilot Group 2.....	48
Figure 5.21. Takeoff without Engine Failure, Aircraft Roll and Track Angle Average PSD, Pilot Group 1. ....	49
Figure 5.22. Takeoff with Engine Failure, Control Input Integral Power, Pilot Group 1.....	50
Figure 5.23. Takeoff with Engine Failure, Control Input Integral Power, Pilot Group 2.....	51
Figure 5.24. Takeoff with Engine Failure, Rudder Pedal Integral Power. ....	52
Figure 5.25. Takeoff with Engine Failure, Aircraft Roll and Track Angle Average PSD, Pilot Group 1.....	54

Figure 5.26. Simulator Attitude Average PSD for Offset Approach, Pilot Group 1 with Zero Delay. ....	56
Figure 5.27. Simulator Average Coherence for Offset Approach, Pilot Group 1 with Zero Delay. ....	56
Figure 5.28. Simulator Attitude Average PSD for Takeoff with Engine Failure, Pilot Group 1 with Zero Delay. ....	57
Figure 5.29. Simulator Average Coherence for Takeoff with Engine Failure, Pilot Group 1 with Zero Delay. ....	57
Figure 7.1. NASA Langley Cockpit Motion Facility (CMF). ....	65

## 1. Introduction

The relative effectiveness in simulating aircraft maneuvers with various motion cueing algorithms was assessed with piloted behavior. Three motion cueing algorithms were evaluated: the current NASA adaptive algorithm [1], and the new optimal and nonlinear motion cueing algorithms. The new algorithms are described in the next section, with the theory and development discussed in greater detail in a separate report [2]. The optimal and nonlinear algorithms are also augmented with a vertical motion cue that is driven by the turbulence and is described in Section 2.6. The nonlinear gains for each degree-of-freedom were tuned with a simulator pilot executing a series of simulated maneuvers on the NASA Langley Visual Motion Simulator (VMS) described in Section 2.1. The outcome of this tuning process is discussed in Section 2.7.

A preliminary performance study of the adaptive and optimal algorithms was previously conducted on the VMS with a group of three pilots executing a set of simulated aircraft maneuvers [3]. The purpose of this current study is to assess the piloted behavior for a larger group of eleven pilots executing maneuvers under various flight conditions such as in-flight turbulence and engine failure with all three cueing algorithms on the VMS. In addition, each maneuver included additional test runs with varying computer image generator (visual) delay. A description of the maneuvers and test procedure is given in Section 3.

While most prior motion cueing evaluations have been based solely on the pilot's subjective evaluation of handling qualities, the pilot performance and workload in these tests were assessed with both a quasi-objective evaluation, the NASA Task Load Index (TLX) [4], and the objective analysis of pilot control inputs with the application of power

spectral density (PSD) frequency analysis. These evaluation techniques are discussed in greater detail in Section 4. In addition, other performance parameters such as the vertical velocity at touchdown and runway touchdown position relative to the runway centerline were investigated for the approach maneuvers. Analysis results for each maneuver showing pilot performance and workload as a function of both the cueing algorithm and the visual display delay are presented in Section 5.

The assumption here is that, in general, the lower the pilot workload for a given maneuver among cueing algorithms, the greater the information being transmitted by the simulator to the pilot. This holds true for aircraft maneuvers without disturbance inputs, where workload increases with increased maneuver complexity. However, with the addition of a disturbance (e.g., turbulence) and/or visual display delay to a maneuver, an increase in the pilot's workload is a function of increased, more realistic information transmitted from the motion cues to the pilot.

## 2. Background Information

### 2.1. NASA Langley Visual Motion Simulator (VMS)

The NASA Langley Visual Motion Simulator (VMS), shown in Figure 2.1, is a general-purpose flight simulator consisting of a two-crewmember cockpit mounted on a 60-inch stroke six-degree-of-freedom synergistic motion base [5], [6].



**Figure 2.1. NASA Langley Visual Motion Simulator (VMS). NASA Langley Research Center, Hampton, Virginia.**

Motion cues are provided in the simulator by the relative extension or retraction of the six hydraulic actuators of the motion base. The NASA adaptive algorithm and the new optimal and nonlinear algorithms were used to drive the motion base during the tuning of the new algorithms and the piloted test evaluation.

The cockpit of the VMS, shown in Figure 2.2, is designed to accommodate a generic transport aircraft configuration on the left side and a generic fighter or rotorcraft configuration on the right side. Both sides of the cockpit are outfitted with three heads-down CRT displays (primary flight display, navigation/map display, and engine display), a number of small standard electromechanical circular instruments and a landing gear handle mounted in the instrument panel. The left side contains a two-axis side stick control loader, and the right side contains a control loaded two-axis center stick. Both

sides contain control loaded rudder systems. The center aisle stand is outfitted with a control display unit, a four-lever throttle quadrant, a flap handle, a speed brake handle, and a slats handle. The cockpit is outfitted with four collimated window display systems to provide an out-the-window visual scene. During the piloted evaluations, the test subject flew from the left seat of the cockpit, while an observer/test conductor rode in the right seat.



**Figure 2.2. Visual Motion Simulator Cockpit. NASA Langley Research Center, Hampton, Virginia.**

The simulator includes a high fidelity, highly nonlinear mathematical model of a Boeing 757-200 aircraft, complete with landing gear dynamics, gust and wind models, flight management systems, and flight control computer systems. For this study, the test subjects flew the simulated aircraft in the manual control mode (without the autopilot), and with manual throttle control (without the autothrottle).

The out-the window visual scene is driven by an Evans and Sutherland ESIG 3000/GT computer generated image system. The visual database represented the Dallas/Fort Worth airport and its surrounding terrain. The study utilized runways 18L and 18R for approach maneuvers and runway 18R for takeoff maneuvers. The runways were equipped with approach lights, precision approach path indicator lights, runway

markings, and signage. The database included all runways and taxiways, and all airport structures and buildings. All tests were conducted in a daylight environment with full visibility.

## 2.2. Coordinated Adaptive Washout Algorithm

The intent of the NASA adaptive algorithm [1] is to adjust the response of the simulator washout filters in real time according to the current state of the simulator. The block diagram for this algorithm is shown in Figure 2.3. There are separate filtering channels for the translational and rotational degrees of freedom with a cross-feed path to provide the steady-state tilt coordination cues.

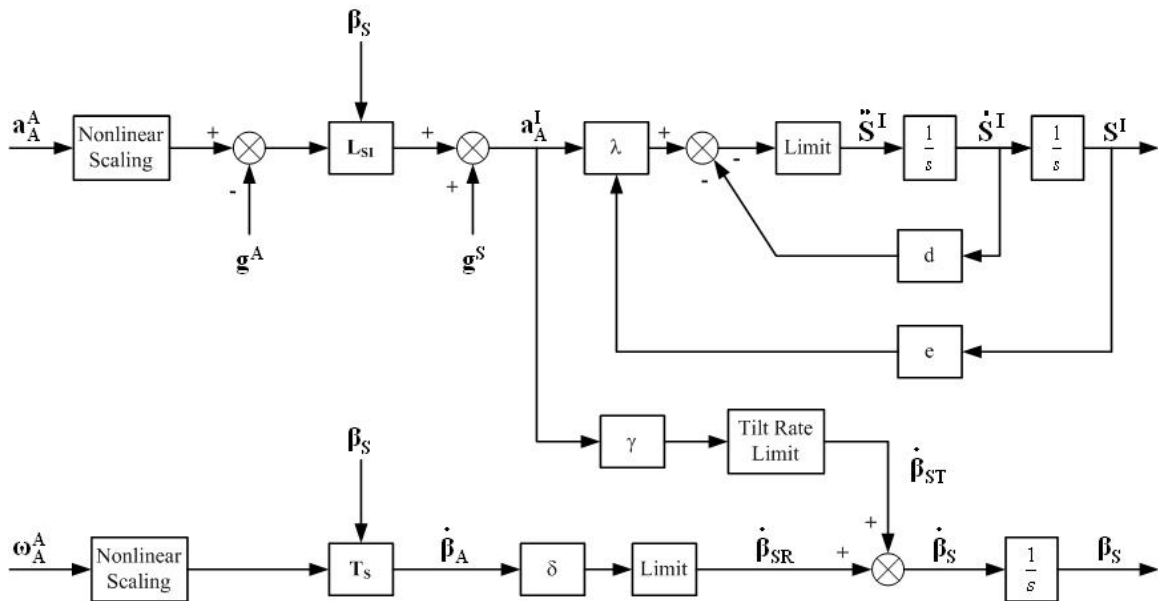


**Figure 2.3. Coordinated Adaptive Washout (NASA Adaptive) Algorithm.**

The aircraft acceleration vector  $\mathbf{a}_A^A$  is first transformed from the center of gravity of the aircraft to the motion base centroid. After nonlinear scaling and limiting, the gravity vector is subtracted to produce a simulator frame specific force vector. The simulator specific force is transformed from the simulator frame  $Fr_S$  into the inertial

frame  $Fr_1$ , resulting in the inertial specific force command  $\mathbf{f}_A^I$ . The specific force command  $\mathbf{f}_A^I$  is passed through a translational channel with a time-varying gain  $\lambda$  to produce a simulator translational acceleration command  $\ddot{\mathbf{S}}^I$ . This acceleration is integrated to produce the velocity  $\dot{\mathbf{S}}^I$ , which is then integrated to produce the simulator translational position command  $\mathbf{S}^I$ . Both the velocity and position commands are employed as feedback.

The aircraft angular velocity vector  $\boldsymbol{\omega}_A^A$  is limited and scaled similar to the translational channel, with the resulting vector being transformed to the Euler angular rate vector  $\dot{\boldsymbol{\beta}}_A$ . This vector is passed through the rotational channel with a time-varying gain  $\delta$  to produce the vector  $\dot{\boldsymbol{\beta}}_{SR}$ . The tilt coordination rate  $\dot{\boldsymbol{\beta}}_{ST}$  is formed from the acceleration  $\mathbf{a}_A^I$  being passed through the cross-feed channel with a fixed gain  $\gamma$ . The summation of  $\dot{\boldsymbol{\beta}}_{ST}$  and  $\dot{\boldsymbol{\beta}}_{SR}$  yields  $\dot{\boldsymbol{\beta}}_S$ , which is then integrated to generate  $\boldsymbol{\beta}_S$ , the simulator angular position command.

The control law for the longitudinal mode is given by the following expressions:

$$\begin{aligned}\ddot{S}_x^I &= \lambda_x f_{Ax}^I - d_x \dot{S}_x^I - e_x S_x^I \\ \dot{\theta}_S &= \gamma_x a_{Ax}^I + \delta_x \dot{\theta}_A,\end{aligned}\tag{2.1}$$

where  $d_x$ ,  $e_x$ , and  $\gamma_x$  are fixed parameters, and  $\lambda_x$  and  $\delta_x$  are the time-varying parameters that are continuously adjusted by steepest descent in an attempt to minimize the instantaneous value of the cost function. The cost function is defined as

$$J_x = \frac{1}{2} (f_{Ax}^I - \dot{S}_x^I)^2 + \frac{W_x}{2} (\dot{\theta}_A - \dot{\theta}_S)^2 + \frac{b_x}{2} (S_x^I)^2 + \frac{C_x}{2} (\dot{S}_x^I)^2,\tag{2.2}$$

where  $W_x$ ,  $b_x$ , and  $C_x$  are constant weights that penalize the difference in response between the aircraft and simulator, as well as restraining the translational velocity and displacement in the simulator.

### 2.3. Optimal Algorithm

The theory and development of the optimal algorithm is well discussed by Telban and Cardullo [2]. The problem is to determine a transfer function matrix  $\mathbf{W}(s)$  that relates the desired simulator motion input to the aircraft input such that a cost function constraining the pilot sensation error (between simulator and aircraft) is minimized. A mathematical model of the human vestibular system [2] is used in the filter development. The optimal algorithm generates the desired transfer functions  $\mathbf{W}(s)$  by an off-line program [2], which are then implemented on-line.  $\mathbf{W}(s)$  will relate the simulator commands to the aircraft states by  $\mathbf{u}_s = \mathbf{W}(s) \times \mathbf{u}_A$ . The block diagram for the on-line algorithm implementation is shown in Figure 2.4. Similar to the NASA adaptive algorithm [1], there are separate filtering channels for the translational and rotational degrees of freedom with the cross-feed path providing the tilt coordination cues.

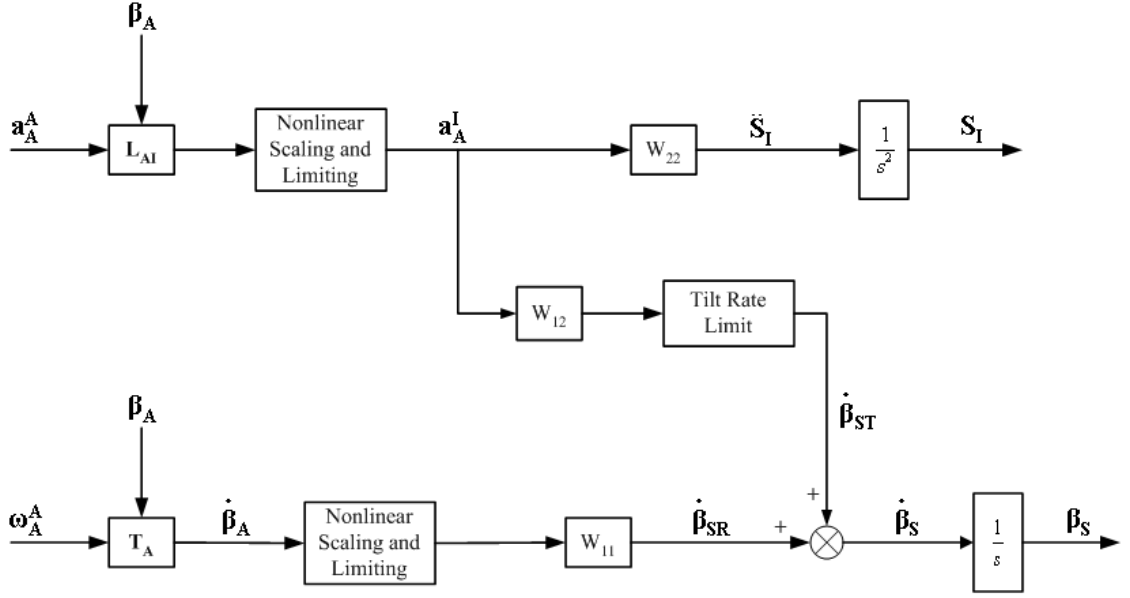


**Figure 2.4. Optimal Algorithm Implementation.**

The aircraft acceleration input vector is first transformed from the aircraft body frame  $Fr_A$  to the inertial frame  $Fr_I$ . Nonlinear scaling in combination with limiting as described in Section 2.5 is then applied to scale the aircraft inputs. The scaled inertial acceleration  $\mathbf{a}_A^I$  is then filtered through the translational filter  $W_{22}$  to produce a simulator translational acceleration command  $\ddot{\mathbf{S}}_I$ . This acceleration is integrated twice to produce the simulator translational position command  $\mathbf{S}_I$ .

The aircraft angular velocity input  $\boldsymbol{\omega}_A^A$  is transformed to the Euler angular rate vector  $\dot{\boldsymbol{\beta}}_A$ , and is limited and scaled similar to the translational channel. This input is then passed through the rotational filter  $W_{11}$  to produce the vector  $\dot{\boldsymbol{\beta}}_{SR}$ . The tilt coordination rate  $\dot{\boldsymbol{\beta}}_{ST}$  is formed from the acceleration  $\mathbf{a}_A^I$  being passed through the tilt coordination filter  $W_{12}$ . The summation of  $\dot{\boldsymbol{\beta}}_{ST}$  and  $\dot{\boldsymbol{\beta}}_{SR}$  yields  $\dot{\boldsymbol{\beta}}_S$ , which is then integrated to generate  $\boldsymbol{\beta}_S$ , the simulator angular position command.

## 2.4. Nonlinear Algorithm

The theory and development of the nonlinear algorithm is well discussed by Telban and Cardullo [2]. The algorithm is formulated as a linear optimal control problem similar to the optimal algorithm, but is also updated in real time with a nonlinear control law. Furthermore, it incorporates models of the human vestibular sensation system along with an integrated visual-vestibular perception model [2]. The block diagram for the on-line implementation is shown in Figure 2.5. Similar to the optimal algorithm, there are separate filtering channels for the translational and rotational degrees of freedom with the cross-feed path providing the tilt coordination cues. Telban and Cardullo [2] reported that for the pitch and roll rotational channels, no benefit resulted from updating the Riccati equation in real time; thus the nonlinear filters are replaced with unity-gain filters.

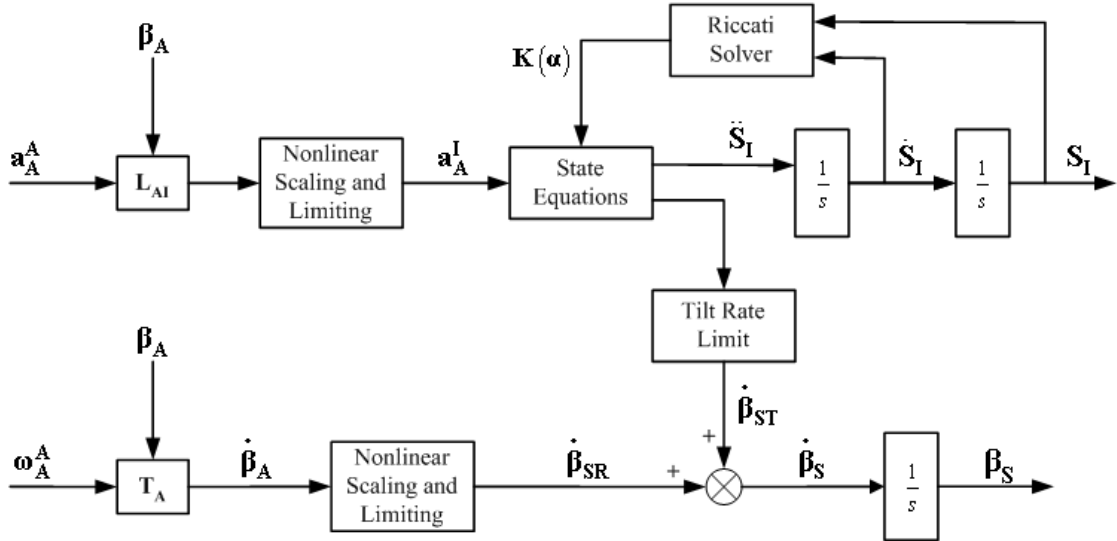


**Figure 2.5. Nonlinear Algorithm Implementation with Unity-Gain Pitch Filter.**

A nonlinear control law is implemented to generate a scalar coefficient  $\alpha$  that is a function of the simulator motion system states:

$$\alpha = \mathbf{x}_d^T \mathbf{Q}_2 \mathbf{x}_d, \quad (2.3)$$

where  $\mathbf{Q}_2$  is a weighting matrix that is at least positive semi-definite. As the computed system states increase in magnitude, i.e., with large commanded platform displacements and velocities,  $\alpha$  increases, resulting in faster control action to quickly wash out the platform to its neutral state. For small commands there will be limited control action, resulting in motion cues sustained for longer durations.

The solution of the algebraic Riccati equation is given as [2]

$$(\mathbf{A}' + \alpha\mathbf{I})^T \mathbf{P}(\alpha) + \mathbf{P}(\alpha)(\mathbf{A}' + \alpha\mathbf{I}) - \mathbf{P}(\alpha)\mathbf{B}\mathbf{R}_2^{-1}\mathbf{B}^T\mathbf{P}(\alpha) + \mathbf{R}'_1 = \mathbf{0}, \quad (2.4)$$

where  $\mathbf{A}'$  and  $\mathbf{B}$  are system matrices and  $\mathbf{R}'_1$  and  $\mathbf{R}_2$  are the standard optimal control weighting matrices defined by Telban and Cardullo [2] in the algorithm development. The system matrix  $\mathbf{A}'$  is augmented with  $\alpha$  times the identity matrix  $\mathbf{I}$ . The solution of Eq. (2.4) from the linear optimal algorithm that was computed off-line in MATLAB™ is used as the initial solution for the first time step. The Riccati equation of Eq. (2.4) is then updated in real time with a structured neural network developed by Ham and Collins [7] that is discussed in more detail by Telban and Cardullo [2].

The Riccati equation solution  $\mathbf{P}(\alpha)$  and the feedback matrix  $\mathbf{K}(\alpha)$  are partitioned corresponding to the partition of the state vector  $\mathbf{x}$  [2]:

$$\begin{aligned} \mathbf{K}_1(\alpha) &= \mathbf{R}_2^{-1} \left[ \mathbf{B}_v^T \mathbf{P}_{11} + \mathbf{B}_d^T \mathbf{P}_{21} + \mathbf{D}_v^T \mathbf{Q} \mathbf{C}_v \right] \\ \mathbf{K}_2(\alpha) &= \mathbf{R}_2^{-1} \left[ \mathbf{B}_v^T \mathbf{P}_{12} + \mathbf{B}_d^T \mathbf{P}_{22} \right] \\ \mathbf{K}_3(\alpha) &= \mathbf{R}_2^{-1} \left[ \mathbf{B}_v^T \mathbf{P}_{13} + \mathbf{B}_d^T \mathbf{P}_{23} - \mathbf{D}_v^T \mathbf{Q} \mathbf{C}_v \right], \end{aligned} \quad (2.5)$$

where the matrices  $\mathbf{B}_v$ ,  $\mathbf{B}_d$ , and  $\mathbf{D}_v \mathbf{Q} \mathbf{C}_v$  are defined by Telban and Cardullo [2], and by symmetry,  $\mathbf{P}_{12} = \mathbf{P}_{21}^T$ . The resulting state equations are then computed in real time:

$$\begin{bmatrix} \dot{\mathbf{x}}_e \\ \dot{\mathbf{x}}_d \end{bmatrix} = \begin{bmatrix} \mathbf{A}_v - \mathbf{B}_v \mathbf{K}_1(\alpha) & -\mathbf{B}_v \mathbf{K}_2(\alpha) \\ -\mathbf{B}_d \mathbf{K}_1(\alpha) & \mathbf{A}_d - \mathbf{B}_d \mathbf{K}_2(\alpha) \end{bmatrix} \begin{bmatrix} \mathbf{x}_e \\ \mathbf{x}_d \end{bmatrix} + \begin{bmatrix} -\mathbf{B}_v (\mathbf{I} + \mathbf{K}_3(\alpha)) \\ -\mathbf{B}_d \mathbf{K}_3(\alpha) \end{bmatrix} \mathbf{u}_A, \quad (2.6)$$

with the matrices  $\mathbf{A}_v$  and  $\mathbf{A}_d$  defined by Telban and Cardullo [2].

For each motion cueing algorithm, the simulator translational position  $\mathbf{S}^I$  and the angular position  $\boldsymbol{\beta}_s$  are used to transform the simulator motion from degree-of-freedom space to actuator space [2], generating the actuator commands required to achieve the desired platform motion.

## 2.5. Nonlinear Input Scaling

Limiting and scaling are applied to both aircraft translational input signals  $\mathbf{a}_A^A$  and rotational input signals  $\boldsymbol{\omega}_A^A$ . Limiting and scaling modify the amplitude of the input uniformly across all frequencies. Limiting is a nonlinear process that clips the signal so that it is limited to be less than a given magnitude. Limiting and scaling can be used to reduce the motion response of a flight simulator. A third-order polynomial scaling was developed [8] and has been implemented in the new simulator motion cueing algorithms.

When the magnitude of the input to the simulator motion system is small, the gain is desired to be relatively high, or the output will be below the pilot's perception threshold. When the magnitude of input is high, the gain is desired to be relatively low or the simulator may attempt to go beyond the hardware limits. Let us define the input as  $x$  and the output as  $y$ . Now define  $x_{\max}$  as the expected maximum input and  $y_{\max}$  as the maximum output, and  $s_0$  and  $s_1$  as the slopes at  $x = 0$  and  $x = x_{\max}$  respectively. Four desired characteristics for the nonlinear scaling are expressed as:

- (1)  $x = 0 \Rightarrow y = 0$ ,
- (2)  $x = x_{\max} \Rightarrow y = y_{\max}$ ,
- (3)  $y'|_{x=0} = s_0$ ,
- (4)  $y'|_{x=x_{\max}} = s_1$ ,

A third-order polynomial is then employed to provide functions with all the desired characteristics. This polynomial will be of the form

$$y = c_3x^3 + c_2x^2 + c_1x + c_0 \quad (2.7)$$

where

$$\begin{aligned} c_0 &= 0, \\ c_1 &= s_0, \\ c_2 &= x_{\max}^{-2} (3y_{\max} - 2s_0x_{\max} - s_1x_{\max}), \\ c_3 &= x_{\max}^{-3} (s_0x_{\max} - 2y_{\max} + s_1x_{\max}). \end{aligned}$$

One example of this polynomial gain is shown in Figure 2.6, with parameters set as

$$x_{\max} = 10, \quad y_{\max} = 6, \quad s_0 = 1.0, \quad s_1 = 0.1.$$

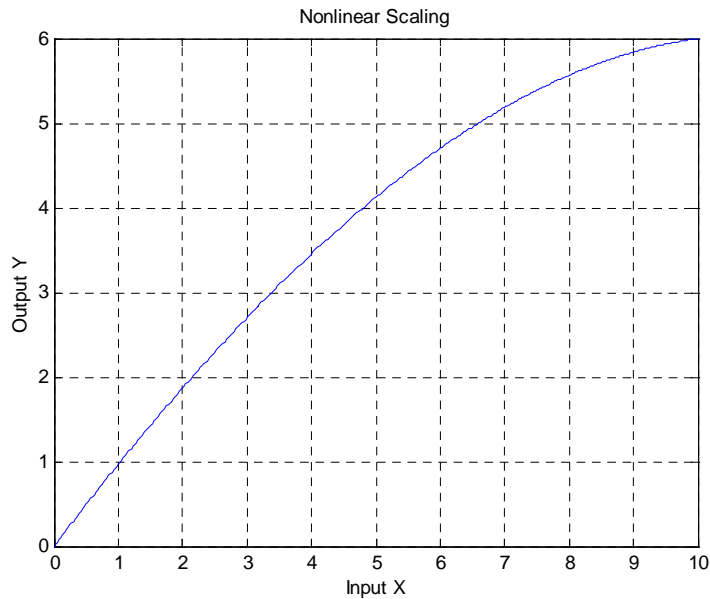


**Figure 2.6. Nonlinear Input Scaling.**

## 2.6. Augmented Turbulence Cue

Reid and Robinson [9] first addressed the problem of producing acceptable motion cues to turbulent gust inputs. They noted that heave is the most critical cue in representing turbulence, but is also the most restricted cue when constraining motion within the platform geometry. To overcome this limitation, they developed an approach in which a second set of aircraft equations of motion driven only by the turbulence inputs is employed. The output from this augmented channel is then added to the output from the primary flight equations, being driven by both turbulence and the pilot control inputs, before serving as input to the motion system. A similar approach to that developed by Reid and Robinson [9] has been implemented and is shown in Figure 2.7.

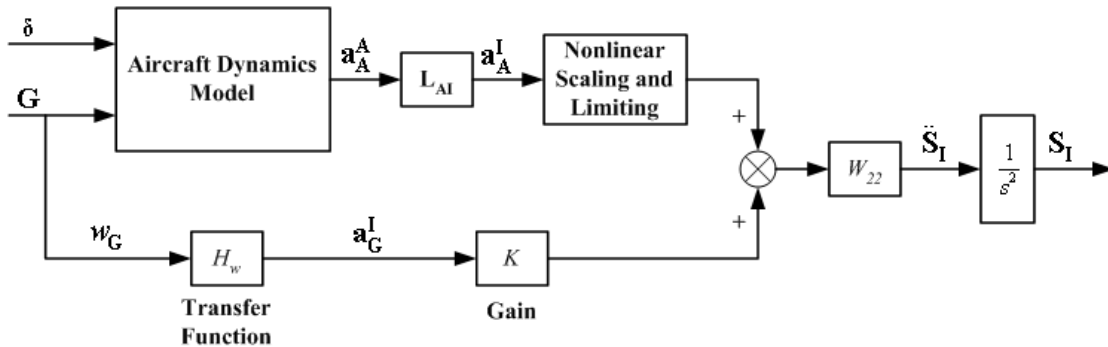


**Figure 2.7. Optimal Algorithm Vertical Mode with Augmented Turbulence Channel.**

The input to the augmented channel is the z-axis component  $w_G$  of the turbulence vector  $\mathbf{G}$ . Reid and Robinson showed that  $w_G$  is the dominant turbulence component needed in producing vertical acceleration due to turbulence. The secondary equations of motion can then be represented by a transfer function  $H_G(s)$ . The secondary acceleration  $\mathbf{a}_G^I$  is then scaled with a constant gain  $K_G$ . Both the primary and secondary signals are then combined before input to the vertical motion cueing filter  $W_{22}$ .

From a simulated Boeing 757-200 aircraft test run, a system identification of aircraft vertical accelerations in response to turbulence was performed. The transfer function  $H_G(s)$  was then created to not only represent the acceleration, but also incorporate some desired motion cueing characteristics, i.e., attenuated low-frequency content and increased high-frequency content. The following second-order transfer function was obtained for  $H_G(s)$ :

$$H_G(s) = 0.1 \frac{(2.4s + 1)(2.4s + 1)}{(0.4s + 1)(0.1s + 1)}. \quad (2.8)$$

For the optimal algorithm, a gain of  $K_G$  equal to 0.8 was chosen to maximize the desired sensation of turbulence while sustaining the actuator extensions within the motion limits. A similar implementation to that shown in Figure 2.7 was applied for the nonlinear algorithm. In this approach, the linear cueing filter  $W_{22}$  was replaced with the nonlinear heave filter, with the gain  $K_G$  set equal to 1.2.

## 2.7. Pilot Tuning of the Cueing Algorithms

A computer program [10] was developed for the purpose of driving the NASA Langley Visual Motion Simulator (VMS) described in Section 2.1. This program includes both the optimal algorithm and the nonlinear algorithm. A general description of the program is given along with a description and flow charts of each cueing algorithm. Common block variable listings and a program listing are also provided. Procedures for tuning the nonlinear gain coefficients are also given.

In order to determine the nonlinear scaling (gain) coefficients for each degree-of-freedom that resulted in the most desired pilot performance, a trained simulator pilot executed a series of pilot controlled maneuvers with the optimal algorithm on the VMS. A series of maneuvers were first executed with the coefficients determined prior to

testing. Coefficients for each degree-of-freedom were then adjusted until the simulator pilot subjectively felt the desired perception and performance were reached, while ensuring that the simulator motion platform limits were not exceeded. The following maneuvers were executed for both algorithms:

- Straight Approach and Landing (with varying wind from head to tail)
- Offset Approach and Landing (with and without turbulence)
- Pitch, Roll, and Yaw Doublets
- Throttle Increase and Decrease
- Coordinated Turn
- Ground Maneuvers (taxiing, effect of aircraft brakes)
- Takeoff from Full Stop.

The optimal algorithm resulted in motion cues with which the simulator pilot commented he had more control and confidence in comparison to the NASA adaptive algorithm. For both pitch and roll doublets, a fast response was observed when changing directions. On takeoffs, the optimal algorithm was found to be easier to pitch up to the desired attitude and control the aircraft. A noticeably large side force was observed with the coordinated turn maneuver. By reducing the gains for the roll degree-of-freedom, this side force was reduced to a minimal sensation. The pitch gains were decreased to reduce the likelihood of entering the braking region or exceeding the actuator limits. Reducing the gains for both roll and pitch degrees-of-freedom still yielded acceptable motion cues.

The severe turbulence effects that were included with the offset approach and landing maneuver were hardly noticeable. An increase of the vertical gain coefficients resulted in increased cues, but still less than satisfactory. This increase in the vertical gains (coupled with an increase of the surge gains) resulted in forward surge cues that are more coordinated with the pitch cues, and a larger aft surge cue (initially, the aft cue was

noticeably smaller than the forward cue). The unsatisfactory turbulence cues resulted in the inclusion of the augmented motion cue driven by the vertical gust.

A second pilot tuning evaluation was later performed on the VMS with both the optimal and nonlinear algorithms, with augmented turbulence cues implemented for both algorithms. A series of maneuvers were first executed with the polynomial gain coefficients determined prior to testing. Coefficients for each degree-of-freedom were then adjusted until the simulator pilot subjectively felt the desired perception and performance were reached, while ensuring that the simulator motion platform limits were not exceeded. The following maneuvers were executed for both algorithms:

- Straight Approach and Landing (with varying wind from head to tail)
- Offset Approach and Landing (with and without turbulence)
- Takeoff from Full Stop (with and without engine failure)
- Ground Maneuvers (taxiing, effect of aircraft brakes).

No additional tuning was needed for either the straight-in or offset approach maneuvers. However, both algorithms showed a tendency to exceed the actuator limits of the motion system with the takeoff maneuver. Reducing the surge gains for the optimal algorithm and both the surge and pitch gains for the nonlinear algorithm resulted in platform motion within the actuator limits during the takeoff maneuvers. The augmented turbulence gain terms for the optimal and nonlinear algorithms discussed in Section 2.6 were adjusted to produce the desired turbulence cues.

Table 2.1 lists the resulting nonlinear gains by degree-of-freedom implemented for each algorithm. From Eq. (2.7), the coefficients  $c_1$ ,  $c_2$ , and  $c_3$  are given for each degree-of-freedom.

**Table 2.1. Nonlinear Gain Coefficients for the Cueing Algorithms.**

Degree-of-Freedom	Optimal Algorithm			Nonlinear Algorithm		
	C1	C2	C3	C1	C2	C3
Surge (X)	0.6	-0.055	0.002	0.5	-0.05	0.002
Sway (Y)	0.5	-0.055	0.002	0.4	-0.035	0.001
In-Air (Z)	0.6	-0.082	0.0038	0.6	-0.082	0.0038
On-Ground (Z)	1.3	-0.0375	0.0003	2.0	-0.05	0.0
Roll (p)	0.3	-0.3	0.1	0.3	-0.3	0.1
Pitch (q)	0.4	-0.54	0.26	0.3	-0.3	0.1
Yaw (r)	1.1	-1.46	0.64	1.1	-1.46	0.64

This page intentionally left blank.

### **3. Test Procedure**

The study consisted of four flight scenarios: (1) a straight-in approach, (2) an offset approach, (3) a normal takeoff, and (4) a takeoff with engine failure. The details of the flight scenarios are described below.

#### **(1) Straight-in Approach**

Altitude - 1300 ft BARO, 697 ft AGL

Airspeed - 135 kts

Heading - 180 deg

Distance to runway - 2 nm

Flaps - Full, Gear - Down

EPR - 1.19

On Glideslope, On Localizer

Wind Conditions - 10 kts, Begins as a head wind, swings around to a 90 deg wind from the left at 1 nm, and continues to swing around to a tail wind as the aircraft crosses the threshold.

#### **Procedure –**

Visual approach,

PAPI lights available on Runway 18R,

Glideslope and Localizer needles available on Primary Flight Display

#### **(2) Offset Approach**

Altitude - 1300 ft BARO, 697 ft AGL

Airspeed - 135 kts

Heading - 180 deg, aligned with Runway 18L

Distance to runway - 2 nm

Flaps - Full, Gear - Down

EPR - 1.19

On Glideslope

Wind Conditions - Severe Turbulence. Lateral gust from the left, 90 deg to runway centerline, turns on at 3000 ft from runway threshold, turns off at the runway threshold.

**Procedure –**

When the red light on instrument panel illuminates (7500 ft from threshold), realign approach and land on Runway 18R,

Visual approach, PAPI lights available on Runway 18R,

Glideslope and Localizer needles available on Primary Flight Display.

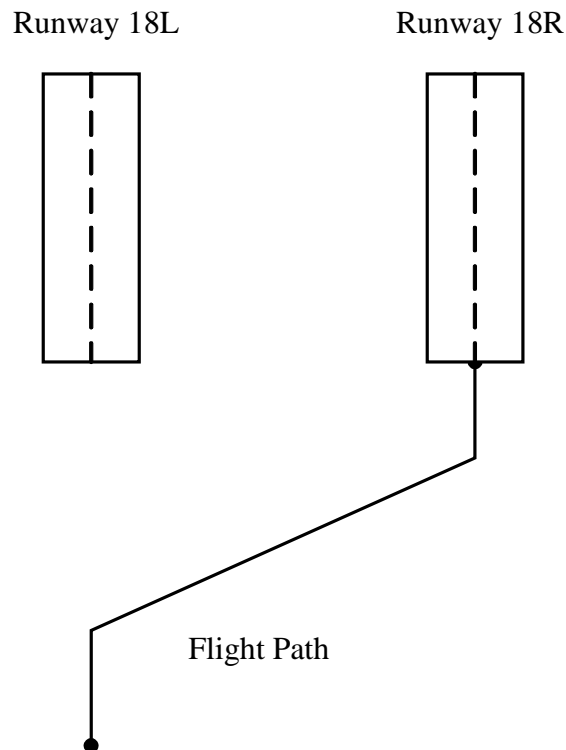


**Figure 3.1. Schematic Diagram of Offset Approach Maneuver Flight Path.**

### **(3) Takeoff - With or without engine failure**

Runway 18R

Flaps - 5 deg

Takeoff EPR - 1.70

$V_R$  - 135 kts,  $V_1$  - 130 kts,  $V_2$  - 140 kts

#### **Procedure -**

Advance throttles from idle to Takeoff EPR

At  $V_R$ , rotate to 15 deg pitch-up attitude

Climb to 2000 ft BARO while accelerating to 200 kts

Retract gear and flaps as appropriate

Maintain runway heading of 180 deg during takeoff

A set of 96 test runs was executed by each pilot and consisted of three maneuvers: 24 for the straight-in approach, 24 for the offset approach, 24 for the normal takeoff, and 24 for the takeoff with engine failure.

The 24 runs for each of the two approach maneuvers resulted from the enumeration of three simulation conditions: four computer image generator (visual display) time delays, both with and without delay compensation: (0, 50, 100, and 200 msec), and three motion cueing algorithms (NASA adaptive, optimal, and nonlinear). This accounted for  $4 \times 2 \times 3 = 24$  test runs per maneuver. For the takeoff maneuver, there were twice as many cases (48) because of an additional test condition, i.e., the case with engine failure. Each maneuver included two test runs with zero delay; for zero delay, the “compensated” run was effectively the same as the uncompensated run. The order of the test runs for each maneuver was randomized, i.e. a zero delay case is not

necessarily the first run, and one cueing algorithm does not necessarily follow another. In addition, the 24 engine failure cases occurred equally distributed at altitudes of 200, 400, 600, and 800 feet above ground level, with either the right or left engine failing. These cases occurred randomly and not necessarily following each other or a case without engine failure.

Appendix A lists the matrix of test runs for each maneuver. With the exception of the first pilot, each pilot first executed the straight-in approach (runs 1 to 24), next the first set of takeoff runs (runs 49 to 72), then the offset approach (runs 25 to 48), followed by the second set of takeoffs (runs 73 to 96). The first pilot executed all runs in order from 1 to 96, commenting that executing 48 takeoffs in a row became difficult to separate one run from another. For each test run, 66 variables were sampled and recorded. The simulation time step was 16 msec. Every fourth sample was recorded, which resulted in a sampling period of 64 msec. For a single test run, about 1000 data points were collected for each variable. These sampled variables are listed in Appendix A. Following execution of each maneuver, each pilot rated the maneuver using the NASA TLX method discussed in the next section.

Eleven pilots took part in the test, with each pilot executing the 96 test runs over one or two days. The pilots had varying aircraft and flight experience.

## **4. Methods of Analysis**

### **4.1. NASA Task Load Index (TLX)**

The NASA Task Load Index (TLX) [4] is a quasi-objective rating procedure that provides an overall workload metric based on a weighted average of six subscale ratings. Three of these subscales relate to the demands imposed on the test subject (mental, physical, temporal) and three to the interaction of the subject with the task (effort, frustration, performance). In addition to the six subscales, an overall weighted measure of the task load is calculated on the basis of the scales. The TLX can be used for any human-system interaction, and has been tested in experimental tasks such as flight simulation and supervisory control.

The NASA TLX is a two-part evaluation procedure consisting of both ratings and weightings. The first part of the procedure involves obtaining a numerical rating for each subscale that reflects the magnitude of the workload for a given task. The rating definitions for each subscale are given in Appendix A. For each test run, the pilot rates each subscale by placing a mark on the desired location on a scaled recording sheet.

The second part of the procedure requires the test subject to evaluate the contribution of each workload subscale to the total workload of a specific task. The weighting reflects the importance of each workload subscale relative to the other subscales, accounting for both the subjects' definition of workload within a task, and differences in the workload sources between tasks. The degree to which each factor contributes to the workload of a specific task is determined by the subject's response to a pair-wise comparison among the six factors. For six subscales, there are 15 pair-wise comparisons. Subjects select a subscale from each pair that contributed more to the

workload of that task. The weighted contribution of each subscale can range from 0 to 5. These weighted workload subscales are then combined to produce a weighted TLX rating for each test run. A high TLX rating implies the pilot is exerting a high workload.

#### **4.2. Pilot Control Input Analysis**

Guo, et al. [3] further demonstrated the application of analyzing power spectral density (PSD) of the pilot control inputs for two motion cueing algorithms (adaptive and optimal) at various time delays, both with and without compensation. Guo, et al. computed the PSD using the smoothed periodogram to eliminate noise artifacts and enhance the microscopic characteristics of the frequency process. The Hamming window [Porat, 1997 #108] using 4096 points was chosen, and zero padding was applied to the time signal to enhance the resolution of adjacent peaks. The average of the signal was subtracted from itself before the PSD was computed to remove any artificial peaks at zero Hz.

An individual PSD for each control input (pitch stick, roll stick, rudder pedal) was first computed for each pilot for a given test condition. Guo, et al. [3] reported that the effect of the test condition, i.e. the cueing algorithm or the delay, had little effect on the throttle, and thus, is not discussed further in this report. These individual PSDs were then averaged at each computed frequency for a given pilot group to produce an average PSD for each cueing algorithm. In the preliminary test, Guo, et al. reported that almost all of the integral power occurs in the frequency range from 0 to 1 Hz. This frequency range is consistent with the human-machine control bandwidth. In computing the integral power, Euler integration is used to calculate the area of the PSD from 0 to 1 Hz. The average

integral power and its standard deviation are then computed for a group of pilots so that the effect of both the motion cueing algorithm and the delay can be assessed.

### 4.3. Simulator Coherence Analysis

Levison, et al. [11] reported that both Levison and Elkind and McRuer, et al. defined the remnant as the portion of the controller output that is not related to the system input by an input/output describing function. They noted that McRuer, et al. concluded that the PSD of the controller remnant is a smooth function of frequency, the remnant is strongly dependent upon the order of the controller dynamics, and can be represented by an equivalent “observation noise” disturbance at the controller input. Levison, et al. [11] developed a model for human controller remnant based upon the assumption that the remnant can be represented as a single vector observation noise process.

A single-degree-of-freedom representation of this model is given in Figure 4.1. The information presented to the human controller is contained in the display vector  $\mathbf{x}$ . This display vector is perturbed by an additional observation noise process  $\mathbf{R}_x$ , yielding  $\mathbf{x}'$  as the total input to the controller. The controller input  $\mathbf{x}'$  is then processed by the controller’s describing function  $H$  to yield the control signal  $\mathbf{u}$  that is applied to the vehicle dynamics  $V$ . In order to simplify analysis of the human-vehicle system, Levison, et al. assumed that the controller’s perceptual and response activities are limited to the estimation of the system error and error rate, along with the explicit control of the output variable and its rate of change. These assumptions imply that the task is compensatory, with a single display presented to the controller from which both the error and rate of error can be obtained.

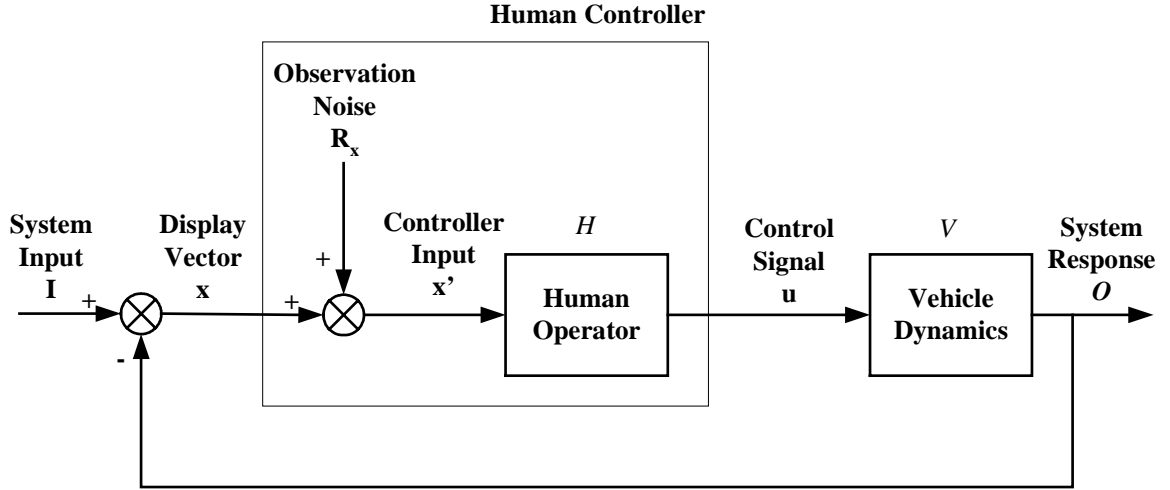


**Figure 4.1. Single-Degree-of-Freedom Manual Control System with Remnant.**

Levison, et al. [11] developed an expression for the observation noise spectrum that is a function of the input noise spectrum, and noted that since the input spectrum can only be obtained at the input frequencies, the observation noise spectrum can only be specified at those same frequencies. Their use of the sum of sinusoidal inputs also facilitated the separation and estimation of remnant-induced signals, since the signal power at frequencies other than the inputs were assumed to arise solely from the remnant.

In a human-vehicle system such as an aircraft, both the system inputs, e.g. the aircraft states, and the pilot control output responses are normally wide-band processes with peak power magnitudes at varying frequencies. One means of quantifying the effects of the observation noise is by computing the coherency spectrum  $\kappa_{yu}$  between the system input and its response [12]:

$$\kappa_{yu} = \sqrt{\frac{|\Phi_{yu}(\omega)|^2}{\Phi_y(\omega)\Phi_u(\omega)}}, \quad (4.1)$$

where  $\Phi_y(\omega)$  and  $\Phi_u(\omega)$  are the power spectral densities for the system output and input respectively, and  $\Phi_{yu}(\omega)$  is the cross-spectral density between the input and output. Ljung [12] noted that the coherency function  $\kappa_{yu}$  can be viewed as a frequency-dependent correlation coefficient between the input and output frequencies, with  $0 \leq \kappa_{yu} \leq 1$ . A coefficient of 1 at a given frequency means that there is perfect correlation between the input and output, with no observation noise. Decreasing values of coherence indicate an increasing effect of the observation noise.

From the experimental data, coherence will be computed using either the simulator motion platform or the simulated aircraft attitude (pitch or roll) as input, and the corresponding control stick response (pitch or roll) as output. Average PSD of the aircraft and simulator attitudes will also be computed in order to reveal any differences among the three motion cueing algorithms.

This page intentionally left blank.

## 5. Analysis Results

During each pilot test, an experienced simulator pilot rode in the simulator in the first officer's seat and observed the control technique and instrument scan patterns of the pilot. In addition, any atypical or unusual behavior when executing maneuvers was noted. From these observations, the pilots can be aggregated into groups in Table 5.1 based upon their control technique and instrument scanning behavior. The most disciplined scan pattern was observed for Pilot Group 1, and was less disciplined for Pilot Group 2. Pilot Group 3 showed the most erratic scanning and control behavior, with individual problems noted for each pilot. By original observation, Group 3 was aggregated into two subgroups (Pilots 2 and 9 and Pilots 3 and 5) that showed the most erratic scanning and control behavior; however Pilot 9 showed less erratic behavior from both the pilot comments and data analysis and was placed in Group 2. Pilot 11, for reasons discussed below, was re-categorized from Group 2 to Group 3.

**Table 5.1. Pilot Groups by Control Technique and Instrument Scan Pattern.**

Pilot Group 1	Pilot 1, Pilot 4, Pilot 7, Pilot 10
Pilot Group 2	Pilot 6, Pilot 8, Pilot 9
Pilot Group 3	Pilot 2, Pilot 3, Pilot 5, Pilot 11

Pilot 2 encountered difficulty on the approach maneuvers as a result of flying predominantly with the instruments and then suddenly transitioning to the visual scene 200 feet above the runway. Pilot 3, a pilot more experienced with small aircraft, had no experience with large transport aircraft, which was manifested predominantly with the takeoff maneuvers. Pilot 5, an experienced military aircraft pilot, exceeded the motion system actuator limits on several optimal algorithm test runs due to aggressive liftoff rotations that resulted in a very high rate of climb and large heave displacement. By

comparison, the liftoff technique of Pilot 4 showed about one-half the rate of climb, with much smaller heave displacements. Pilot 11 showed very erratic control behavior during the final phase of the approach. This resulted in a number of approach runs ending with pilot-induced oscillation (PIO) at the landing flare.

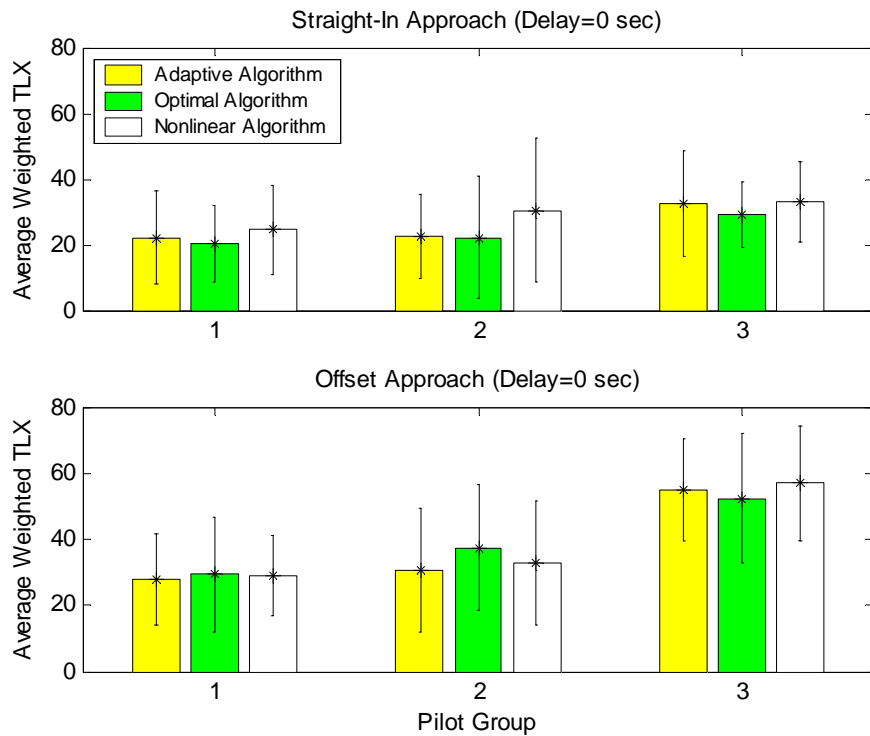
The aggregated pilot groups were used in the NASA TLX analysis discussed in the next section. Appendix B provides a control input analysis for Pilot Groups 1 and 2 for each of the four test maneuvers. For each pilot group, this control analysis consists of the average PSD (of all pilots in the group) as a function of frequency for uncompensated delay conditions of 0, 100, and 200 msec. The 50 msec delay condition was not analyzed since its effect on pilot performance and workload was expected to be insignificant. The pitch stick and roll stick were analyzed for all maneuvers, with the rudder pedal also analyzed for the takeoff maneuver with engine failure. With the exception of the takeoff with engine failure, the rudder PSD is much less than either the pitch stick or roll stick PSD.

### **5.1. NASA Task Load Index**

Due to differences in hardware, the visual system image generator transport delay varies among different simulators. Some researchers have opined that the effects of the image generator delay may be mitigated by the addition of motion cues. For this reason, it becomes important to understand the motion cueing algorithm performance as a function of the uncompensated delay, and its subsequent effect on the pilot's workload. In order to investigate the variations among the algorithms by pilot group, the NASA Task Load Index (TLX) analysis was first performed for the zero delay case. The

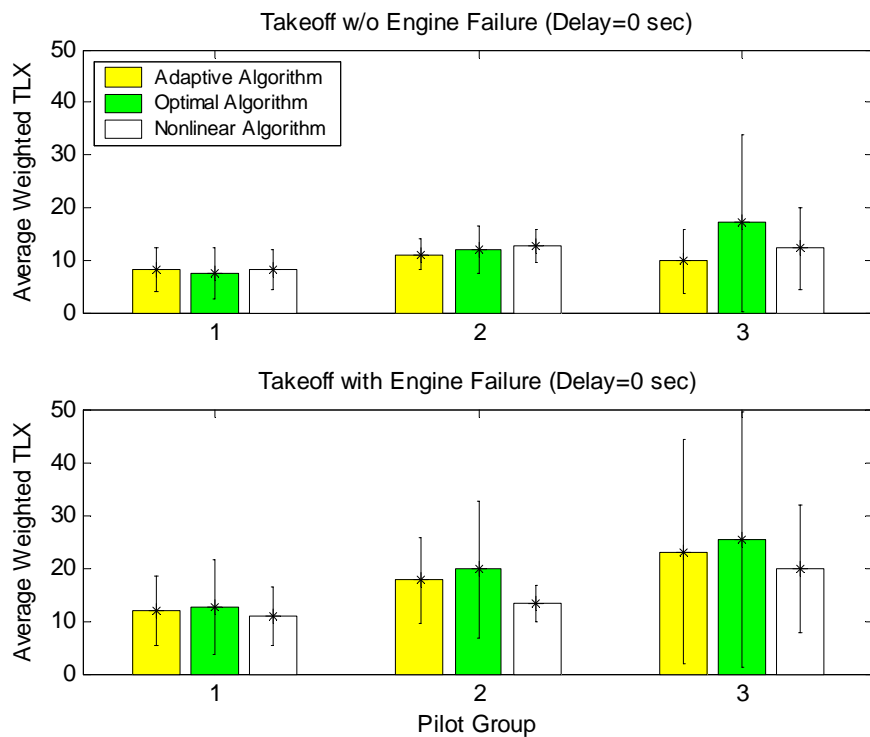
analysis was then performed among the cueing algorithms at delays of 0, 100, and 200 msec.

Figure 5.1 compares the average weighted TLX ratings for the straight-in and offset approach maneuvers with no delay for each aggregated pilot group. For the straight-in approach, the results for each algorithm were not significantly different, although the nonlinear algorithm tends to show a slightly higher workload. Pilot Groups 1 and 2 were about the same, while Group 3 showed a small increase for all algorithms. The standard deviation did not vary much among either the algorithms or the pilot groups. For Pilot Groups 1 and 2, the offset approach did not show significant differences among the cueing algorithms, with Group 2 showing a slightly higher TLX for all algorithms. Group 3 showed a much more noticeable increase for all algorithms, with no noticeable difference among the algorithms.



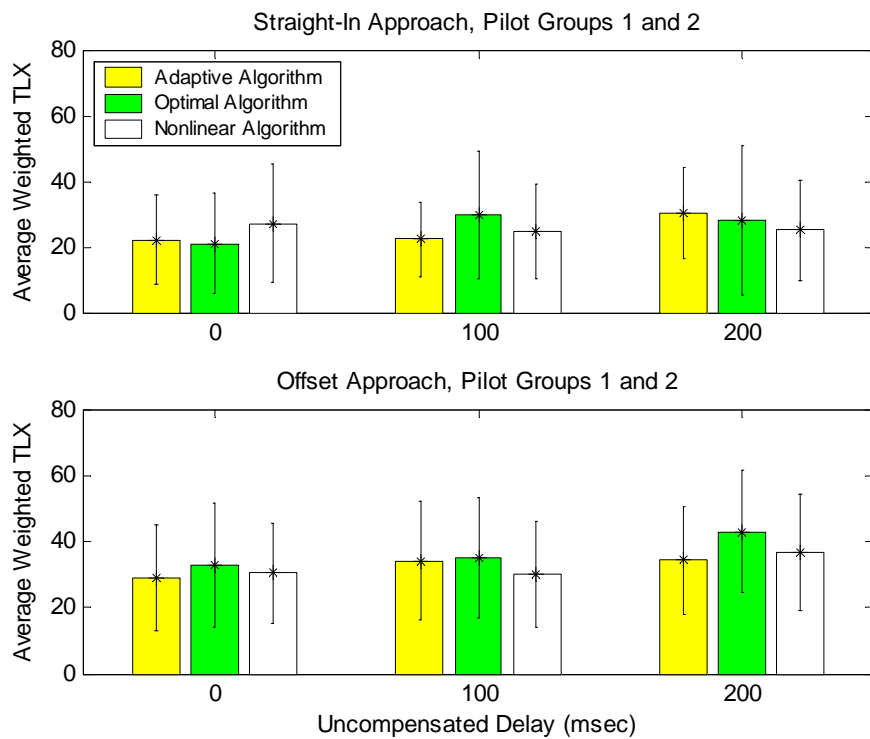
**Figure 5.1. TLX for Approach Maneuvers by Pilot Group with No Delay.**

Figure 5.2 shows the average weighted TLX for the takeoff maneuver (with and without engine failure) with no delay. For the case without engine failure, Groups 1 and 2 do not reveal any significant differences in workload among the algorithms, with Group 2 showing a slightly higher TLX for each algorithm. Pilot Group 3 shows larger standard deviations for all algorithms, with a much higher average rating and variation occurring with the optimal algorithm. The standard deviation of the nonlinear algorithm was about the same as the adaptive algorithm for each pilot group. The case with engine failure shows an increase in both the average rating and standard deviation by pilot group, Group 1 having the lowest ratings and variation and Group 3 showing much higher ratings and variation. Note that the nonlinear algorithm shows the lowest ratings and variation for each pilot group.



**Figure 5.2. TLX for Takeoff Maneuvers by Pilot Group with No Delay.**

Figure 5.3 shows the average weighted TLX ratings for the straight-in and offset approach maneuvers as a function of delay. The average TLX for each cueing algorithm is computed for Pilot Groups 1 and 2 combined. Pilot Group 3 is removed from this analysis due to its increased workload and variability observed among the cueing algorithms. For the straight-in approach, the results for each algorithm are not significantly different. With zero delay, the nonlinear algorithm produced the highest TLX, but showed a lower rating for the 100 msec case compared to the optimal algorithm, and the lowest rating for 200 msec delay among all algorithms. For this maneuver, the cueing algorithms do not reveal a consistent trend with increasing delay.



**Figure 5.3. TLX for Approach Maneuvers with Delay, Pilot Groups 1 and 2.**

The offset approach also did not reveal any significant differences among the cueing algorithms. A small increase in the TLX was observed as a function of delay; the

nonlinear algorithm resulted in the lowest workload for both 100 and 200 ms delay cases, while the optimal algorithm showed the highest workload for all delay cases.

Figure 5.4 shows the average weighted TLX for the takeoff maneuver (with and without engine failure) for Pilot Groups 1 and 2 as a function of delay. For the case without engine failure, the TLX was almost the same for each algorithm with the absence of delay. With delay, the optimal algorithm produced a higher TLX, while the adaptive and nonlinear algorithms showed no significant change with delay. The standard deviation was about the same for all algorithms. The case with engine failure resulted in the nonlinear algorithm having a slightly lower rating with zero delay. Increasing the delay resulted in higher ratings (with the same standard deviation) for all algorithms, with the nonlinear algorithm having a lower TLX among all algorithms at 100 msec, and a lower rating at 200 msec compared to the optimal algorithm.

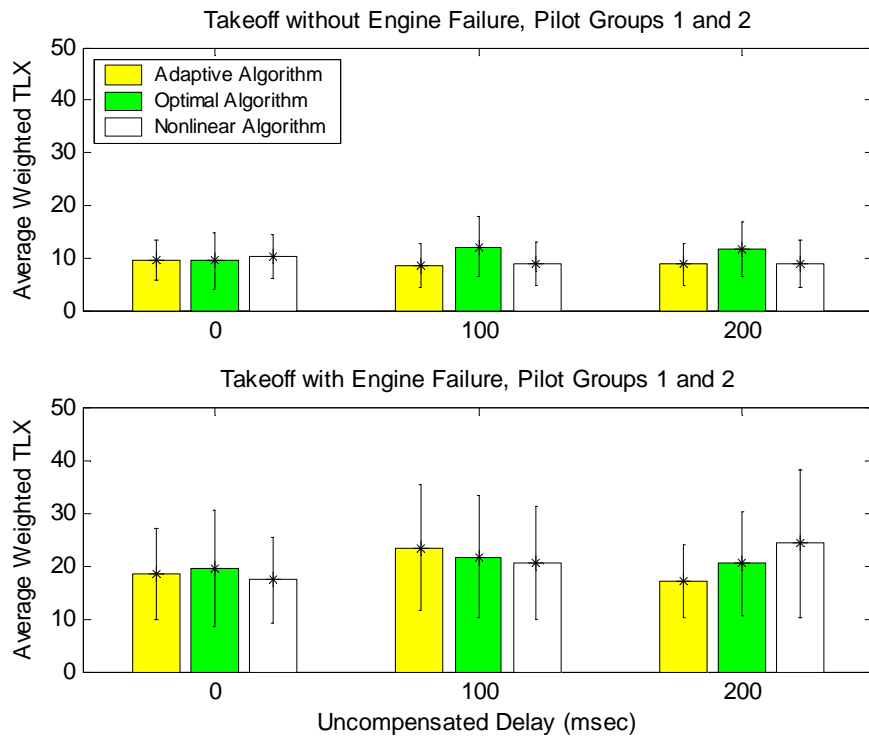
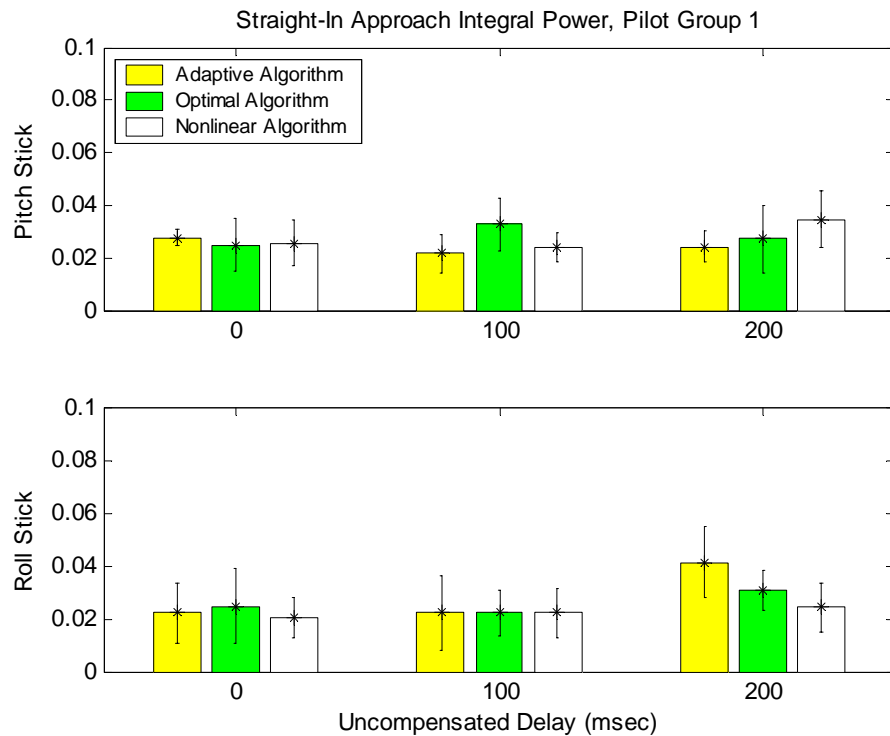


**Figure 5.4. TLX for Takeoff Maneuvers with Delay, Pilot Groups 1 and 2.**

## 5.2. PSD Analysis

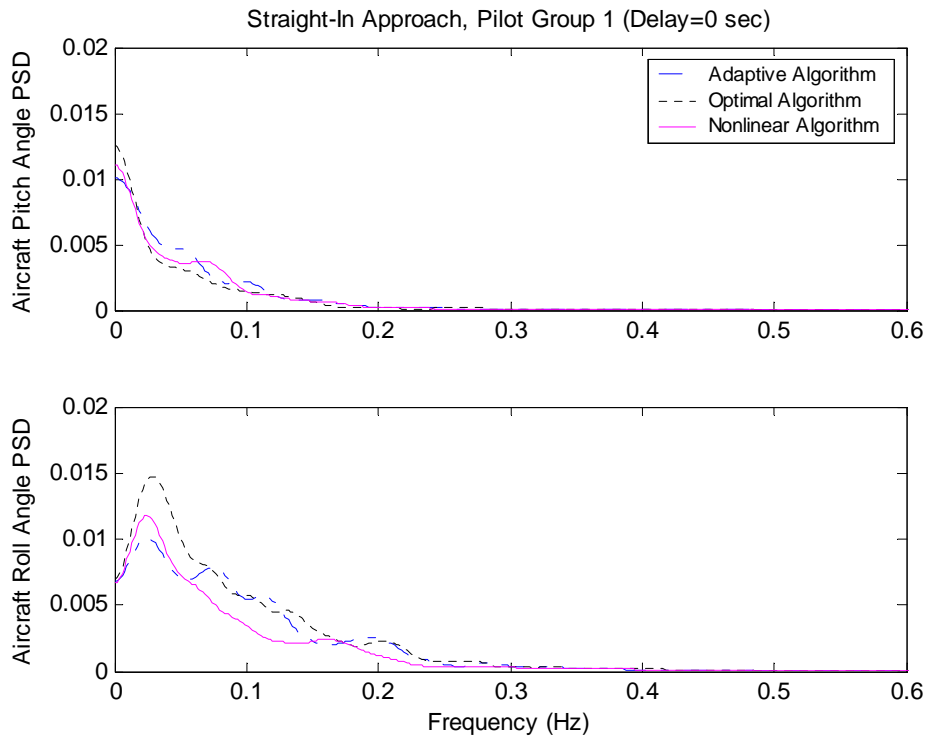
### 5.2.1. Straight-In Approach

Figure 5.5 shows the control input integral power for Pilot Group 1. The conditions with both zero and 100 msec delay showed insignificant differences among the cueing algorithms for both the pitch stick and roll stick. For 200 ms delay, the adaptive algorithm had the largest power increase for the roll stick. The nonlinear algorithm remains almost unchanged as a function of delay, with the least amount of roll stick power variation among the three algorithms. The average PSD for the zero delay condition is shown in Appendix B, Figure B.1. Note that there was only a small variation among the cueing algorithms for either the pitch stick or roll stick PSD. Increased control activity with delay is observed in the average PSD for 100 and 200 msec delay conditions shown in Figures B.2 and B.3 of Appendix B.



**Figure 5.5. Straight-In Approach, Control Input Integral Power, Pilot Group 1.**

Figure 5.6 shows the average PSD for the aircraft roll and pitch angles for Pilot Group 1 with zero delay. The pitch angle PSD is similar to the pitch stick PSD of Figure B.1, with the aircraft PSD about the same for all three cueing algorithms. The roll angle PSD revealed a low-frequency peak between 0.02 and 0.03 Hz for all algorithms, with the optimal algorithm having the largest peak magnitude.



**Figure 5.6. Straight-In Approach, Aircraft Angle Average PSD with Zero Delay, Pilot Group 1.**

Figure 5.7 shows the control input integral power for Pilot Group 2. Both the pitch stick and roll stick produced increased power and standard deviation for each cueing algorithm over Group 1. The zero delay condition showed an increase in power from the adaptive to the nonlinear algorithm. In Figure B.4, the average PSD for zero delay showed a large peak near 0.45 to 0.5 Hz for the nonlinear algorithm, which is due to reported incidents of pilot-induced oscillation (PIO) for Pilots 6 and 8. The optimal

algorithm resulted in significantly large integral power and variation at both 100 and 200 msec delay, which is due to repeated incidents of PIO for Pilot 6. These PIO incidents were evident in the average PSD in Figures B.5 and B.6. For the nonlinear algorithm, while the pitch stick power remained unchanged with delay, the roll stick power decreased, with no incidents of PIO observed.

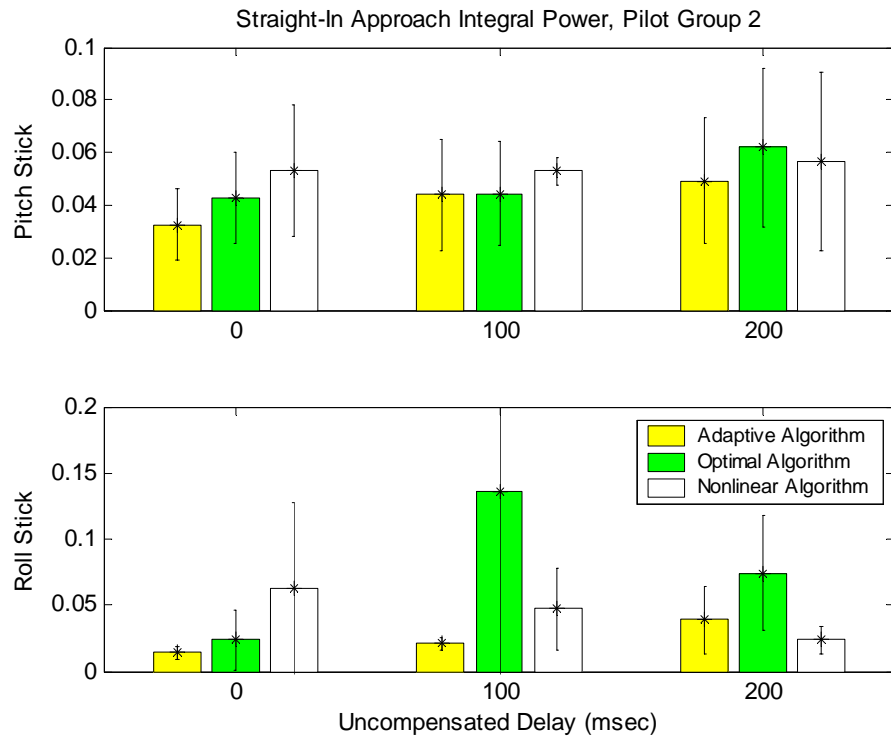


**Figure 5.7. Straight-In Approach, Control Input Integral Power, Pilot Group 2.**

Figure 5.8 shows the average PSD for the aircraft roll and pitch angles for Pilot Group 2 with zero delay. The increased PSD for both the pitch and roll angle reflects the increased control input power shown in Figure 5.7. The pitch angle magnitude is highest for the nonlinear algorithm. The optimal algorithm showed the largest low-frequency peak for the roll angle, with the variation among the algorithms being more significant in

comparison to Pilot Group 1. The roll stick PIO illustrated in Figure B.6 is observed in the roll angle PSD at about the same frequency.

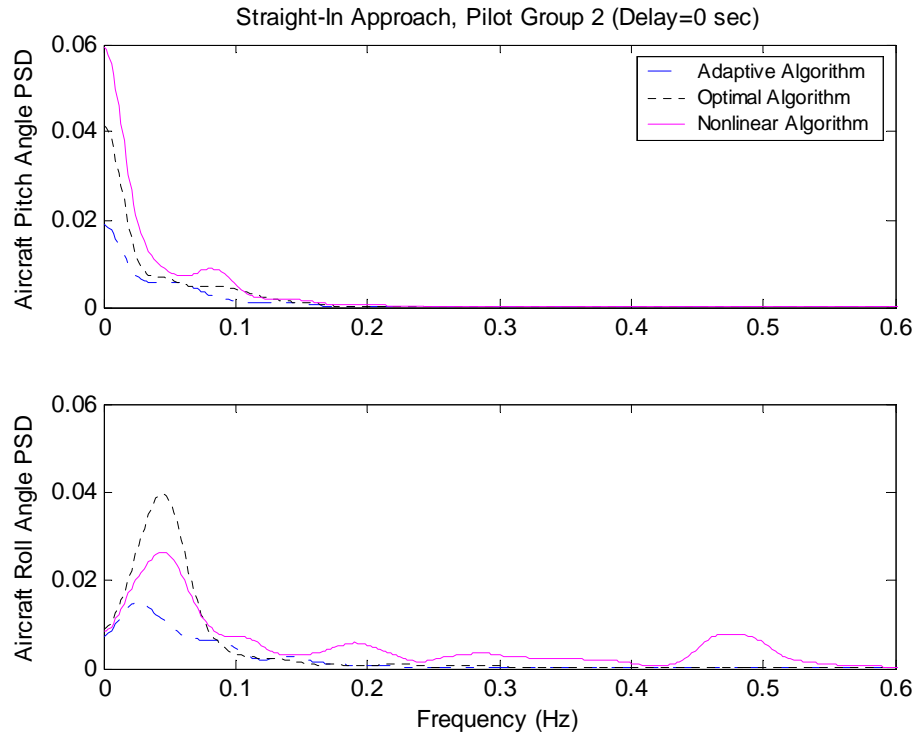


**Figure 5.8. Straight-In Approach, Aircraft Angle Average PSD with Zero Delay, Pilot Group 2.**

The vertical rate of the aircraft upon touchdown can be considered as a measure of performance. A small touchdown rate would indicate that the pilot has more control of the aircraft, while a higher rate results from the pilot having less control. Figure 5.9 shows the average vertical rate at the touchdown for both Pilot Group 1 and Pilot Group 2. Note that the vertical rates for Pilot Group 1 are low (less than 2 ft/sec), with the adaptive algorithm producing the lowest rates. For Pilot Group 2, the vertical rates increased for all cueing algorithms, with no significant difference among the algorithms for either pilot group.

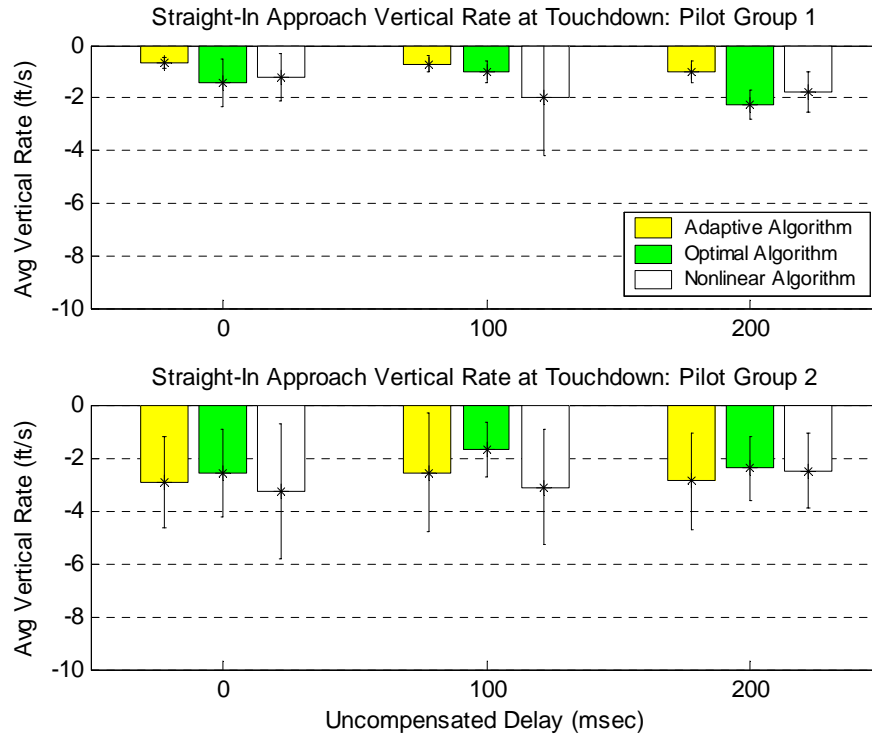


**Figure 5.9. Straight-In Approach, Vertical Rate at Touchdown.**

The x- and y- coordinates of the aircraft at touchdown; i.e. the distance from the runway threshold (the start of the runway), and the distance from the runway centerline were investigated. These results are shown in Figure 5.10 and Figure 5.11. No noticeable or significant trends were observed with either coordinate among the motion cueing algorithms, although the pilots in Group 1 tended to land an average of about 300 feet further down the runway. The longer landing may also account for a lower vertical rate at touchdown, indicating that the aircraft was “floating” as the pilot attempted to land.

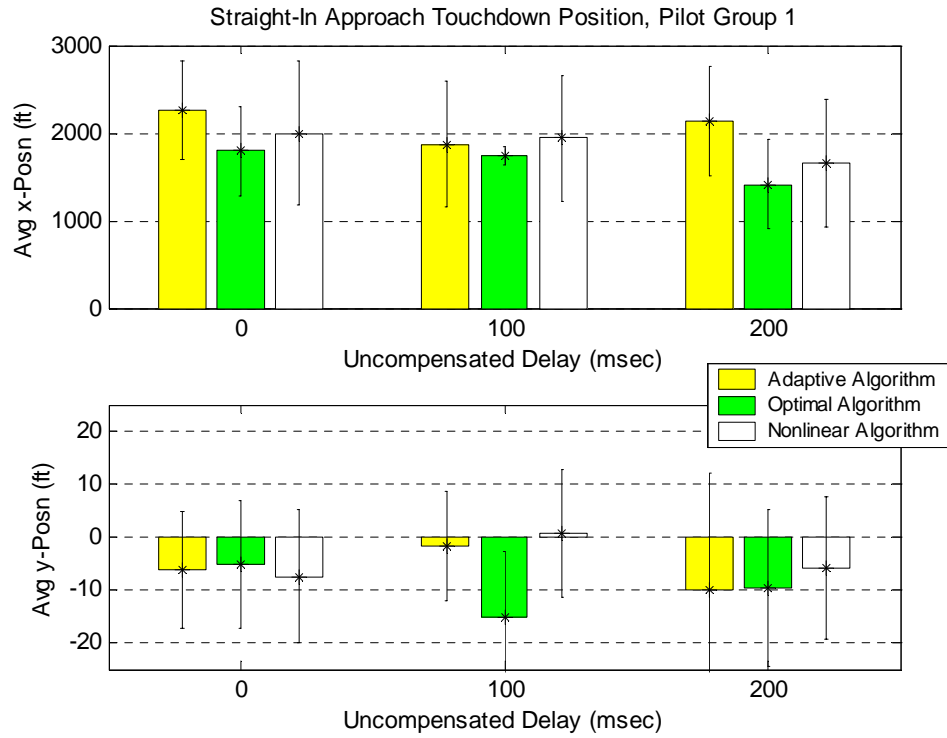


**Figure 5.10. Touchdown Coordinates, Straight-In Approach, Pilot Group 1.**

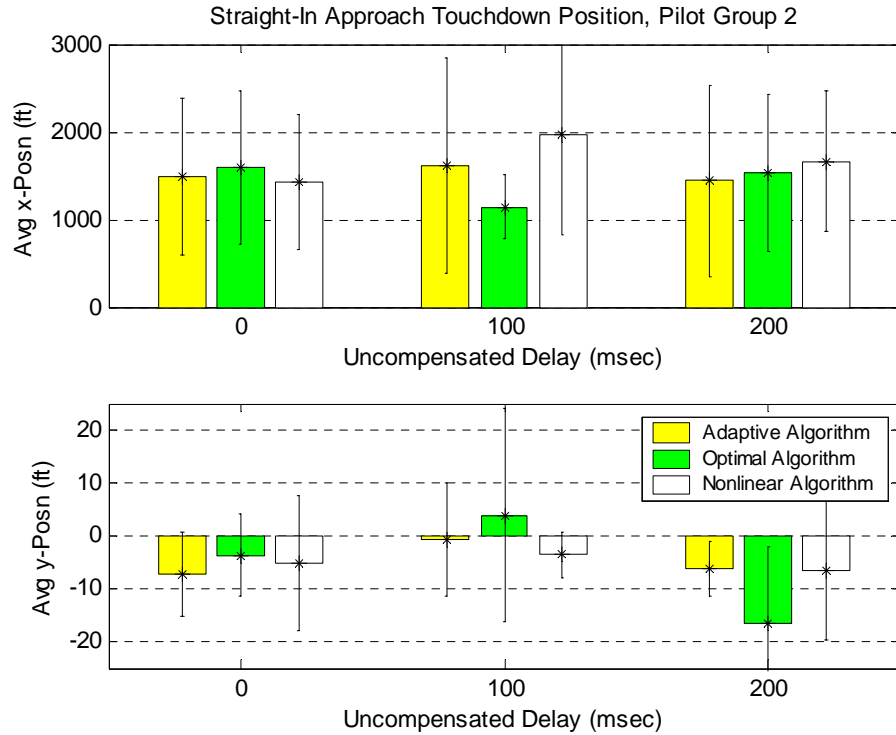


**Figure 5.11. Touchdown Coordinates, Straight-In Approach, Pilot Group 2.**

### 5.2.2. Offset Approach

Figure 5.12 shows the control input integral power for Pilot Group 1. The zero delay condition shows increasing pitch stick power from the adaptive to the nonlinear algorithm. The nonlinear algorithm produced slightly more roll stick power than either optimal or adaptive. With delay, the roll stick power increased for both the optimal and nonlinear algorithms, but only at 200 msec delay for the pitch stick power.

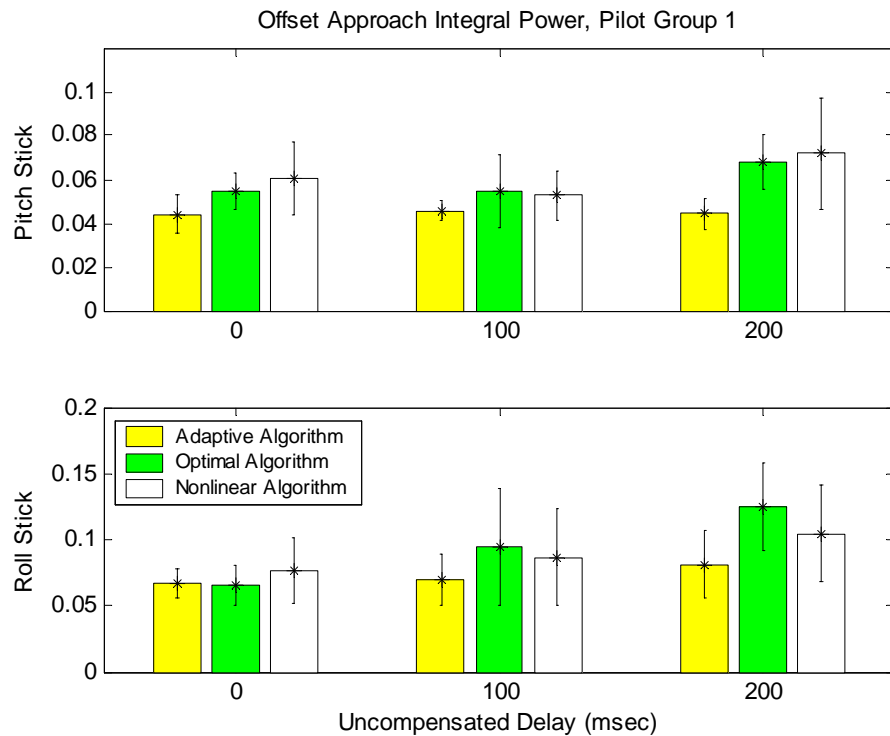
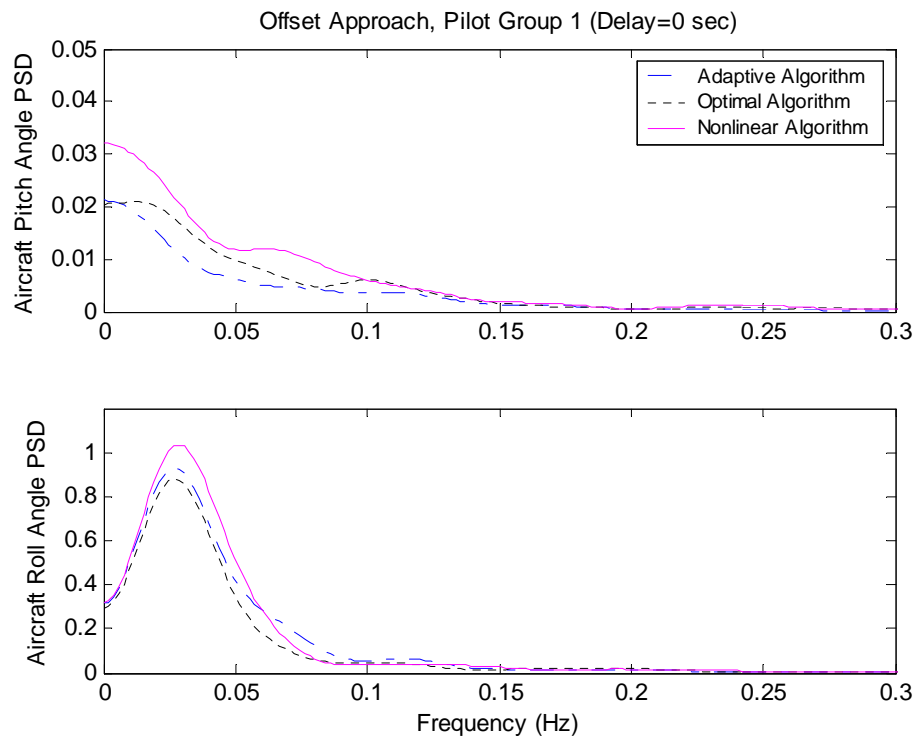


**Figure 5.12. Offset Approach, Control Input Integral Power, Pilot Group 1.**

Figure B.7 of Appendix B shows the average PSD for the zero delay condition for Pilot Group 1. Note that the nonlinear algorithm produced a higher low-frequency PSD for the pitch stick and higher mid-frequency (0.2 to 0.5 Hz) PSD for the roll stick. Increased control activity with delay is observed in the average PSD for 100 and 200 msec delay conditions shown in Figures B.8 and B.9 of Appendix B. An increase in PSD

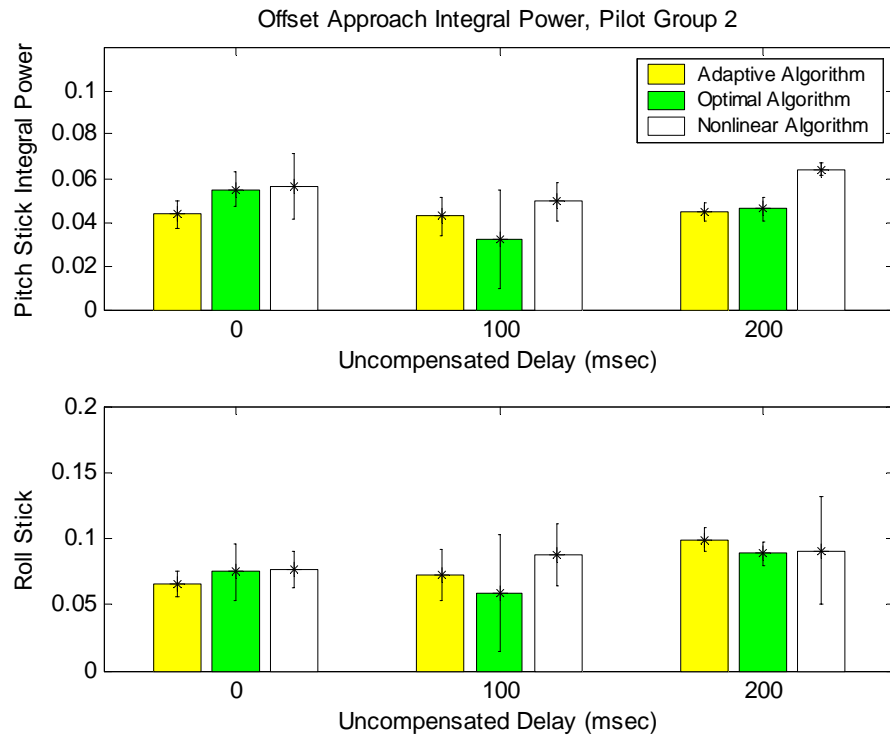
is observed in the frequency range from 0.1 to 0.4 Hz. For the 100 ms condition, Pilot 1 reported that the delay was noticeable and the controls were less responsive for both the optimal and nonlinear algorithms.

Figure 5.13 shows the average PSD for the aircraft roll and pitch angles for Pilot Group 1 with zero delay. The pitch angle PSD is similar to the pitch stick PSD of Figure B.7, with the nonlinear algorithm showing the largest pitch angle activity. The roll angle produced a large peak at about 0.028 Hz for all algorithms, which was also reported by Guo, et al. [3] in the preliminary test. This frequency corresponds to a period of about 34 seconds, the duration of the offset approach. The nonlinear algorithm produced a slightly larger peak magnitude that corresponds to the larger control input integral power in Figure 5.12 as well as the higher low-frequency peak in the average PSD in Figure B.7.



**Figure 5.13. Offset Approach, Aircraft Angle Average PSD, Pilot Group 1 with Zero Delay.**

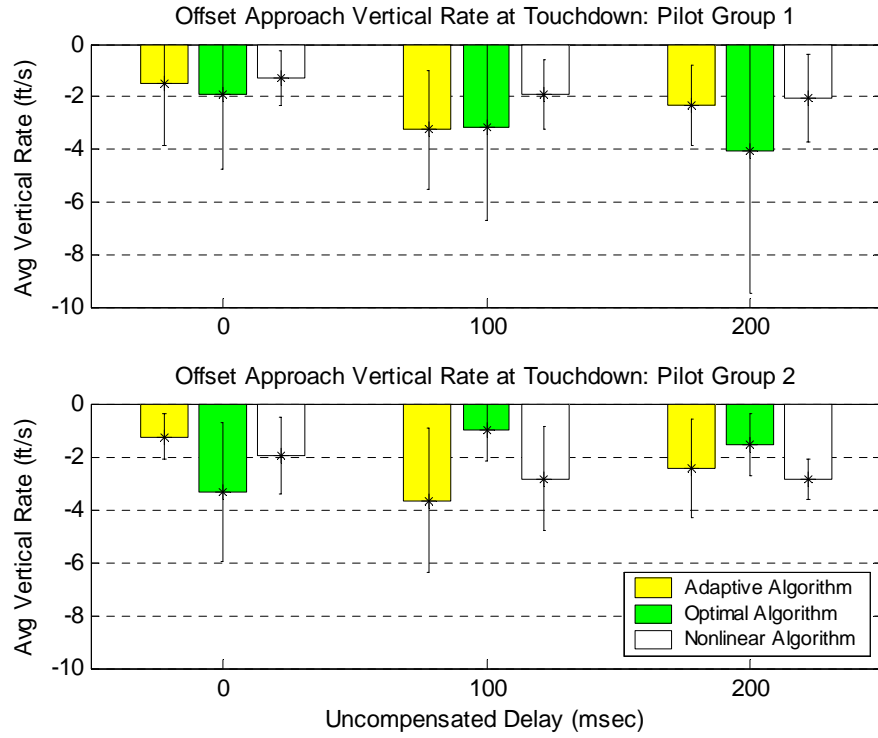
For the offset approach, the control input integral power for Pilot Group 2 was about the same as Pilot Group 1, with the optimal algorithm showing less power with the 100 and 200 msec delay conditions. These results are shown in Figure 5.14. The average PSD for Group 2 are given in Figures B.10 to B.12.



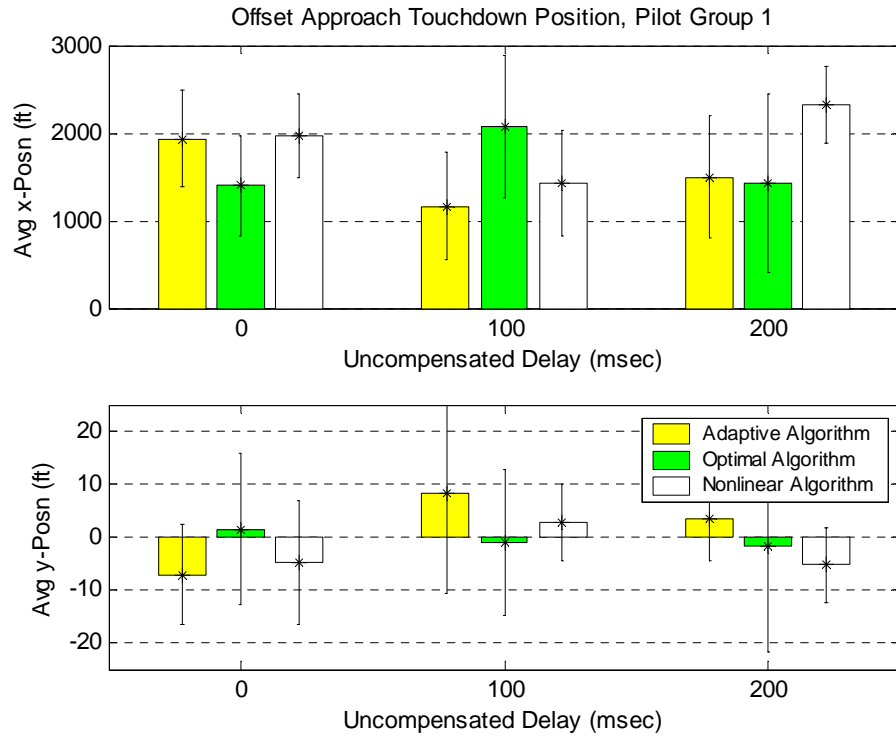
**Figure 5.14. Offset Approach, Control Input Integral Power, Pilot Group 2.**

Figure 5.15 shows the average vertical rate at the touchdown for both Pilot Group 1 and Pilot Group 2. The vertical rates are higher as compared to the straight-in approach, which would indicate the pilots having less control of the aircraft upon touchdown. There was no significant difference in magnitude between the two groups. While the nonlinear algorithm produced the lowest vertical rates for Pilot Group 1, no significant difference among algorithms was revealed for either pilot group. Also, investigation of the runway touchdown coordinates shown in Figures 5.16 and 5.17, did

not yield any significant or noticeable difference among the cueing algorithms, although similar to the straight-in approach the pilots in Group 1 tended to land about an average of 300 feet further down the runway.



**Figure 5.15. Offset Approach, Vertical Rate at Touchdown.**



**Figure 5.16. Touchdown Coordinates, Offset Approach, Pilot Group 1.**

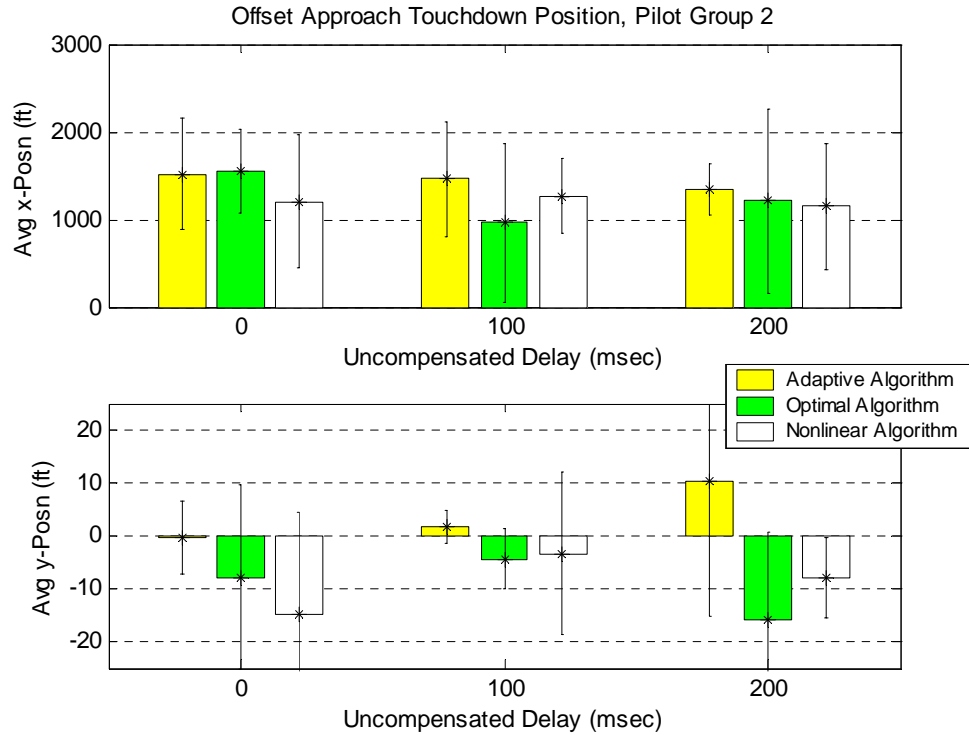


**Figure 5.17. Touchdown Coordinates, Offset Approach, Pilot Group 2.**

A number of pilots noticed and commented on the different sensed levels of turbulence between the adaptive and the optimal/nonlinear algorithms with the augmented turbulence channel [2]. In general, they felt that the new algorithms produced a more realistic feel of turbulence, while the adaptive algorithm produced a high-frequency “washboard” effect that was uncharacteristic of severe turbulence in aircraft.

Figure 5.18 shows the average PSD of the simulator z-axis displacement for both approach maneuvers with zero delay for Pilot Group 1. For the offset approach, the nonlinear algorithm produced a high peak at about 0.06 Hz that is more than twice as high as the optimal algorithm, and significantly higher than the adaptive algorithm. This additional vertical aircraft motion produced by the turbulence will increase the pilot’s workload in controlling the aircraft.

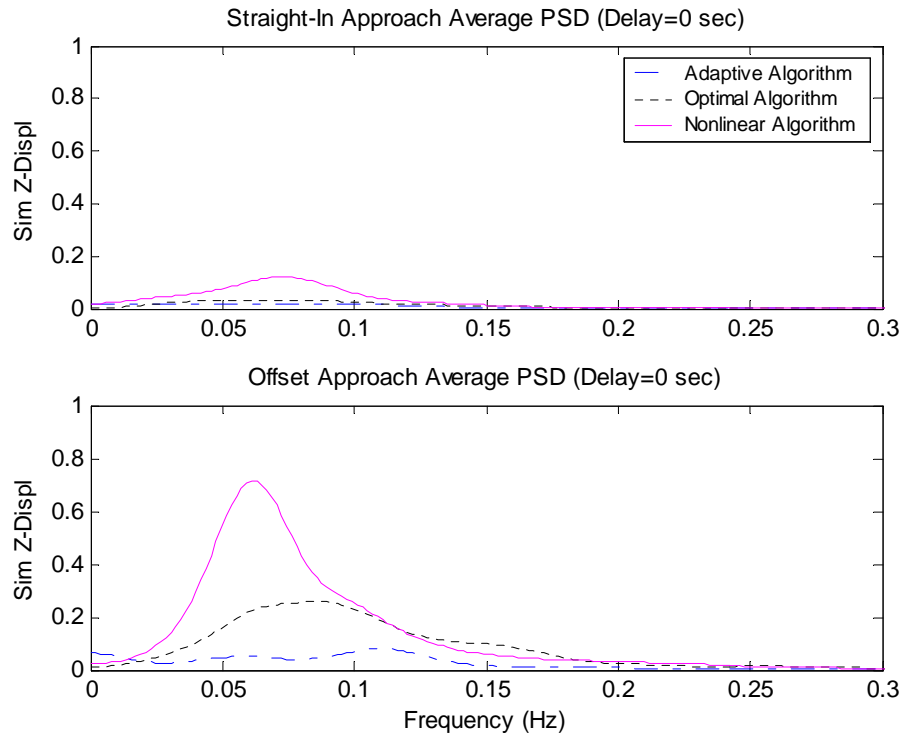


**Figure 5.18. Simulator Z-Axis Average PSD for Approach Maneuvers, Pilot Group 1.**

The straight-in approach (without turbulence) showed a similar trend; however the average PSD for the nonlinear algorithm is much lower, with a less significant increase in magnitude compared to the offset approach with severe turbulence. Pilot Group 2 produced very similar results for both maneuvers.

### 5.2.3. Takeoff without Engine Failure

The PSD and control input integral power for takeoff maneuvers include the liftoff portion of the maneuver from the point the aircraft leaves the runway up to an altitude of 2000 feet, and does not include the initial “throttle-up” and takeoff roll portion of the maneuver. Figure 5.19 shows the control input integral power for Pilot Group 1. The pitch stick power is invariant among either the cueing algorithms or the delay, with the standard deviations small.

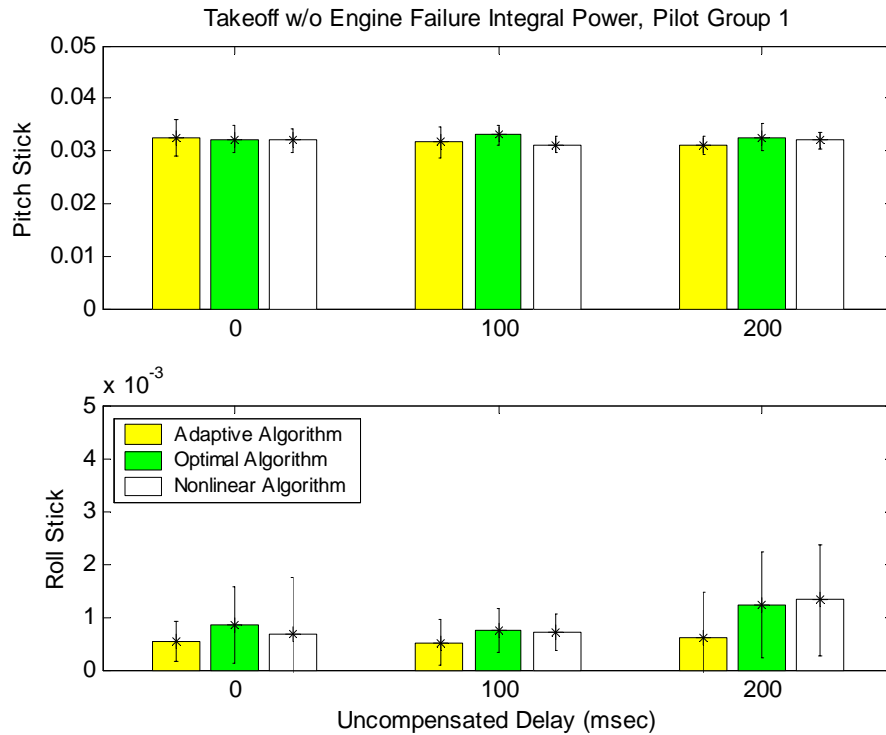


**Figure 5.19. Takeoff without Engine Failure, Control Input Integral Power, Pilot Group 1.**

Without engine failure, the roll stick power is low. For delay conditions of zero and 100 msec, the power was not significantly different among the cueing algorithms, while with 200 msec delay the optimal and nonlinear algorithms are slightly higher.

Figure 5.20 shows the control input integral power for Pilot Group 2. The pitch stick power was almost unchanged for all cases as compared to Pilot Group 1. For the zero delay condition, the optimal and nonlinear algorithms showed a slight increase in the roll stick magnitude. With delay, the power tends to be higher, in particular with the optimal algorithm with 100 ms delay.

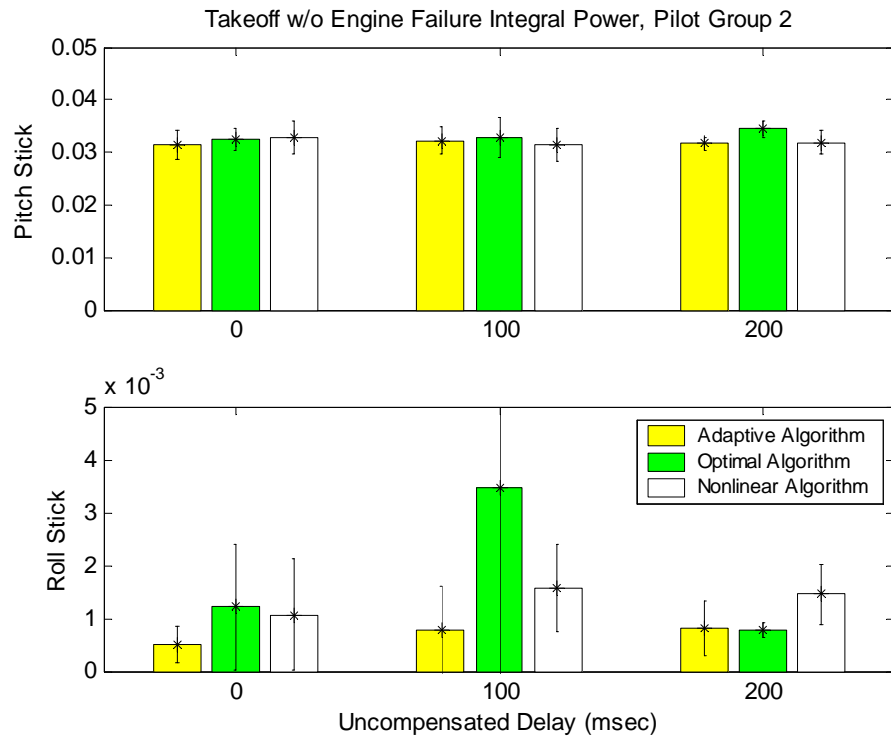
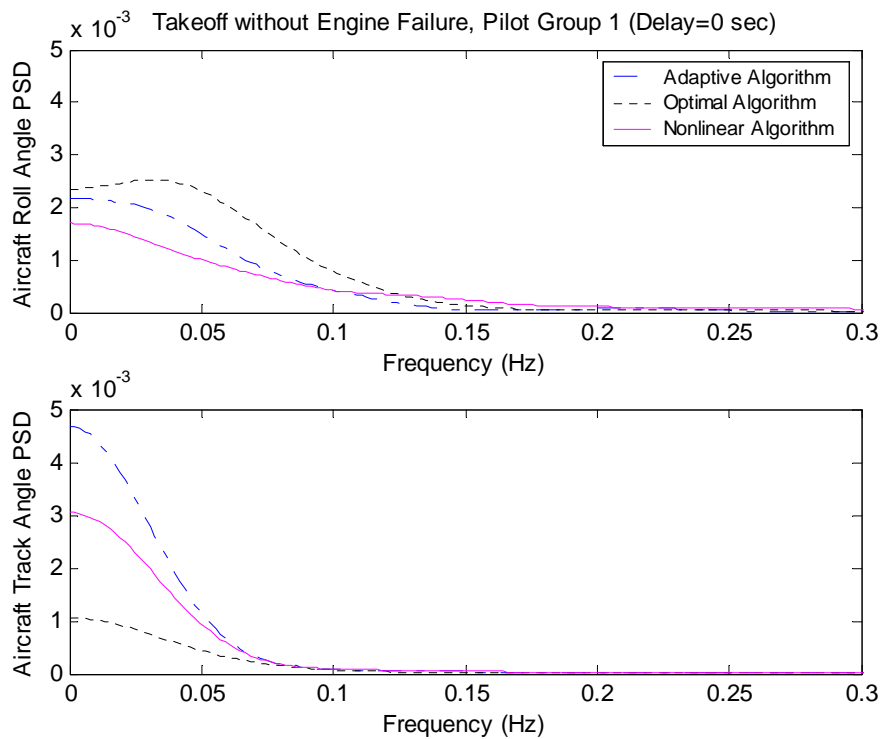


**Figure 5.20. Takeoff without Engine Failure, Control Input Integral Power, Pilot Group 2.**

The average PSD for Pilot Group 1 in Figures B.13 to B.15 revealed that most of the roll stick control activity is below 0.4 Hz. Similar results occurred for Pilot Group 2 as shown in Figures B.16 to B.18. Increases in PSD usually occurred in the same

frequency range. The exception is the optimal algorithm with 100 msec delay. In this case a large peak occurred between 0.35 and 0.45 Hz that may have been the result of an unnoticed pilot-induced oscillation for Pilot 6.

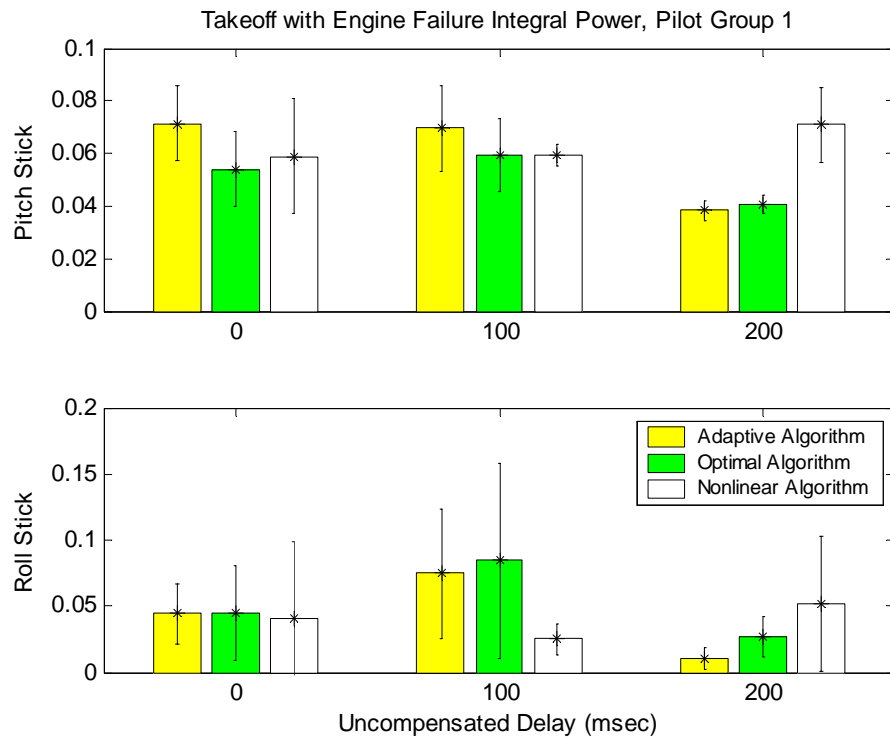
Figure 5.21 shows the average PSD of the aircraft roll and track angles for Pilot Group 1 with zero delay. The track angle is the angle between the nose and velocity vector of the aircraft. Note that the roll angle magnitude is small and does not vary much among algorithms. The track angle magnitude is also small, but showed some variation among the cueing algorithms. However, this will have little influence on the pilot workload since without engine failure, the rudder pedal activity was negligible.



**Figure 5.21. Takeoff without Engine Failure, Aircraft Roll and Track Angle Average PSD, Pilot Group 1.**

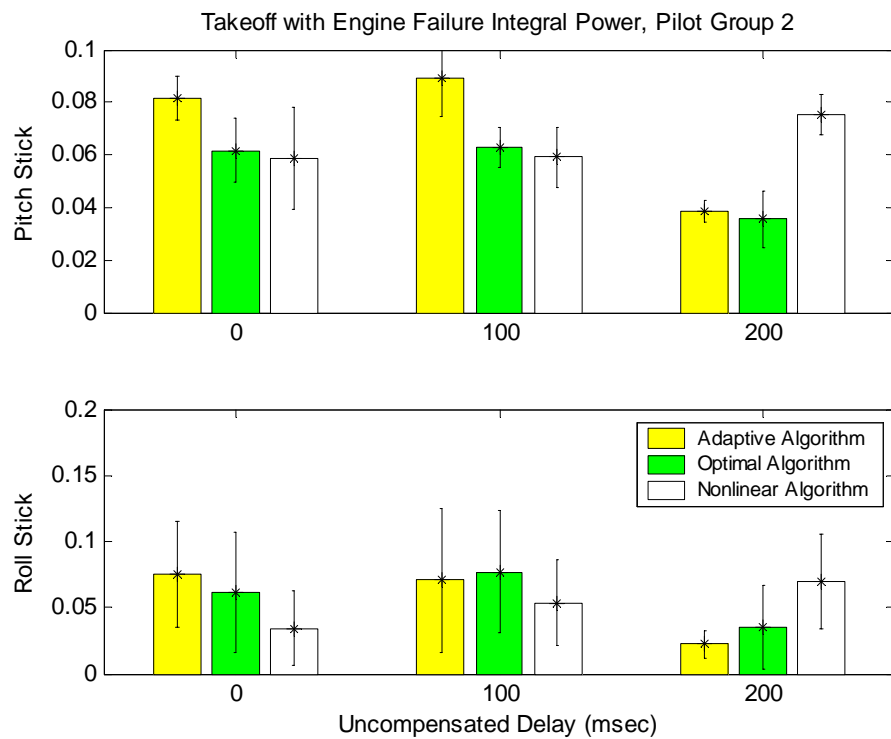
#### 5.2.4. Takeoff with Engine Failure

Figure 5.22 shows the pitch stick and roll stick control input integral power for Pilot Group 1. For delay conditions of zero and 100 msec, the pitch stick power was noticeably higher for the adaptive algorithm, with both the optimal and nonlinear algorithms yielding similar results. For the zero delay condition, the roll stick power was about the same for all three algorithms, while for 100 msec delay the nonlinear algorithm remained unchanged and both the adaptive and optimal algorithms noticeably increased. The 200 msec delay condition shows unexpected reductions in the pitch and roll stick power for both the adaptive and optimal algorithms, while the nonlinear algorithm power remained about the same as the zero and 100 msec delay conditions.



**Figure 5.22. Takeoff with Engine Failure, Control Input Integral Power, Pilot Group 1.**

The control input integral power for Pilot Group 2, shown in Figure 5.23, yielded similar results for the pitch stick for zero and 100 msec delay conditions. The roll stick showed higher power for the adaptive and optimal algorithms with zero delay, and the nonlinear algorithm power about the same as for Pilot Group 1. Figure B.22 shows the average PSD for the zero delay condition for Pilot Group 2. Note that the adaptive algorithm produced the highest low-frequency PSD for both the pitch stick and the roll stick. The nonlinear algorithm resulted in the lowest low-frequency roll stick PSD. Similar behavior compared to Pilot Group 1 for the 200 msec delay condition was also observed for both the pitch and roll stick power.



**Figure 5.23. Takeoff with Engine Failure, Control Input Integral Power, Pilot Group 2.**

The average PSD for Pilot Group 1 in Figures B.19 to B.21 revealed that most of the pitch stick activity is at low frequencies. For zero and 100 msec delay cases, the

adaptive algorithm has the highest low-frequency peak, while for 200 msec delay the peak is highest for the nonlinear algorithm. These results correspond to the control input integral power shown in Figure 5.22. The roll stick average PSD, in relation to the control input integral power, is also apparent, with the nonlinear algorithm showing the lowest peak among the algorithms for 100 msec delay, and the highest peak for 200 msec delay. Similar observations from Figures B.22 to B.24 can be made for Pilot Group 2 in relation to Figure 5.23.

The rudder pedal control input integral power for Pilot Groups 1 and 2 is shown in Figure 5.24. Note that the condition with zero delay showed much larger power with the adaptive algorithm, with the nonlinear algorithm being slightly higher compared to the optimal algorithm for both pilot groups.

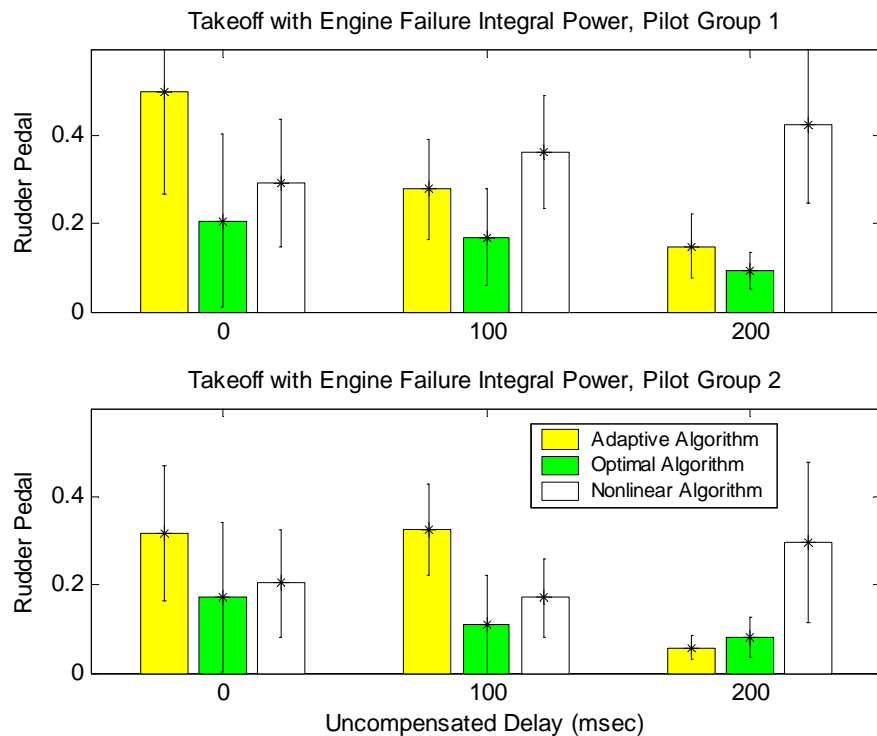


**Figure 5.24. Takeoff with Engine Failure, Rudder Pedal Integral Power.**

Increasing the delay to 100 msec showed the rudder pedal power for both the optimal and nonlinear algorithms unchanged for both pilot groups, with a reduction observed for the adaptive algorithm with Pilot Group 1. For the 200 msec delay condition, both pilot groups yielded a reduction with the rudder pedal power for the adaptive and optimal algorithms, while the nonlinear algorithm increased slightly compared to the zero and 100 msec conditions.

The average PSD for the rudder pedal, shown in Figures B.25 to B.27, showed the PSD to be predominantly low frequency content. The peak was noticeably higher for the adaptive algorithm for both pilot groups with zero and 100 msec delay, and lowest for the optimal algorithm. With 200 msec delay, the nonlinear algorithm shows the highest peak. These results compare to the control input integral power shown in Figure 5.24.

Figure 5.25 shows the average PSD of the roll angle and track angle for Pilot Group 1 with zero delay. Note that with the addition of an engine failure, both the roll and track angles significantly increase for all algorithms. The roll angle for the adaptive algorithm is about twice the magnitude at low frequencies compared to the optimal and nonlinear algorithms. The track angle showed a more significant increase in low-frequency content for the adaptive algorithm by a factor of seven, with the optimal and nonlinear algorithms yielding similar results. Pilot Group 2 yielded similar results for the aircraft roll and track angles.

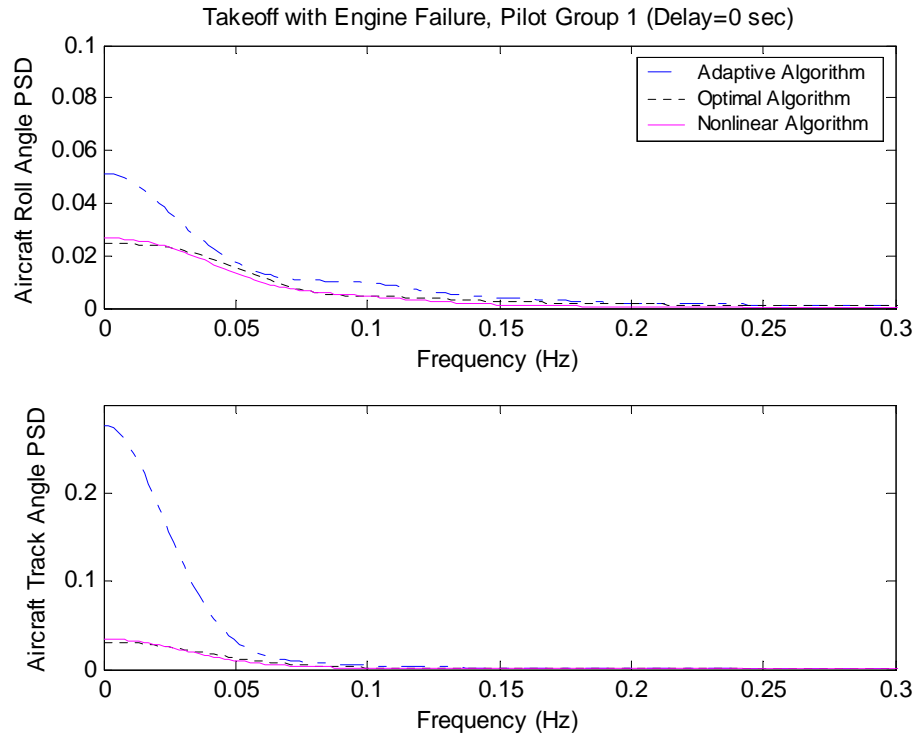


**Figure 5.25. Takeoff with Engine Failure, Aircraft Roll and Track Angle Average PSD, Pilot Group 1.**

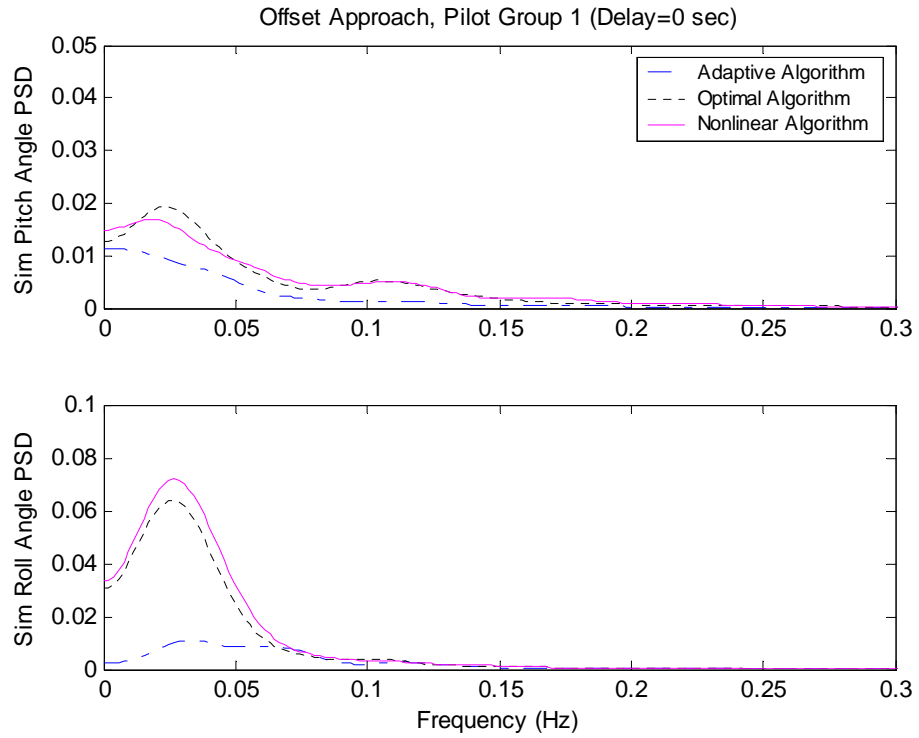
### 5.3. Simulator Attitude Coherence

Figure 5.26 shows the average simulator pitch and roll angle PSD for Pilot Group 1 for the offset approach with zero delay. The optimal and nonlinear algorithms resulted in increased PSD for both the pitch and roll angles compared to the adaptive algorithm. The simulator roll angle PSD increase was more significant, with a peak near the same frequency as the aircraft roll angle PSD shown in Figure 5.13.

Figure 5.27 shows the average simulator pitch and roll angle coherence defined in Section 5.1 and Eq. (4.1). In Figure 5.27, the optimal and nonlinear algorithms showed significantly less coherence for the low frequency range near the roll angle peak frequency. One reason for this may be the augmented turbulence cue implemented for both algorithms. The increased heave cues shown in Figure 5.18 may be producing

additional "observation noise" in the pilot's roll stick response that is uncorrelated with the simulator roll cues. The pitch angle shows increased coherence for both the optimal and nonlinear algorithms up to 0.1 Hz followed by reduced coherence at mid-frequencies up to 0.4 Hz. Figure 5.28 shows the average simulator pitch and roll angle PSD for Pilot Group 1 for the takeoff with engine failure and zero delay. The simulator roll angle PSD for the adaptive algorithm was about twice as large at low frequencies compared to the adaptive and nonlinear algorithms.

In Figure 5.29, the nonlinear algorithm showed less coherence at low frequencies compared to the adaptive algorithm. Less coherence may indicate that the pilot is more effectively sensing the disturbance, i.e. the engine failure as observation noise not correlated with the simulator roll cues. The pitch angle PSD is larger for the optimal algorithm compared to the adaptive algorithm, but with a reduced coherence.



**Figure 5.26. Simulator Attitude Average PSD for Offset Approach, Pilot Group 1 with Zero Delay.**

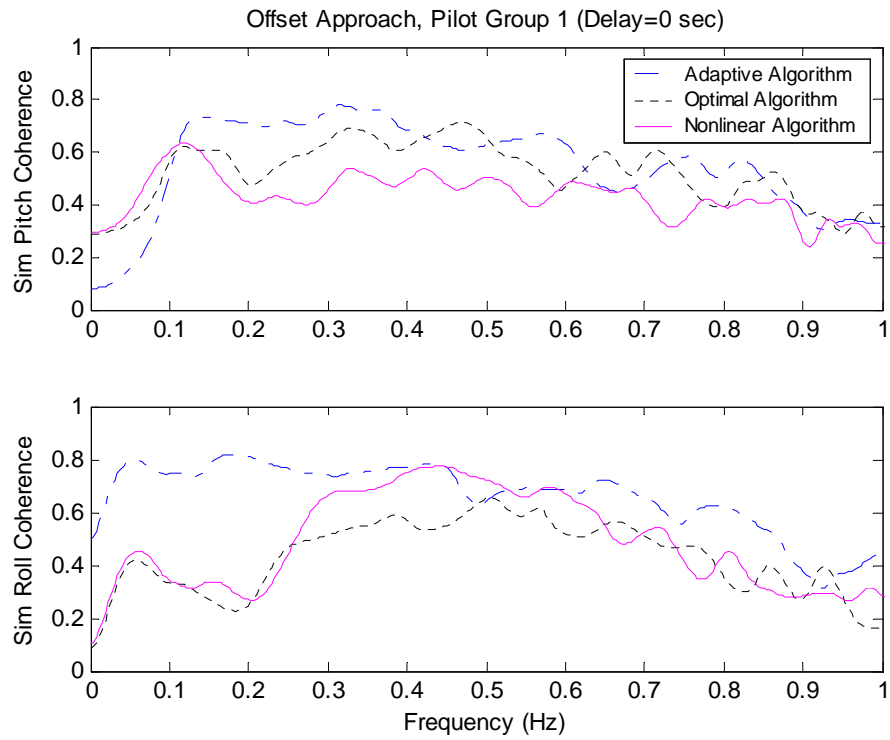


**Figure 5.27. Simulator Average Coherence for Offset Approach, Pilot Group 1 with Zero Delay.**

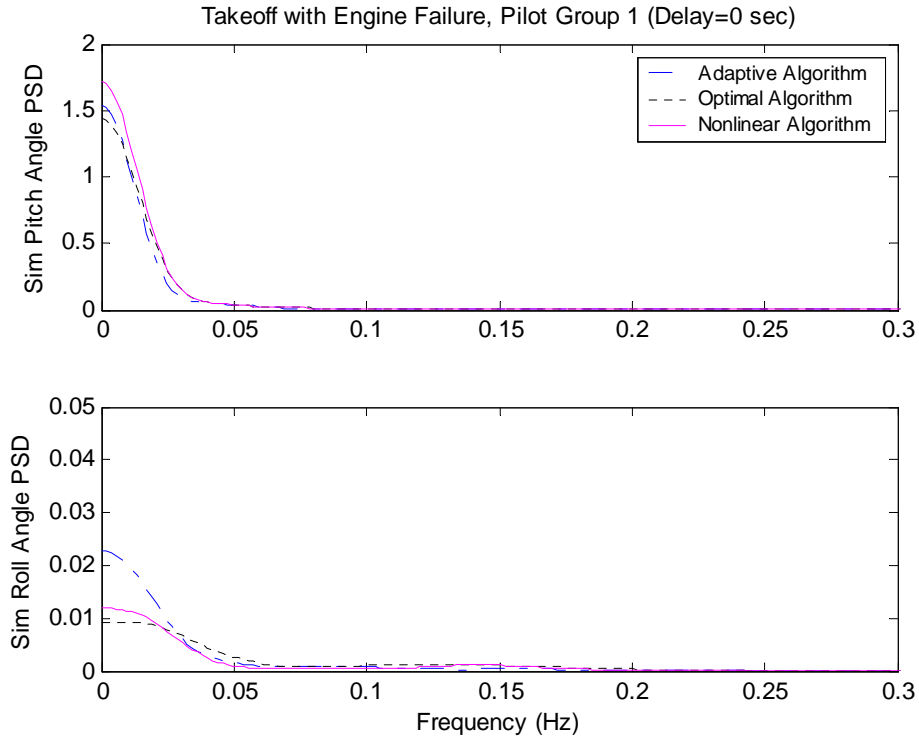


**Figure 5.28. Simulator Attitude Average PSD for Takeoff with Engine Failure, Pilot Group 1 with Zero Delay.**

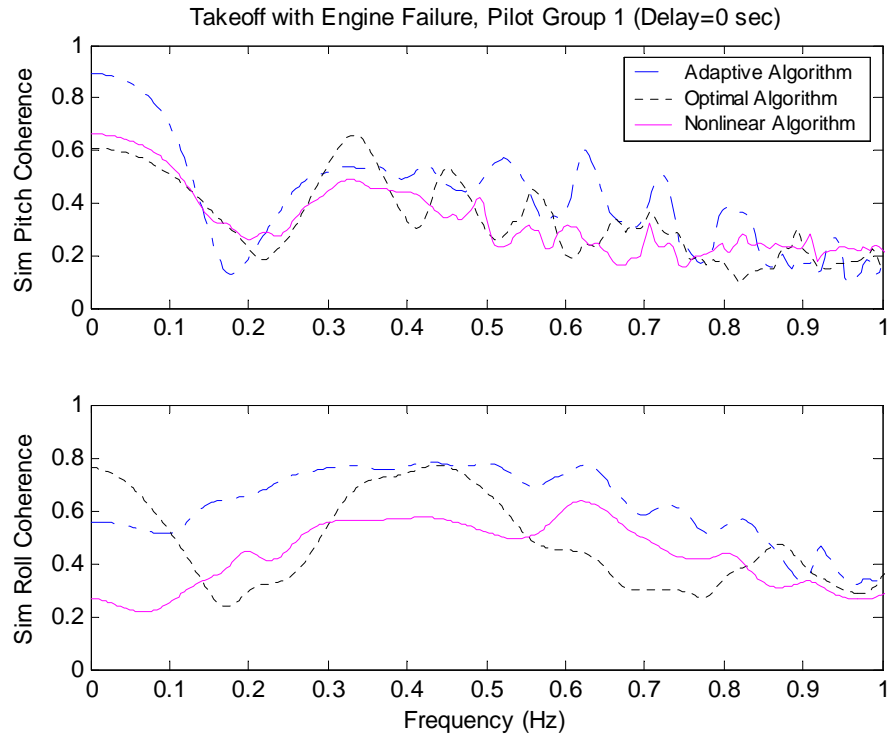


**Figure 5.29. Simulator Average Coherence for Takeoff with Engine Failure, Pilot Group 1 with Zero Delay.**

Both the straight-in approach and the takeoff without engine failure resulted in simulator roll angles of relatively small magnitude compared to the pitch angles. The average simulator attitude PSD and coherence for the straight-in approach are shown in Appendix B, Figures B.28 and B.29. The average coherence was about the same for all three cueing algorithms for both pitch and roll. The pitch angle PSD was the highest for the nonlinear algorithm, with the roll PSD for both the optimal and nonlinear algorithms being twice as large as the adaptive algorithm. The average simulator attitude PSD and coherence for the takeoff without engine failure is shown in Appendix B, Figures B.30 and B.31. The average coherence for the pitch angle was about the same for all three algorithms, but for the roll angle the optimal and nonlinear algorithms resulted in less coherence compared to the adaptive algorithm. The nonlinear algorithm resulted in the largest roll angle PSD with a peak of about 0.16 Hz.

The coherence based upon the aircraft attitude for each of the four maneuvers for Pilot Group 1 (with zero delay) is given in Figures B.32 to B.35. In each case the coherence was about the same for all algorithms. The roll stick was well correlated to the aircraft roll angle at frequencies from 0.1 to 0.5 Hz, then gradually decreased.

## 6. Summary of Results

By aggregating pilots into groups with similar control technique and instrument scan pattern, NASA TLX ratings revealed differences in workload and behavior among the pilot groups. Pilot Group 3 resulted in the highest workload for all maneuvers, most noticeably with the offset approach and the takeoff with engine failure. By analyzing the pilot ratings in this manner, the pilots with the most erratic and outlying behavior (Pilot Group 3) could be identified. Pilot Group 2 showed a small, insignificant TLX increase compared to Pilot Group 1. The large standard deviations shown for each maneuver illustrate that even with aggregation, the pilot behavior remains non-homogeneous within each pilot group.

Analysis of the TLX ratings with delay conditions reveals some noticeable trends among the cueing algorithms. For the straight-in approach, offset approach, and takeoff maneuver without engine failure, the nonlinear algorithm produces about the same or higher workload compared to the adaptive algorithm for zero delay, but less workload with 100 and 200 msec delay. The optimal algorithm results in the highest workload for these maneuvers in the presence of delay. For the takeoff with engine failure, the nonlinear algorithm produces the lowest workload for both zero and 100 msec delay.

By analyzing the integral power and the average PSD separately for Pilot Groups 1 and 2, differences among either pilot groups or cueing algorithms become more noticeable. For the straight-in approach, Pilot Group 1 showed less power and only small differences among the cueing algorithms. Pilot Group 2 resulted in increased pitch stick power for all algorithms that tended to be larger for the optimal and nonlinear algorithms. The roll stick power also increased for Pilot Group 2, with pilot-induced oscillations

contributing to increased power and pilot variability for the optimal and nonlinear algorithms. Similarly, the roll stick power for the takeoff without engine failure showed less control input integral power and variation among the cueing algorithms for Pilot Group 1, while Pilot Group 2 resulted in increased power and variability, most noticeably for the optimal algorithm.

Differences in control input integral power among the pilot groups were less noticeable with the offset approach. Both the optimal and nonlinear algorithms showed an increase in power compared to the adaptive algorithm. A major contributor to the integral power resulted from the augmented vertical cues due to turbulence. In response to realistic turbulence, the pilot will increase his workload and generate more roll and pitch stick activity. A significant increase in the simulator roll angle PSD is also observed for both algorithms, but is less correlated with the control response of the roll stick due to the disturbance effects of the turbulence.

Analysis of the piloted performance for both the straight and offset approaches with both the vertical velocity upon touchdown and the runway position did not yield any noticeable difference among the cueing algorithms. Pilot Group 1 tended to “float” further down the runway and land with a lower vertical velocity in comparison to Pilot Group 2. Two additional performance parameters, the glide slope error and localizer error, were also investigated. These parameters did not show any noticeable difference among either the cueing algorithms or the pilot groups.

The takeoff with engine failure maneuver showed a reduction in control activity for the optimal and nonlinear algorithms with both zero and 100 msec delay conditions. The nonlinear algorithm produced the least amount of roll stick power, and is less

correlated with the simulator roll angle. The optimal algorithm resulted in less rudder pedal power for both conditions. With the 200 msec delay condition, the nonlinear algorithm produced an expected increase in control activity, indicating the pilots are detecting the engine failure and increasing their workload to correct the aircraft motion. The reduced workloads for the adaptive and optimal algorithms for this condition indicate the pilots may be getting less of the sensory information needed to completely correct the engine failure disturbance.

This page intentionally left blank.

## 7. Conclusions

Piloted performance tests revealed some noticeable differences between the cueing algorithms, but these differences were not always statistically significant. From the NASA TLX ratings, the group of pilots observed to have the most erratic control behavior resulted in the largest rated workload. Further analysis of the TLX ratings with the remaining pilots shows, in most cases, less workload and variation among pilots with the nonlinear algorithm. Performance variations among the algorithms were better observed from power spectral density (PSD) and control input integral power analysis. For the simpler maneuvers, the straight-in approach and the takeoff without engine failure, the pilots with the “best” control technique showed similar performance for each algorithm. Differences among algorithms become more apparent for the pilots with more erratic control behavior, especially with pilot-induced oscillations for both the optimal and nonlinear algorithms.

Both of the complex maneuvers, the offset approach with turbulence and the takeoff with engine failure, showed more uniform performance among pilots with varying control technique. Increased control input integral power for the optimal and nonlinear algorithms, observed for the offset approach, resulted from additional vertical turbulence cues that some pilots felt were more realistic compared to the adaptive algorithm. Lower workload, for zero and 100 ms delay conditions, compared to the adaptive algorithm was observed for the takeoff with engine failure, with the optimal algorithm showing the least amount of rudder pedal and the nonlinear algorithm showing the least amount of roll stick activity.

The piloted test results yielded a large amount of variability in pilot workload and performance that was a consequence of the availability of only a small population of eleven pilots having a wide range of flight experience. The aggregation of pilot groups by observed similarities in control technique and instrument scan pattern given in Table 5.1 revealed noticeable trends among both pilot groups and cueing algorithms. However, large variations in pilot performance within each pilot group persisted, resulting in the differences among cueing algorithms appearing ambiguous and insignificant. Analysis of two pilots with Boeing 757-200 experience (from the most disciplined group) showed a reduction in the variation in pilot behavior, most noticeably with the takeoff with engine failure. Such an improvement to pilot testing was suggested by Go, et al. [13]. The NASA/FAA Boeing 747-400 motion system tests conducted by Go, et al. utilized a large, homogenous population of forty pilots, all of whom were current Boeing 747-400 captains and first officers.

Reducing the nonlinear gains for the optimal algorithm (surge) and the nonlinear algorithm (surge and pitch) was necessary so that the takeoff could be flown within the 60-inch actuator extension limits and low bandwidth (2-Hz) of the Langley Visual Motion Simulator (VMS). However, gain reductions contribute to degradation in pilot performance that was observed most frequently with the straight-in approach. Implementation of the optimal and nonlinear algorithms on a platform with increased actuator extensions would allow for increased gains, thus resulting in improved pilot performance. One such motion platform is located in the Cockpit Motion Facility (CMF) [14], shown in Figure 7.1, presently being erected at the NASA Langley Research Center.

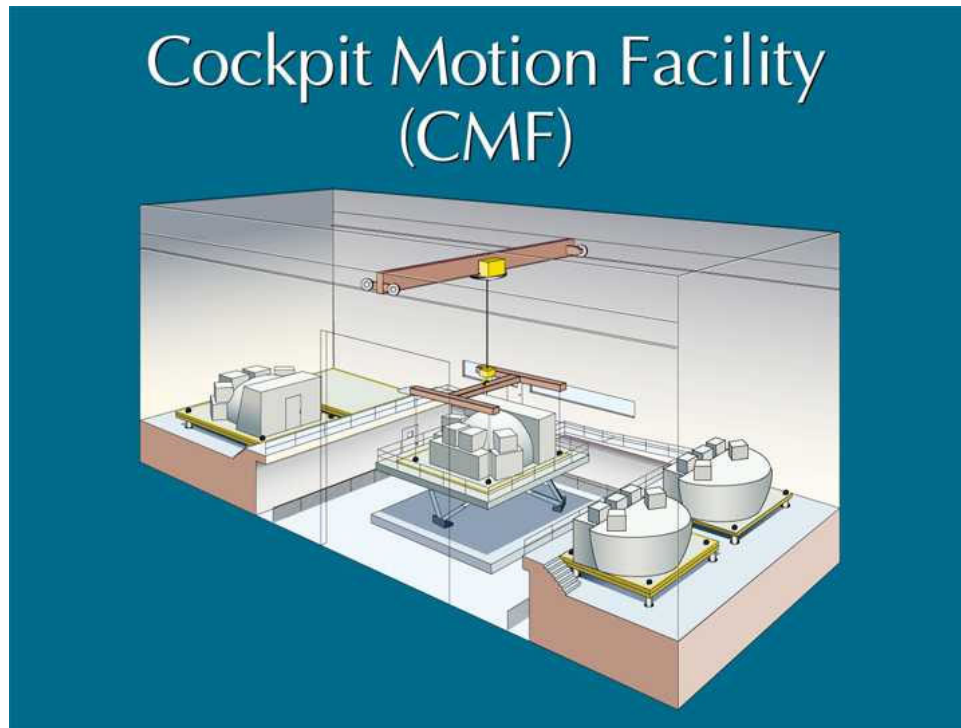


**Figure 7.1. NASA Langley Cockpit Motion Facility (CMF).**

The Cockpit Motion Facility is made up of one motion system site and four fixed-base sites. The motion system site contains a six-degree-of-freedom state-of-the-art synergistic motion base with 76-inch actuator extensions. The four fixed-base sites provide homes for the simulator cockpits when they are not resident on the motion system. Each cockpit has its own visual display system and all cockpits share Evans and Sutherland ESIG 3000 image generators.

Both the optimal and nonlinear algorithms along with the NASA adaptive algorithm will be implemented on the CMF. Pilot tuning of the nonlinear gains, similar to that previously done for the new algorithms on the VMS, will be performed.

The use of signal processing and power spectral density (PSD) techniques to analyze pilot performance and workload proved to be quite beneficial. Variations in pilot

performance that were less noticeable with the quasi-objective NASA TLX method, e.g. pilot-induced oscillations, could be better discriminated from PSD and control input integral power analysis. These analyses revealed a noticeable improvement in workload on the takeoff with engine failure with reduced roll stick activity for the nonlinear algorithm. This improvement is due to the improved lateral motion cues transmitting more information from the simulator to the pilot. Pilots with more erratic control behavior also showed some tendency to generate pilot-induced oscillations on straight landings for the nonlinear algorithm, but noticeably less compared to the optimal algorithm. The pilot-induced oscillations are a function of the reduced surge and pitch gains needed to keep the simulator within its hardware limits. These results are expected to improve with implementation of the nonlinear algorithm on the Cockpit Motion Facility that will allow increased surge and pitch gains.

## Appendix A. Pilot Test Runs and Conditions

Nomenclature:

Cueing Algorithm: 0 Adaptive, 2 Optimal, 3 Nonlinear

Compensation: 0 without Compensation, 1 with Compensation

Engine Failure: 0 without Failure, 1 with Failure

**Table A.1. Straight-In Approach Runs 1 to 24**

Run	Delay (msec)	Cueing Algorithm	Compensation
1	100	2	0
2	100	3	1
3	50	3	1
4	200	3	0
5	0	3	1
6	50	3	0
7	200	0	0
8	200	2	0
9	0	2	0
10	50	0	0
11	0	0	0
12	0	3	0
13	100	3	0
14	200	3	1
15	0	2	1
16	100	0	0
17	50	0	1
18	50	2	0
19	200	0	1
20	100	2	1
21	200	2	1
22	50	2	1
23	100	0	1
24	0	0	1

**Table A.2. Offset Approach Runs 25 to 48**

Run	Delay (msec)	Cueing Algorithm	Compensation
25	200	2	1
26	200	3	1
27	200	2	0
28	50	0	0
29	0	3	1
30	100	3	1
31	100	2	0
32	200	3	0
33	50	3	1
34	0	2	0
35	50	3	0
36	50	2	1
37	0	2	1
38	0	3	0
39	50	0	1
40	100	0	1
41	100	3	0
42	200	0	1
43	200	0	0
44	50	2	0
45	100	0	0
46	0	0	0
47	0	0	1
48	100	3	1

**Table A.3. Takeoff Test Runs 49 to 72**

Run	Delay (msec)	Cueing Algorithm	Compensation	Failure	Altitude (ft)
49	100	3	1	0	0
50	200	2	1	0	0
51	0	2	0	1	800
52	100	2	0	0	0
53	100	2	0	2	400
54	50	2	1	2	600
55	100	0	0	1	200
56	0	2	0	0	0
57	100	0	1	2	800
58	100	0	1	0	0
59	50	3	0	2	600
60	200	2	1	2	200
61	50	2	1	0	0
62	100	0	0	0	0
63	50	0	0	0	0
64	0	3	1	1	400
65	200	2	0	1	800
66	50	0	0	2	400
67	50	3	1	0	0
68	0	0	0	0	0
69	200	3	0	1	200
70	0	3	1	0	0
71	0	2	1	2	600
72	0	0	0	1	200

**Table A.4. Takeoff Test Runs 73 to 96**

Run	Delay (msec)	Cueing Algorithm	Compensation	Failure	Altitude (ft)
73	200	2	0	0	0
74	100	2	1	0	0
75	200	0	0	0	0
76	100	3	1	1	400
77	50	0	1	1	600
78	50	0	1	0	0
79	0	0	1	2	400
80	50	3	1	1	800
81	50	2	0	0	0
82	100	2	1	2	200
83	200	0	0	2	800
84	100	3	0	0	0
85	200	0	1	0	0
86	200	3	1	0	0
87	0	2	1	0	0
88	200	0	1	1	600
89	200	3	1	2	200
90	0	3	0	0	0
91	0	0	1	0	0
92	50	3	0	0	0
93	100	3	0	1	400
94	50	2	0	1	600
95	0	3	0	2	800
96	200	3	0	0	0

**Table A.5. Pilot Test Evaluation Sampled Variables.**

Variable	Units	Description
time	sec	time
pitch_stic, roll_stick, rudder_ped, throttle	%	pilot control inputs
altitude	ft	altitude
altitude_d	ft/sec	change in altitude
ias	ft/sec	indicated air speed
p, q, r	rad/sec	aircraft angular velocity
pdot, qdot, rdot	rad/sec/sec	aircraft angular acceleration
u, v, w	m/sec	aircraft linear velocity
udot, vdot, wdot	m/sec/sec	aircraft linear acceleration
track, theta, phi	deg	aircraft Euler angles and track angle
nx_ps, ny_ps, nz_ps	g	aircraft normal force at pilot station
sx, sy, sz	ft	Earth-frame positions (x,y,z) with respect to runway threshold
gs_error	deg	glide slope error
loc_error	deg	localizer error
volt_leg_[1:6]	volts	commanded leg lengths
lin_accel[1:6]	g	linear accelerometers (six)
pitchincl, rollincl	deg	inclinometer angles (roll and pitch)
com2_[xdd, ydd, zdd] (optimal)	m/sec/sec	commanded platform accelerations
comint2_[phid, thed, psid] (optimal)	rad/sec	commanded platform Euler rates
m1c_ssi(1:3) (optimal)	m	desired platform positions
m_betas(1:3) (optimal)	rad	desired platform Euler angles
[x, y, z]_motion (standard)	m	desired platform positions
[phi, the, psi]_motion (standard)	rad	desired platform Euler angles
u_gust, v_gust, w_gust		gust – magnitude & direction

**Table A.6. NASA TLX Subscale Rating Definitions.**

Title	Endpoints	Descriptions
<b>MENTAL DEMAND</b>	Low/High	How much mental and perceptual activity was required (e.g., thinking, deciding, calculating, remembering, looking, searching, etc.)? Was the task easy or demanding, simple or complex, exacting or forgiving?
<b>PHYSICAL DEMAND</b>	Low/High	How much physical activity was required (e.g., pushing, pulling, turning, controlling, activating, etc.)? Was the task easy or demanding, slow or brisk, slack or strenuous, restful or laborious?
<b>TEMPORAL DEMAND</b>	Low/High	How much time pressure did you feel due to the rate or pace at which the tasks or task elements occurred? Was the pace slow and leisurely or rapid and frantic?
<b>EFFORT</b>	Low/High	How hard did you have to work (mentally and physically) to accomplish your level of performance?
<b>PERFORMANCE</b>	Good/Poor	How successful do you think you were in accomplishing the goals of the task set by the experimenter (or yourself)? How satisfied were you with your performance in accomplishing these goals?
<b>FRUSTRATION LEVEL</b>	Low/High	How insecure, discouraged, irritated, stressed and annoyed versus secure, gratified, content, relaxed and complacent did you feel during the task?

## Appendix B. Pilot Group Average PSD and Coherence

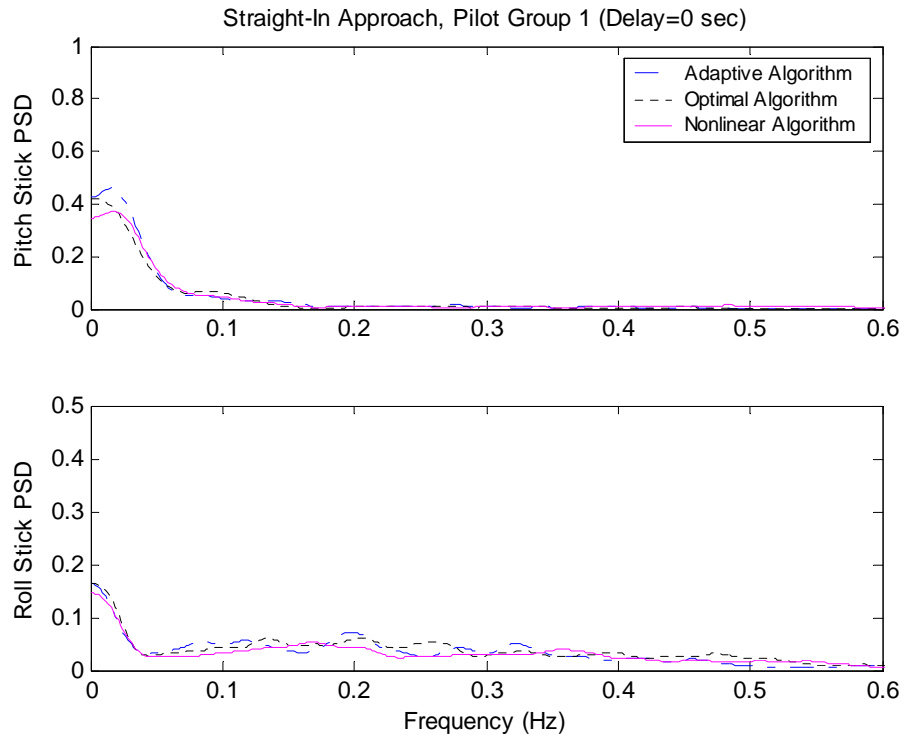


**Figure B.1. Straight-In Approach Average PSD, Pilot Group 1, No Delay.**

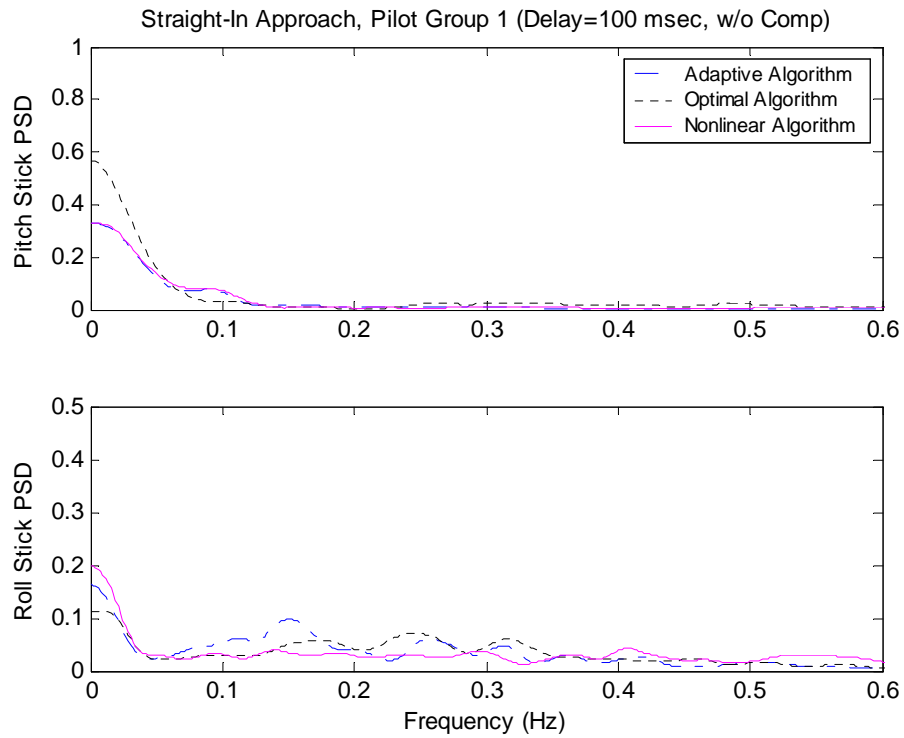


**Figure B.2. Straight-In Approach Average PSD, Pilot Group 1, Delay 100 msec.**

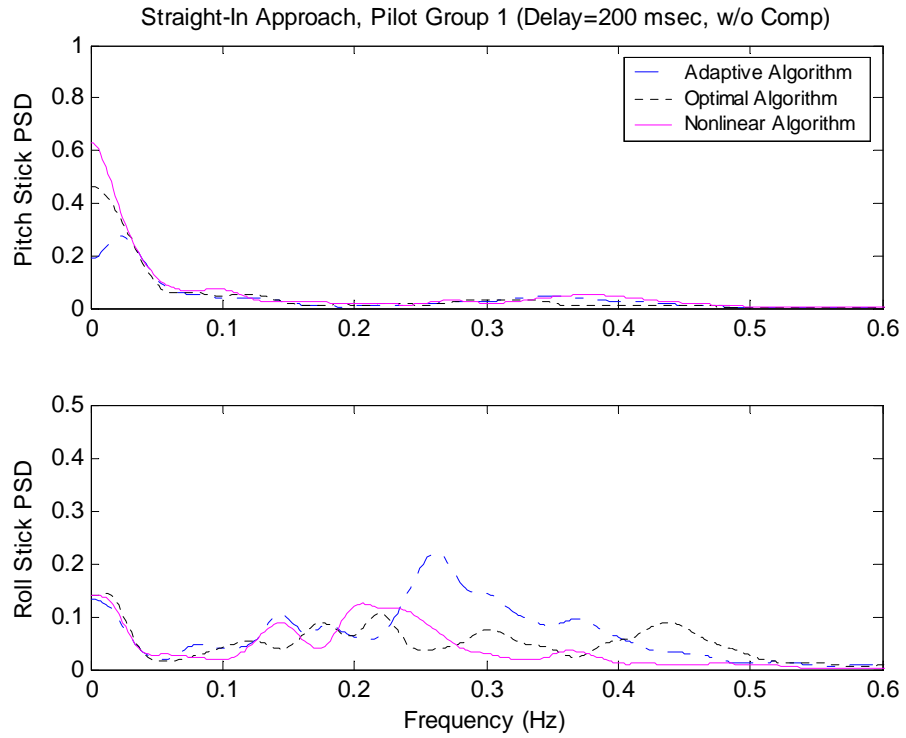


**Figure B.3. Straight-In Approach Average PSD, Pilot Group 1, Delay 200 msec.**

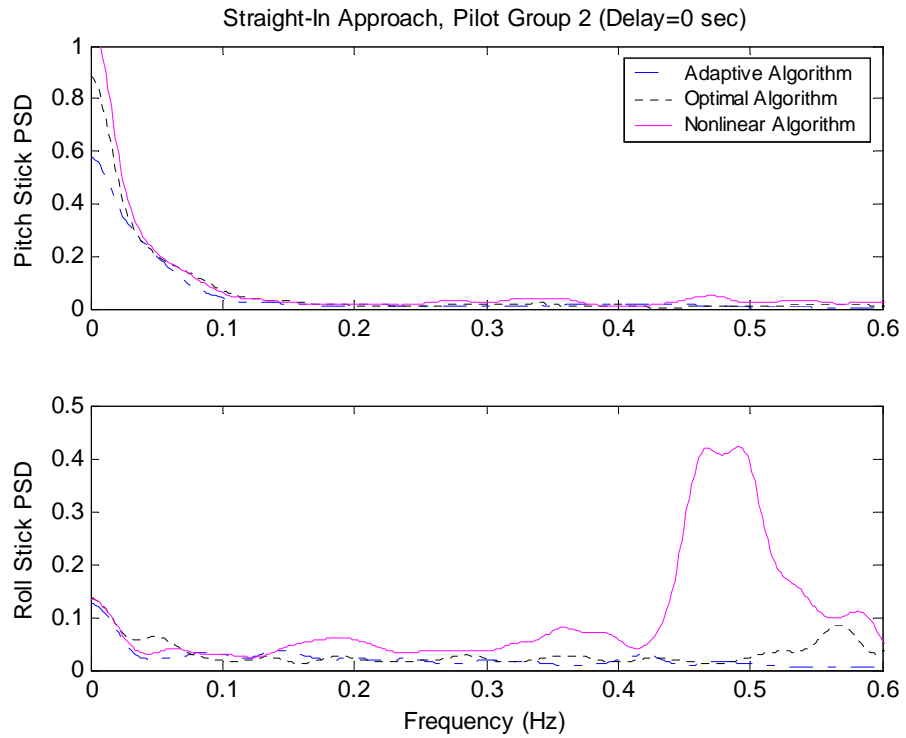


**Figure B.4. Straight-In Approach Average PSD, Pilot Group 2, No Delay.**

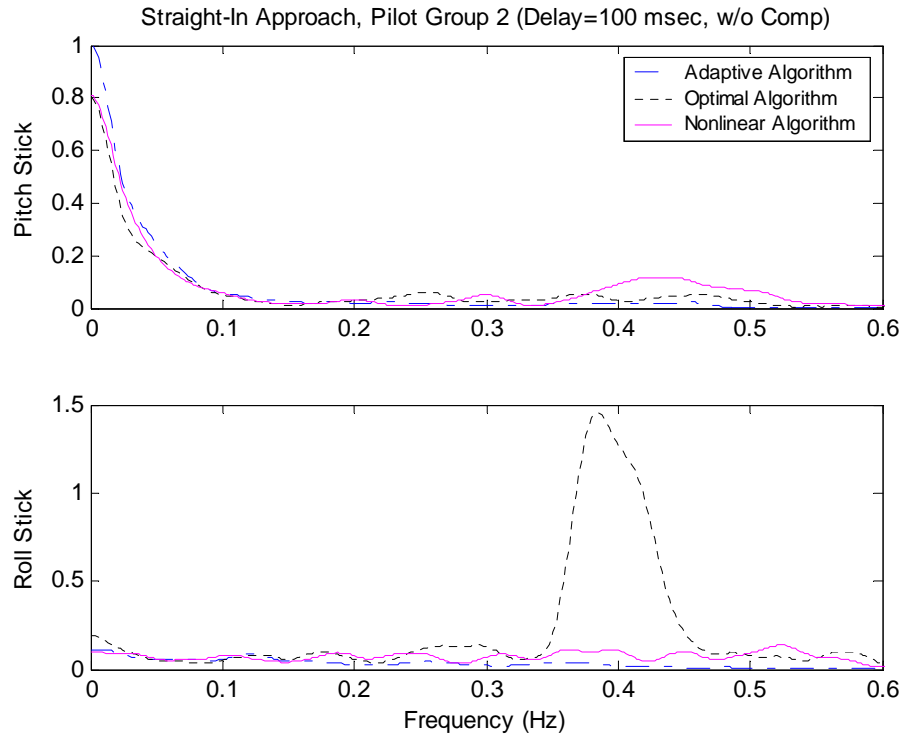


**Figure B.5. Straight-In Approach Average PSD, Pilot Group 2, Delay 100 msec.**

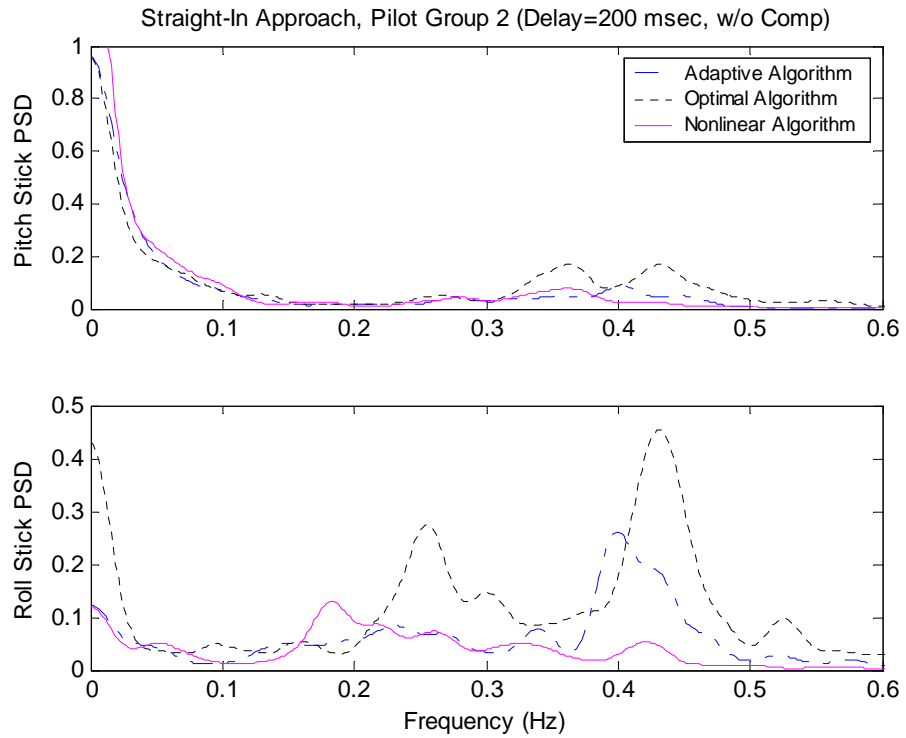


**Figure B.6. Straight-In Approach Average PSD, Pilot Group 2, Delay 200 msec.**

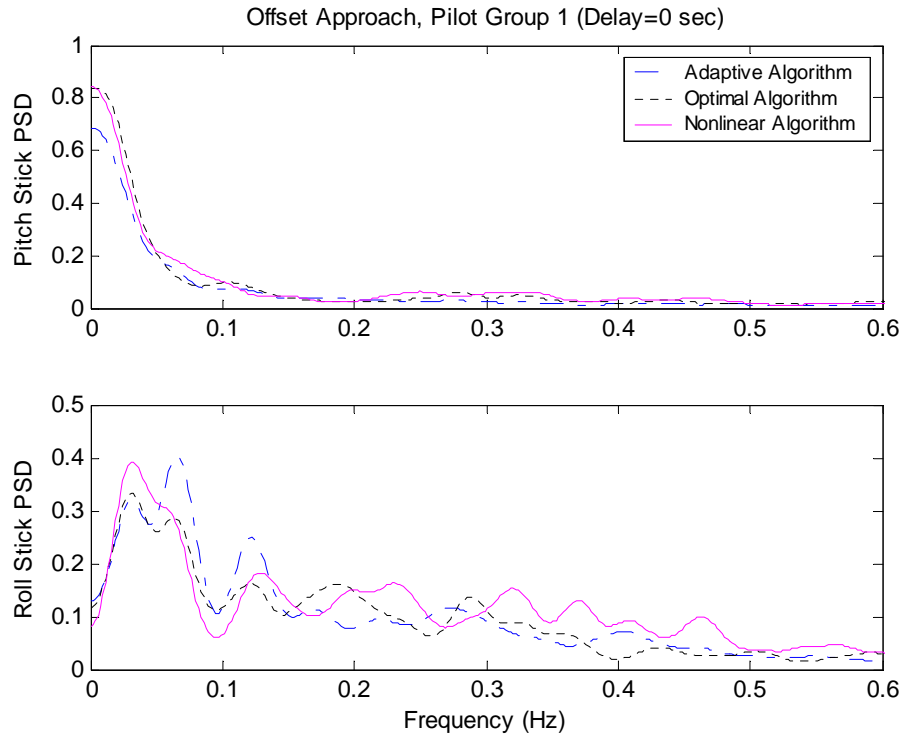


**Figure B.7. Offset Approach Average PSD, Pilot Group 1, No Delay.**

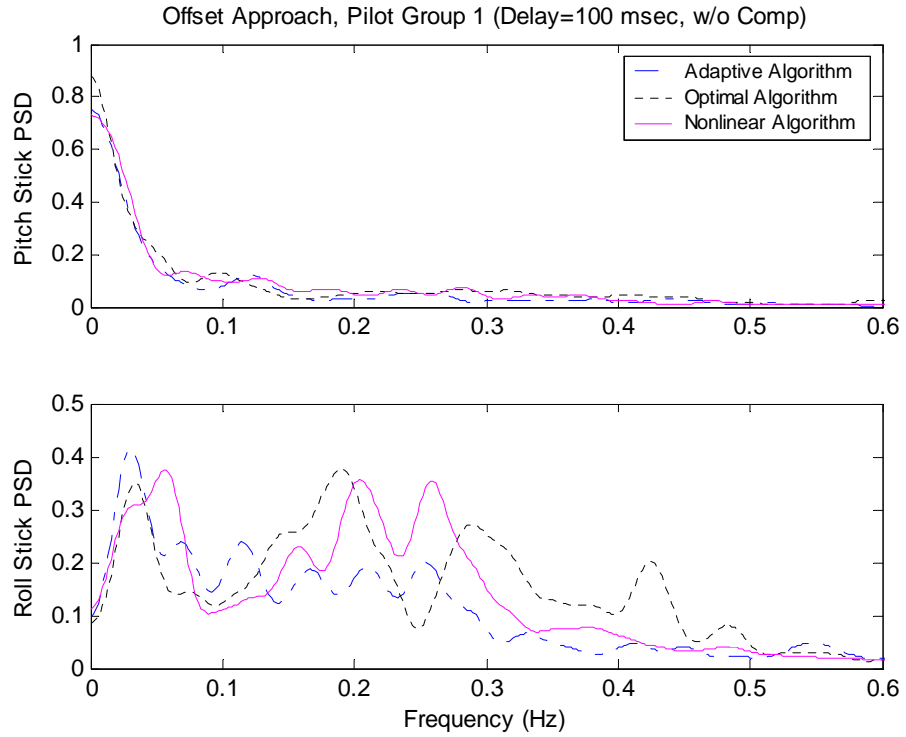


**Figure B.8. Offset Approach Average PSD, Pilot Group 1, Delay 100 msec.**

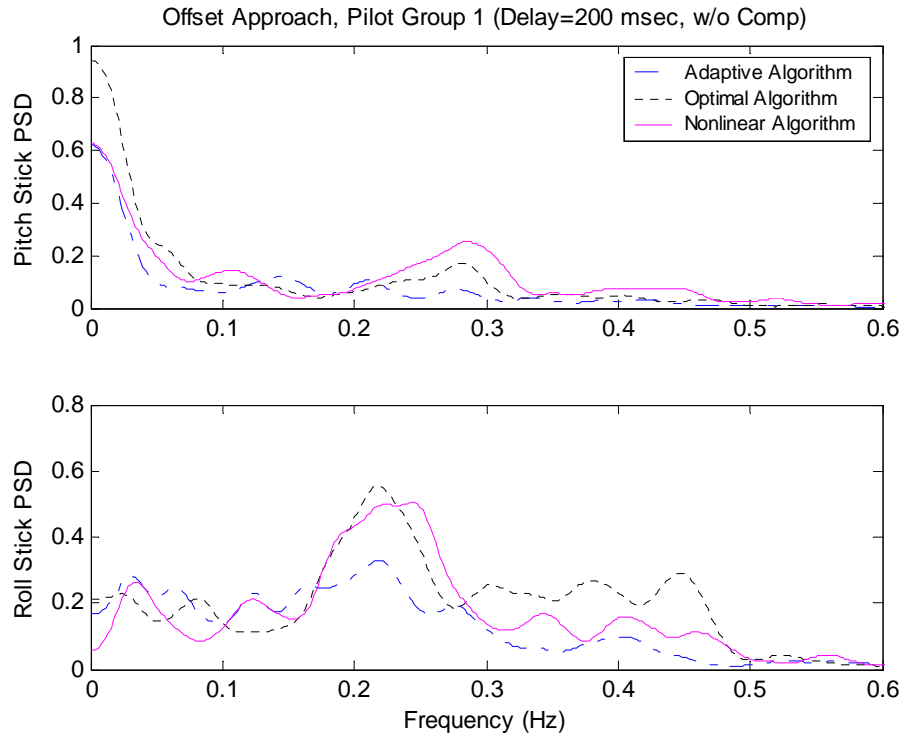


**Figure B.9. Offset Approach Average PSD, Pilot Group 1, Delay 200 msec.**

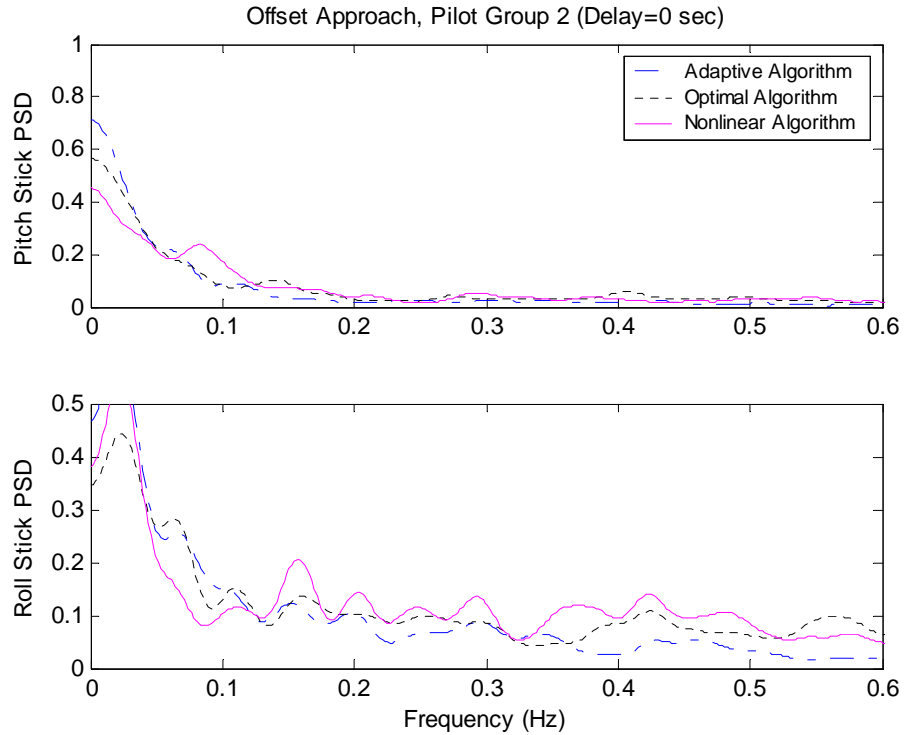


**Figure B.10. Offset Approach Average PSD, Pilot Group 2, No Delay.**

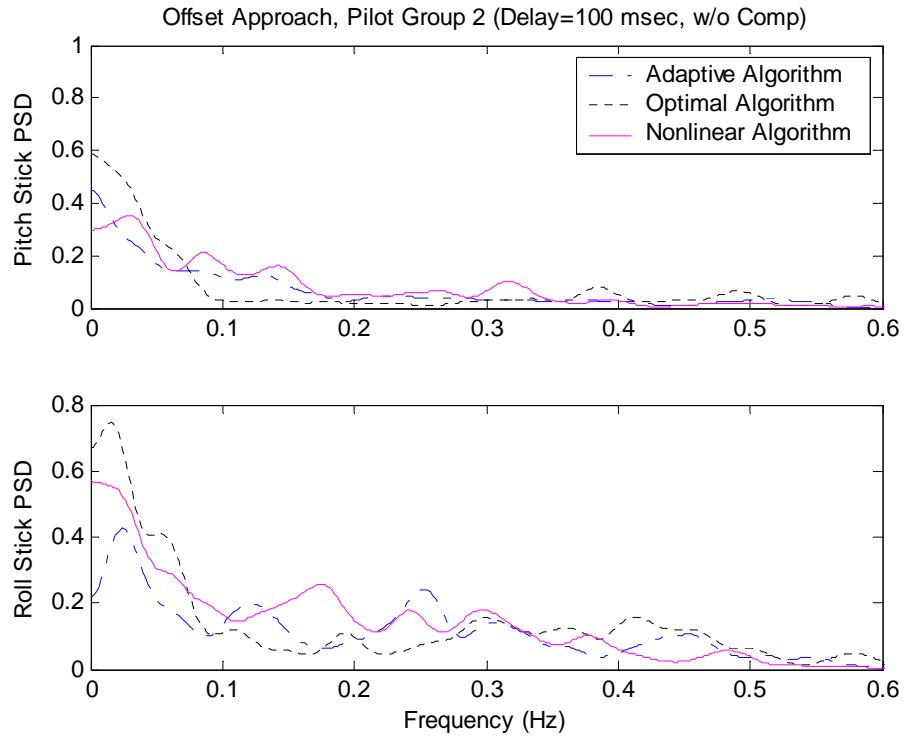


**Figure B.11. Offset Approach Average PSD, Pilot Group 2, Delay 100 msec.**

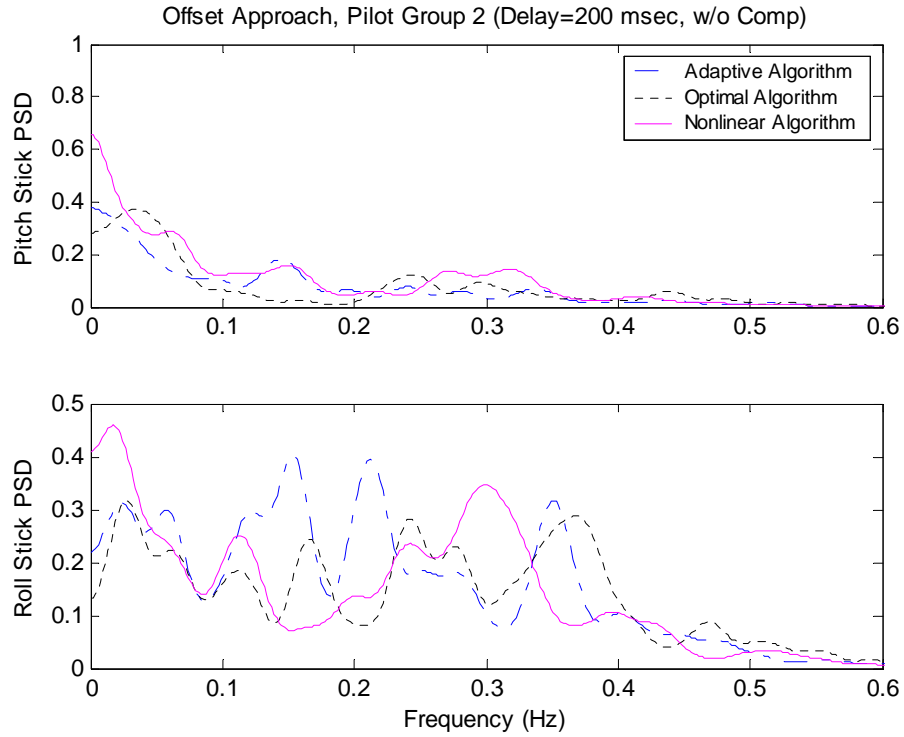


**Figure B.12. Offset Approach Average PSD, Pilot Group 2, Delay 200 msec.**

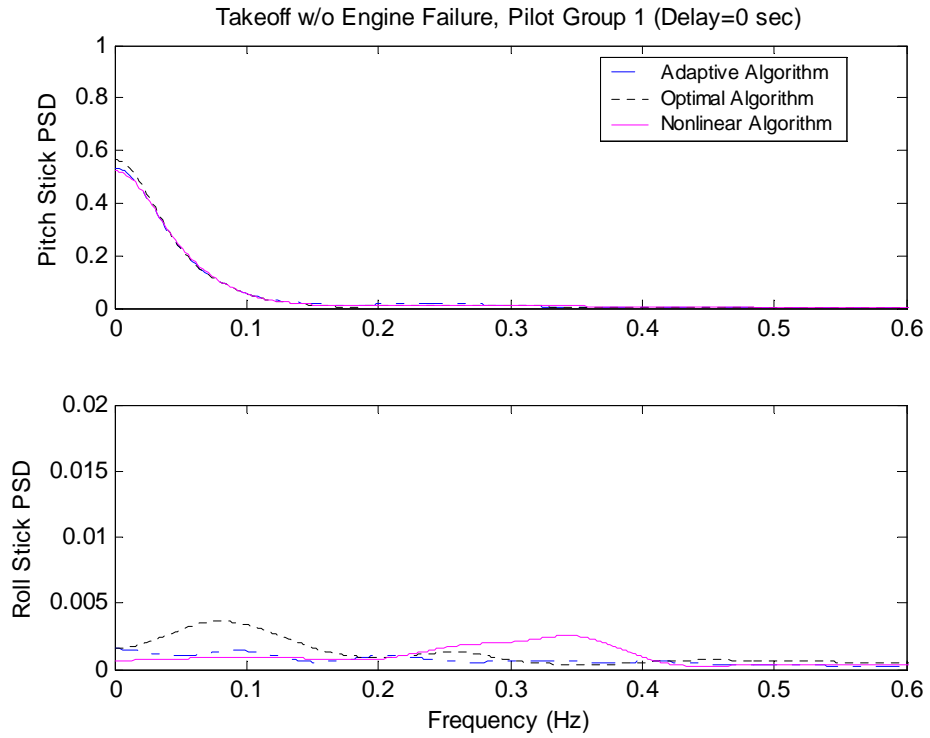


**Figure B.13. Takeoff w/o Engine Failure Average PSD, Pilot Group 1, No Delay.**

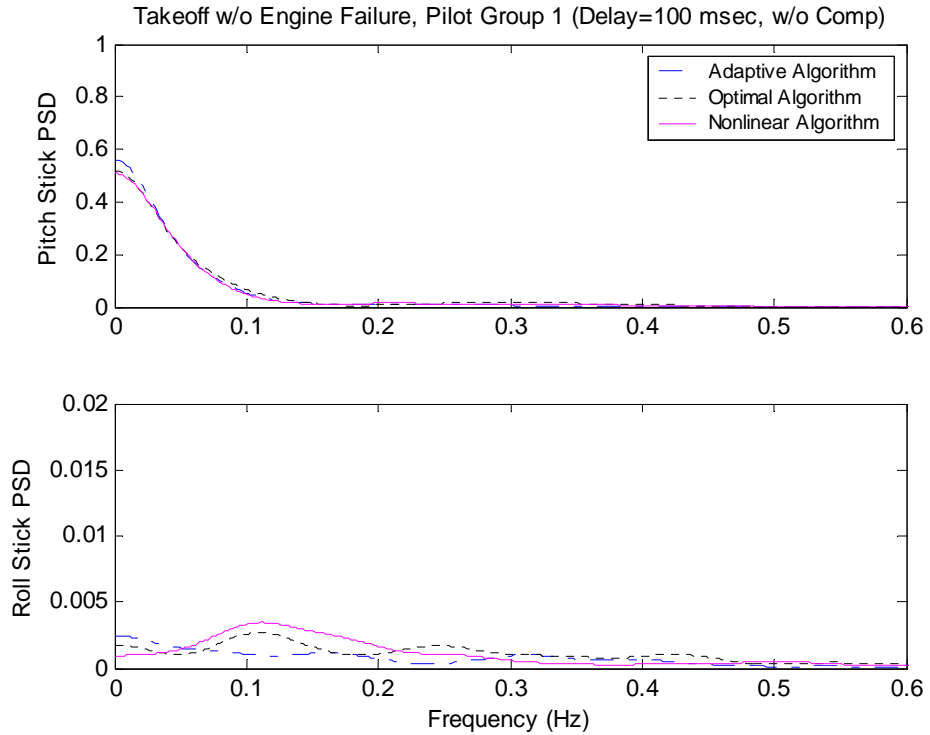


**Figure B.14. Takeoff w/o Engine Failure Average PSD, Pilot Group 1, Delay 100 msec.**

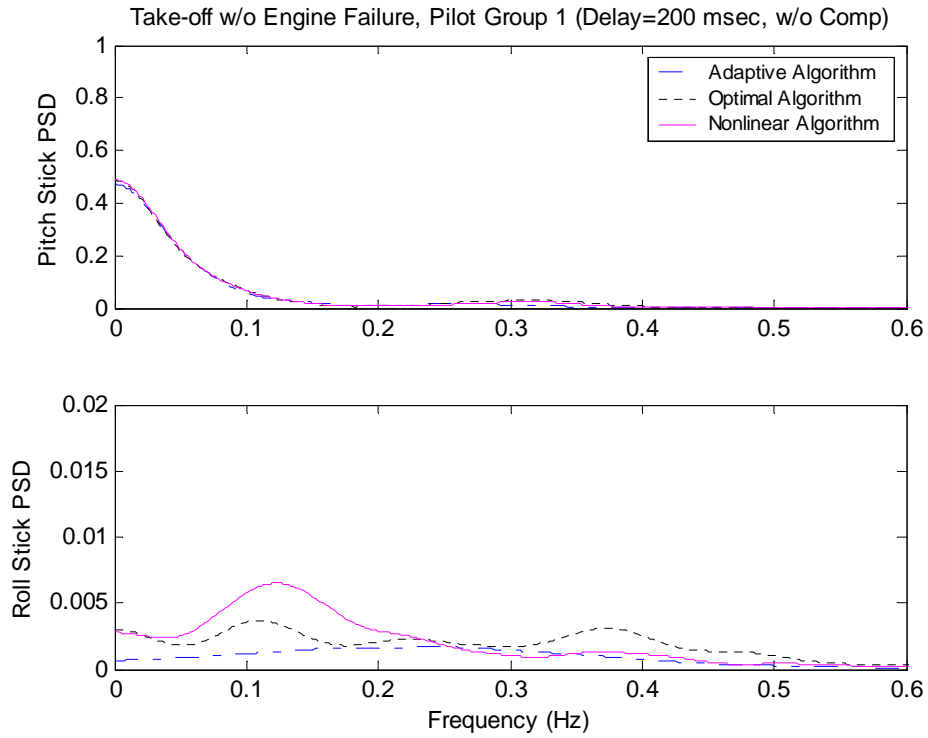


**Figure B.15. Takeoff w/o Engine Failure Average PSD, Pilot Group 1, Delay 200 msec.**

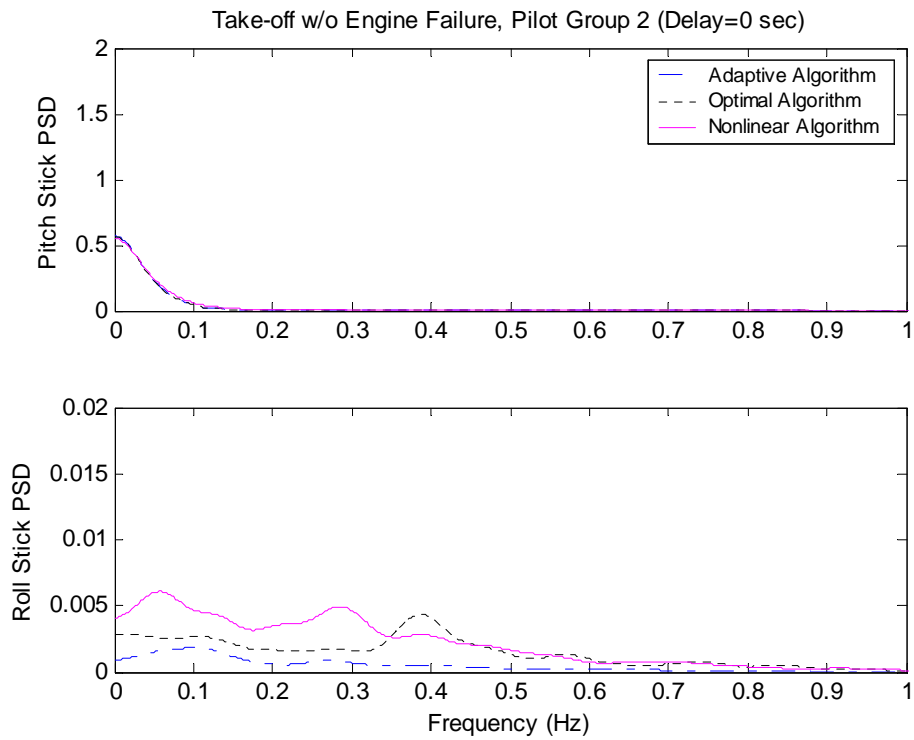


**Figure B.16. Takeoff w/o Engine Failure Average PSD, Pilot Group 2, No Delay.**

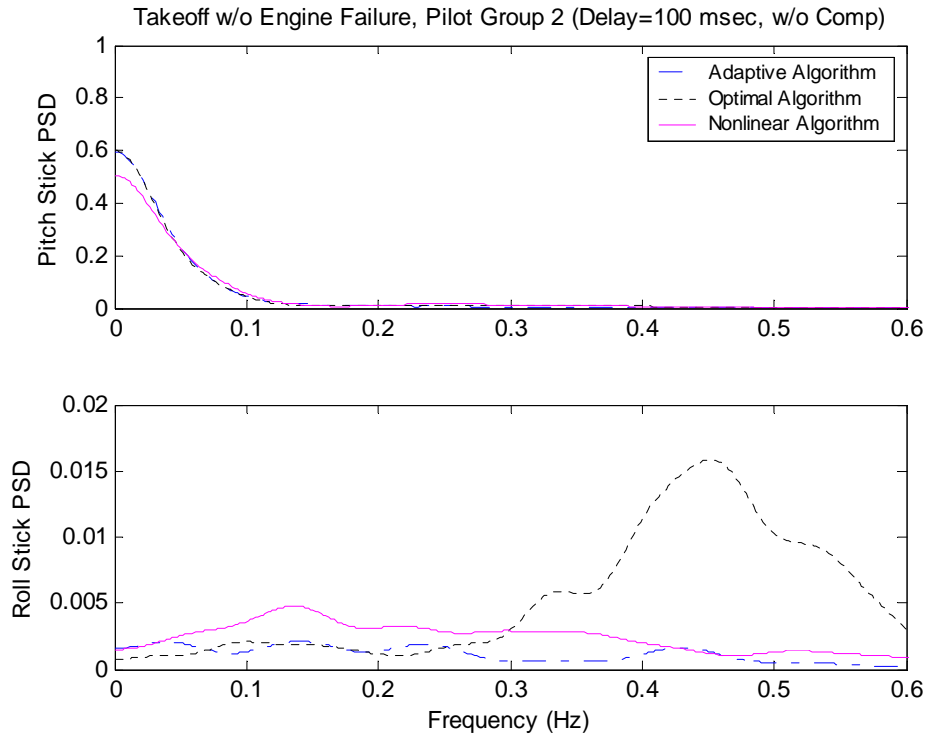


**Figure B.17. Takeoff w/o Engine Failure Average PSD, Pilot Group 2, Delay 100 msec.**

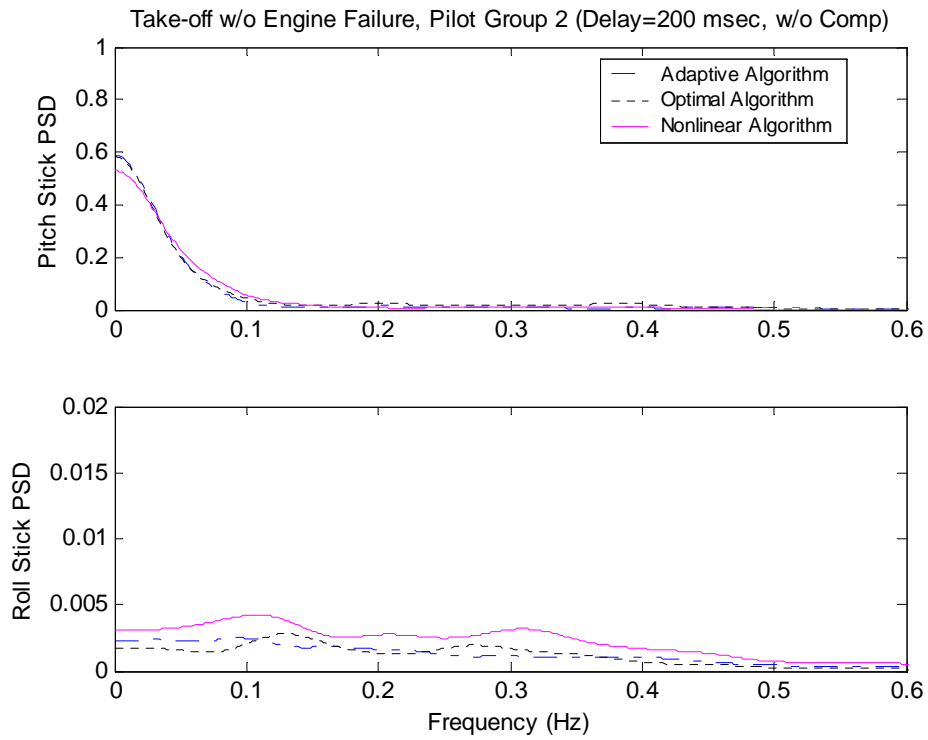


**Figure B.18. Takeoff w/o Engine Failure Average PSD, Pilot Group 2, Delay 200 msec.**

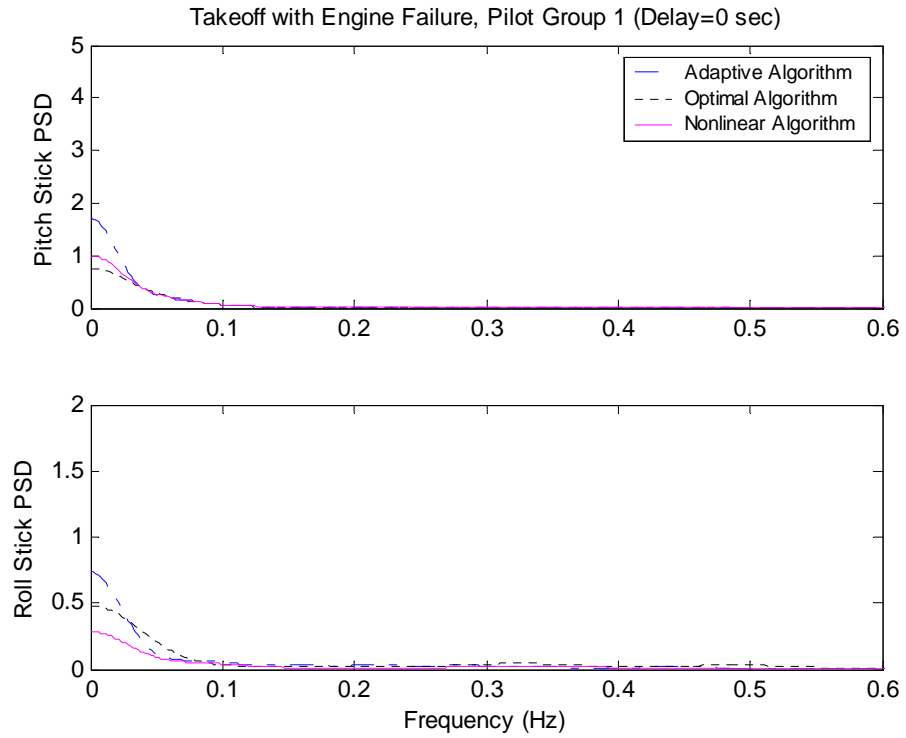


**Figure B.19. Takeoff with Engine Failure Average PSD, Pilot Group 1, No Delay.**

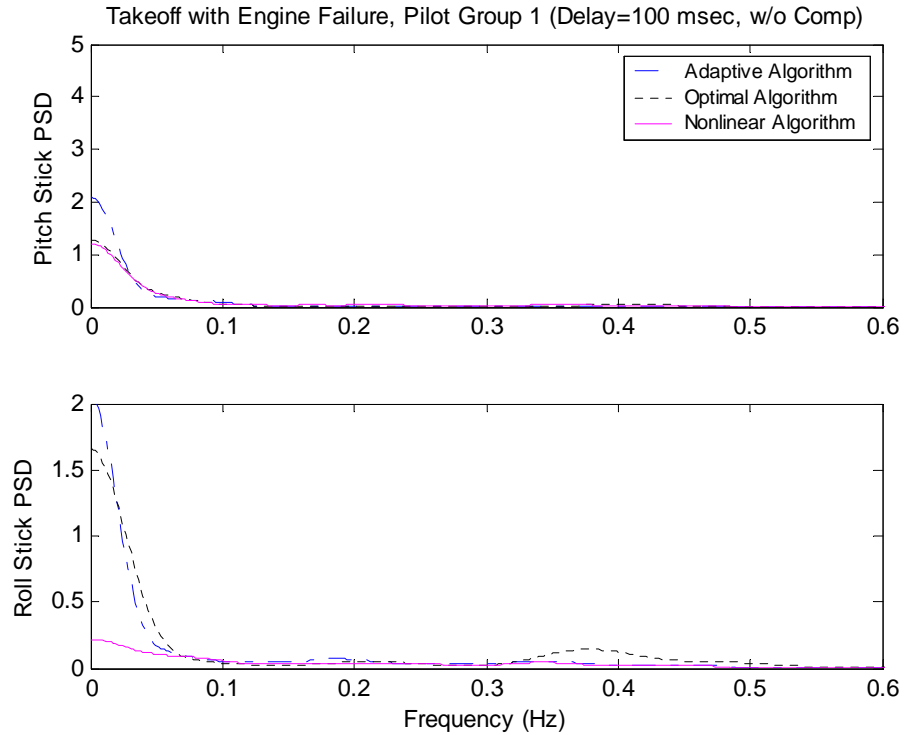


**Figure B.20. Takeoff with Engine Failure Average PSD, Pilot Group 1, Delay 100 msec.**

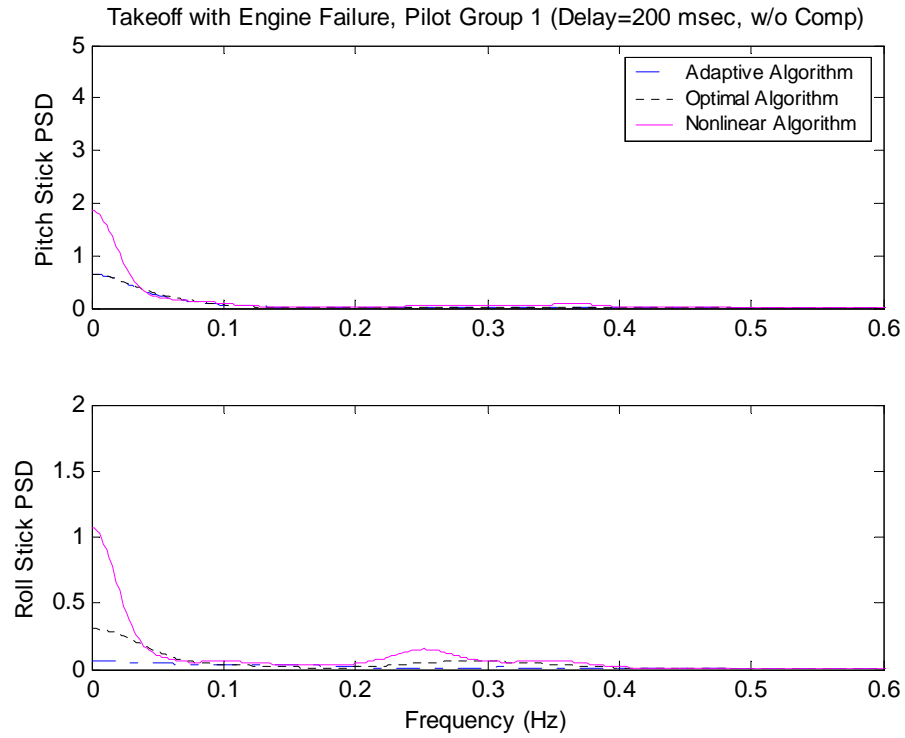


**Figure B.21. Takeoff with Engine Failure Average PSD, Pilot Group 1, Delay 200 msec.**

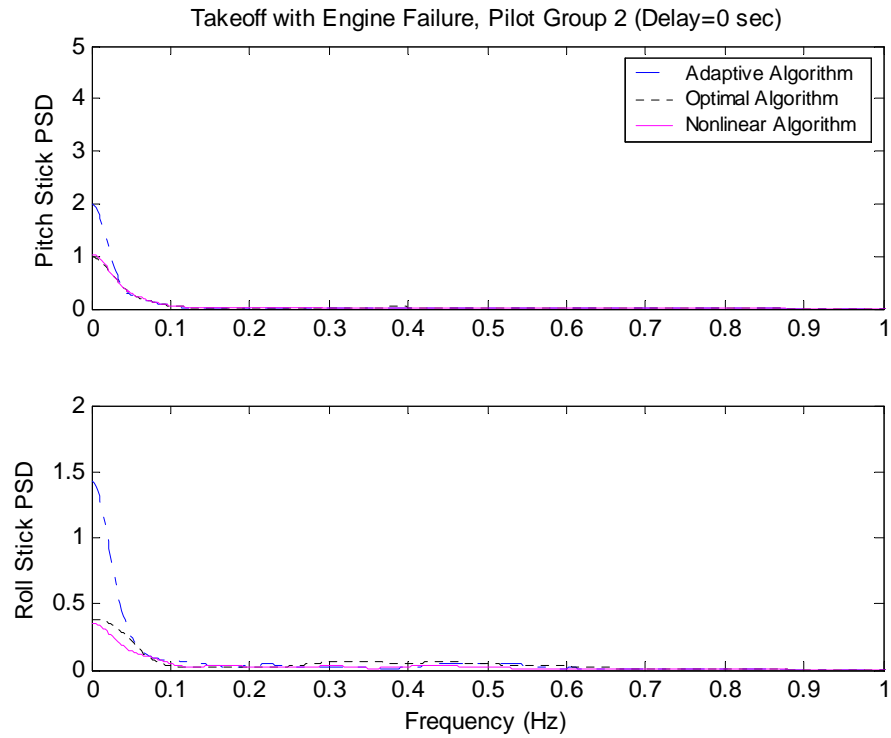


**Figure B.22. Takeoff with Engine Failure Average PSD, Pilot Group 2, No Delay.**

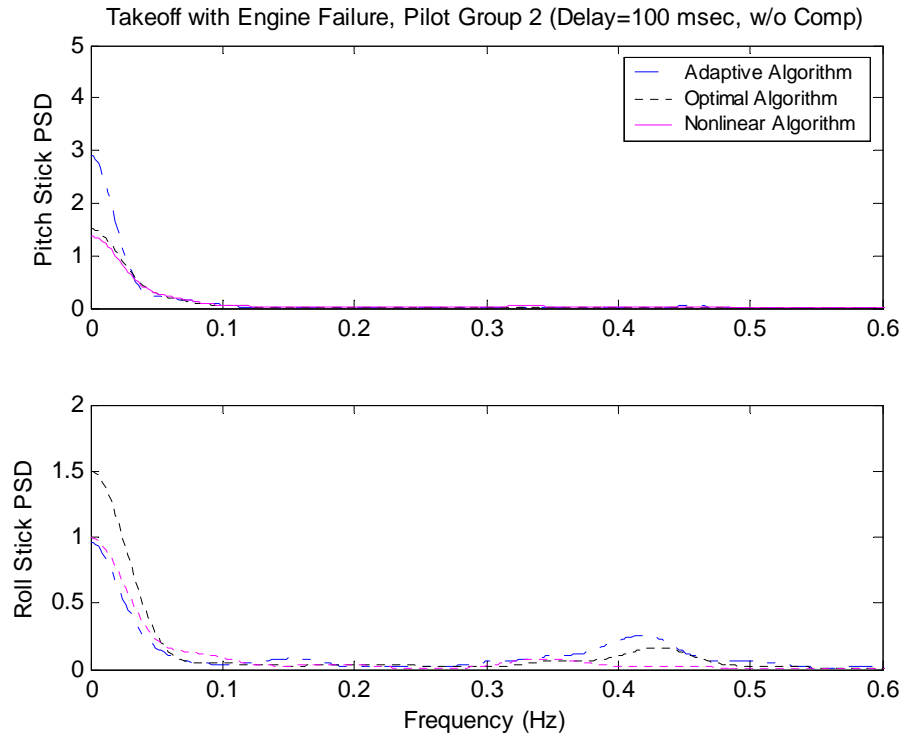


**Figure B.23. Takeoff with Engine Failure Average PSD, Pilot Group 2, Delay 100 msec.**

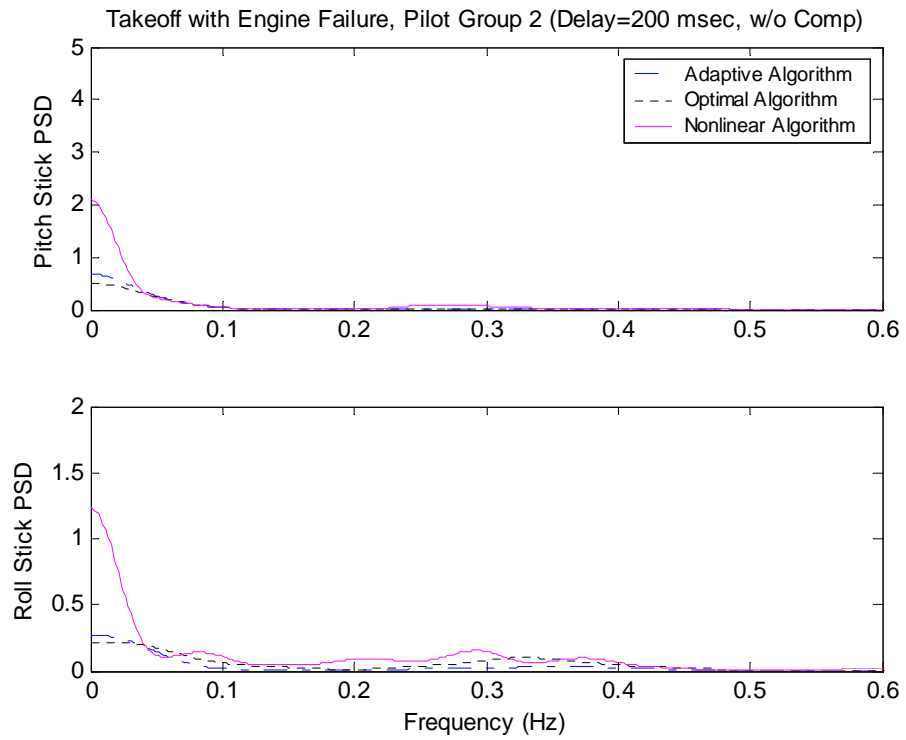


**Figure B.24. Takeoff with Engine Failure Average PSD, Pilot Group 2, Delay 200 msec.**

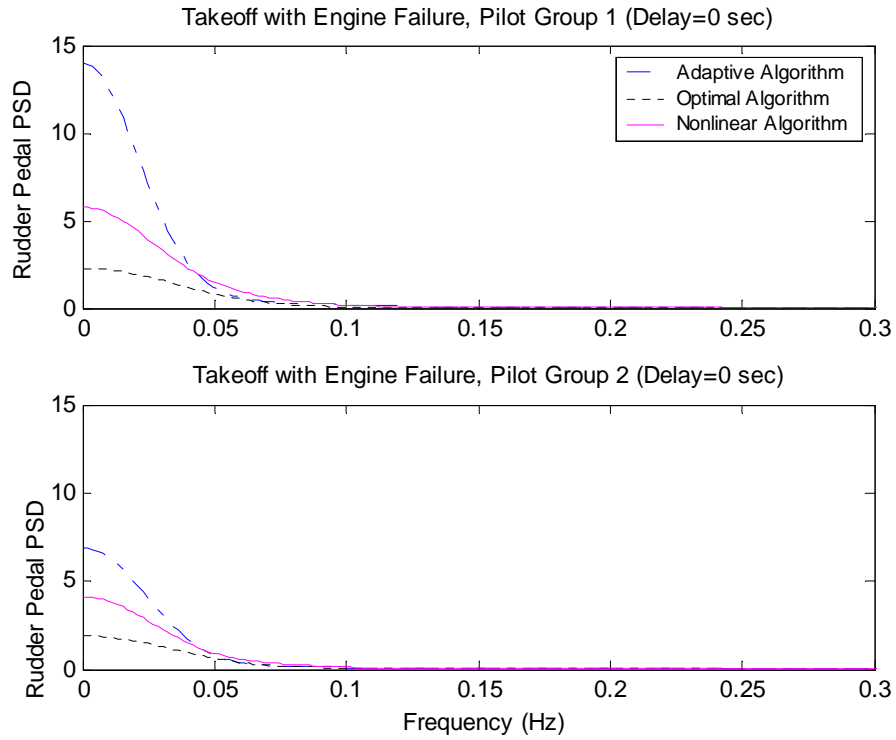


**Figure B.25. Takeoff with Engine Failure Average PSD, Rudder Pedal, No Delay.**

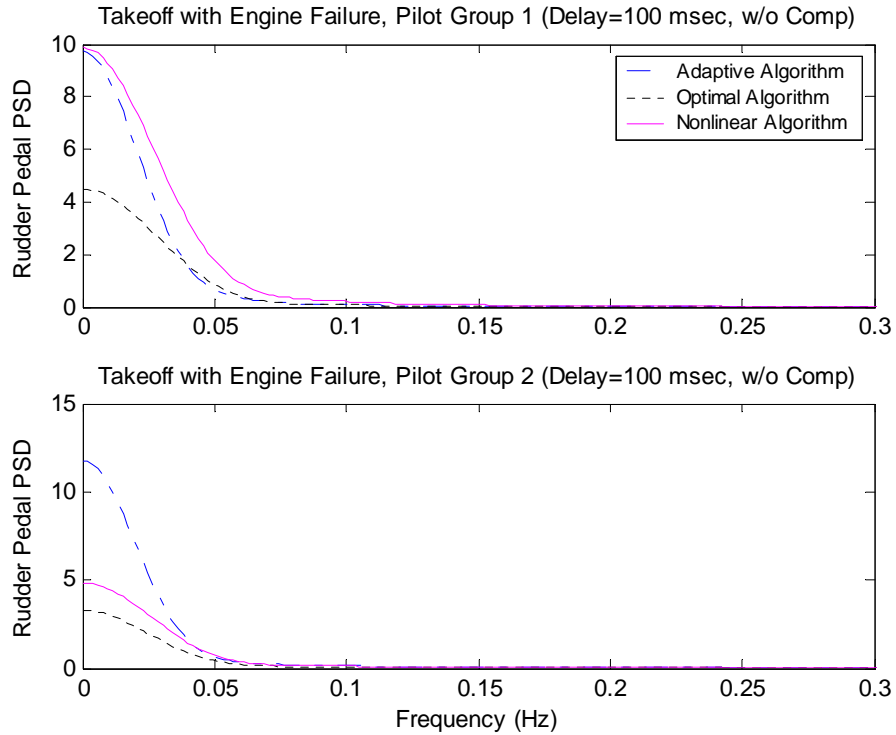


**Figure B.26. Takeoff with Engine Failure Average PSD, Rudder Pedal, Delay 100 msec.**

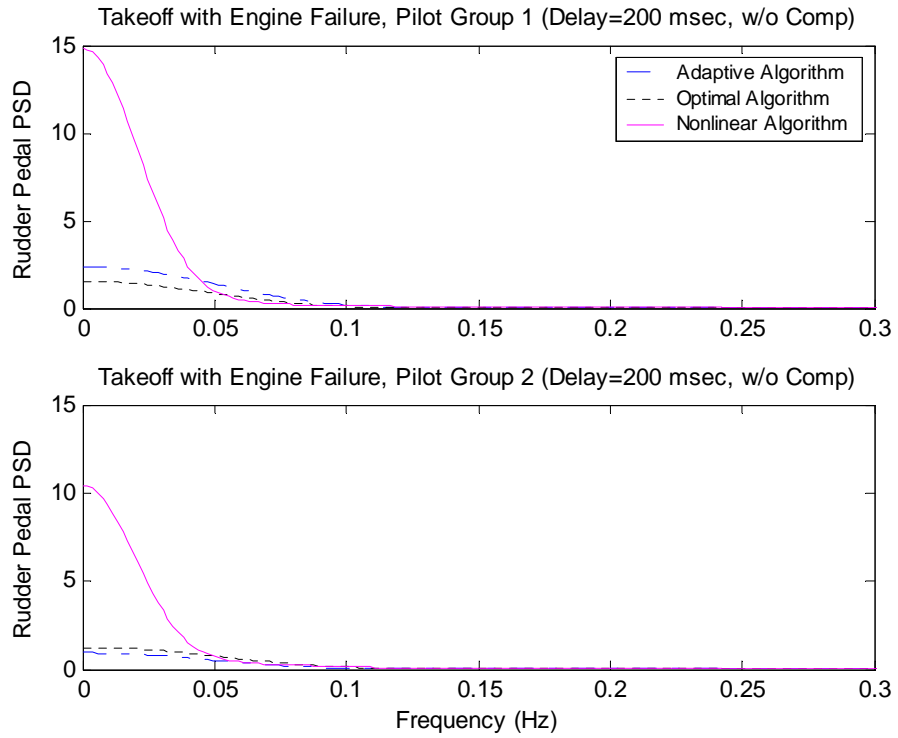


**Figure B.27. Takeoff with Engine Failure Average PSD, Rudder Pedal, Delay 200 msec.**

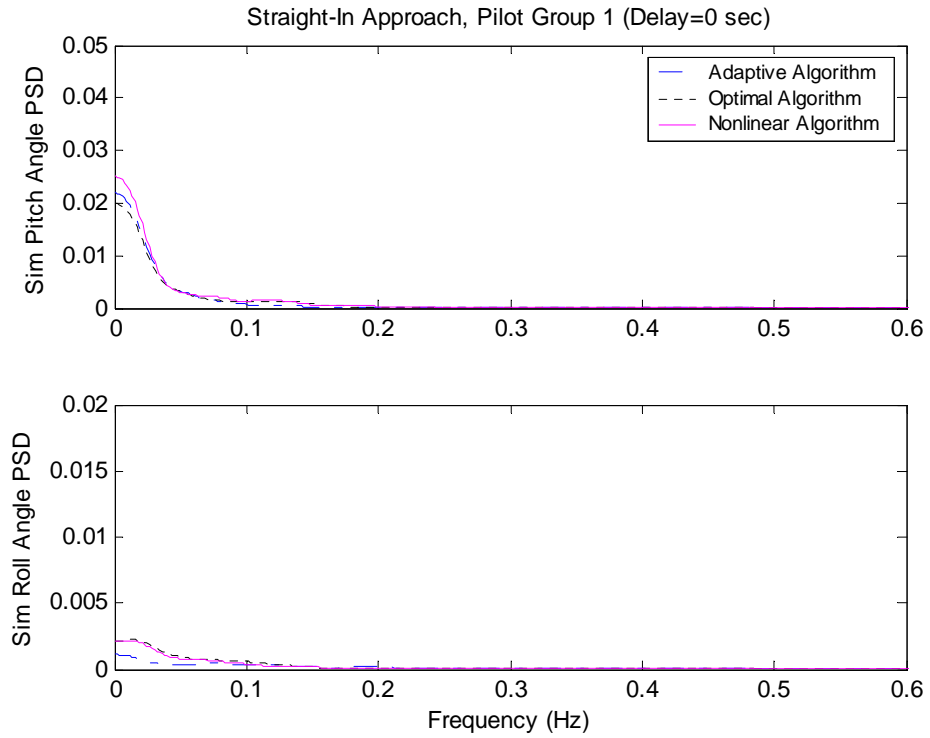


**Figure B.28. Straight-In Approach, Simulator Attitude Average PSD, Pilot Group 1.**

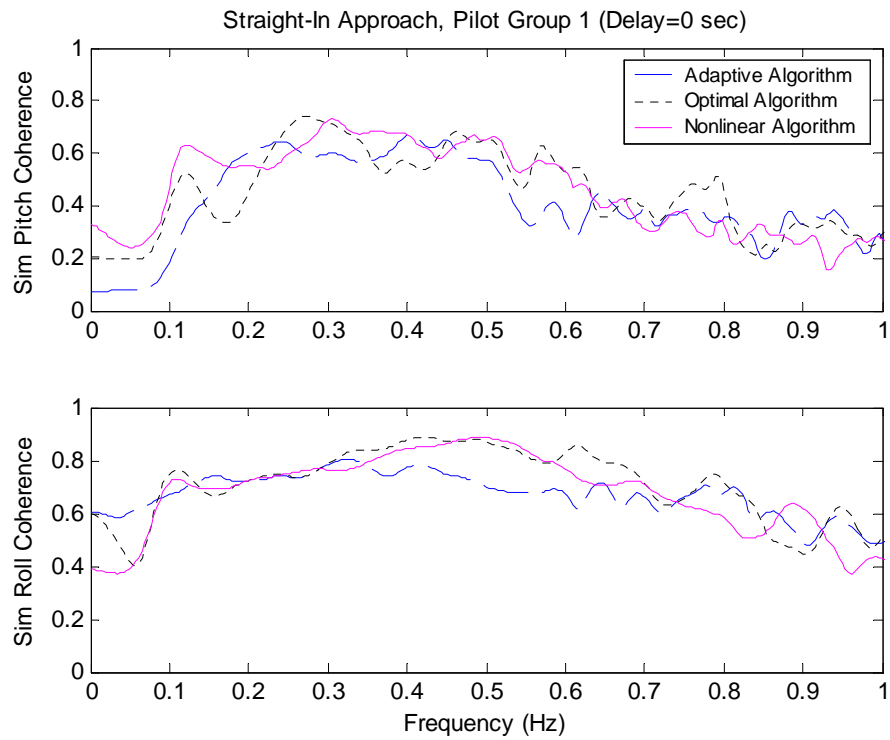


**Figure B.29. Straight-In Approach, Average Simulator Coherence, Pilot Group 1.**

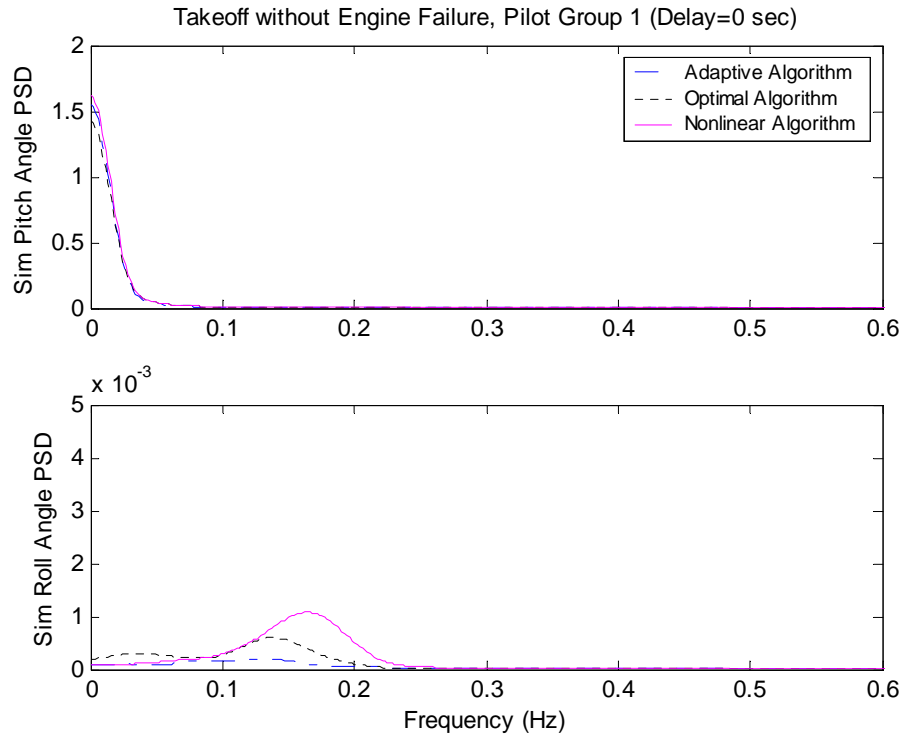


**Figure B.30. Takeoff w/o Engine Failure, Simulator Attitude Average PSD, Pilot Group 1.**

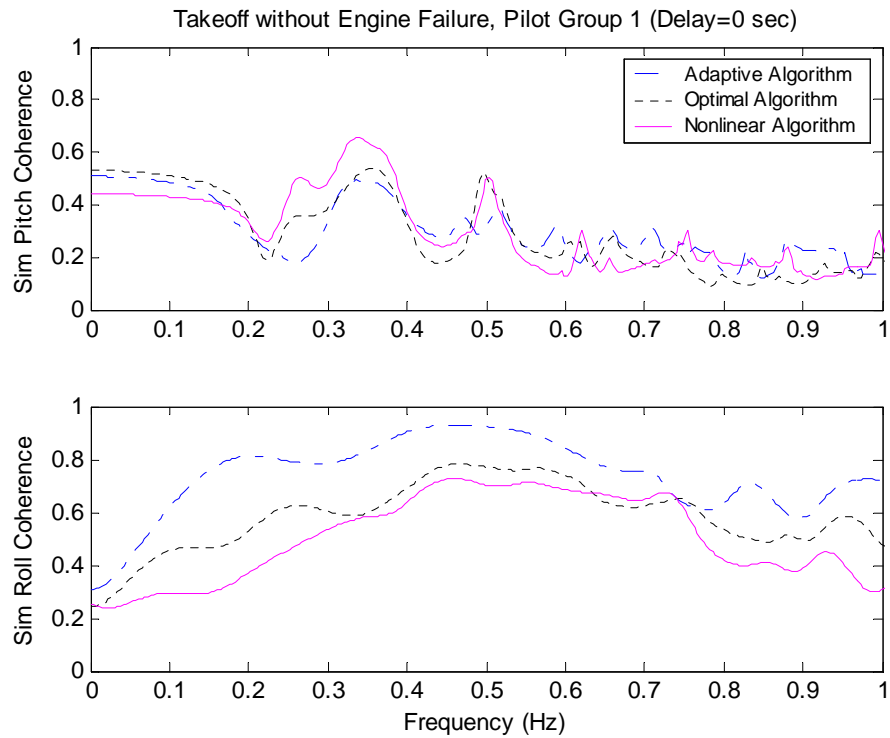


**Figure B.31. Takeoff w/o Engine Failure, Average Simulator Coherence, Pilot Group 1.**

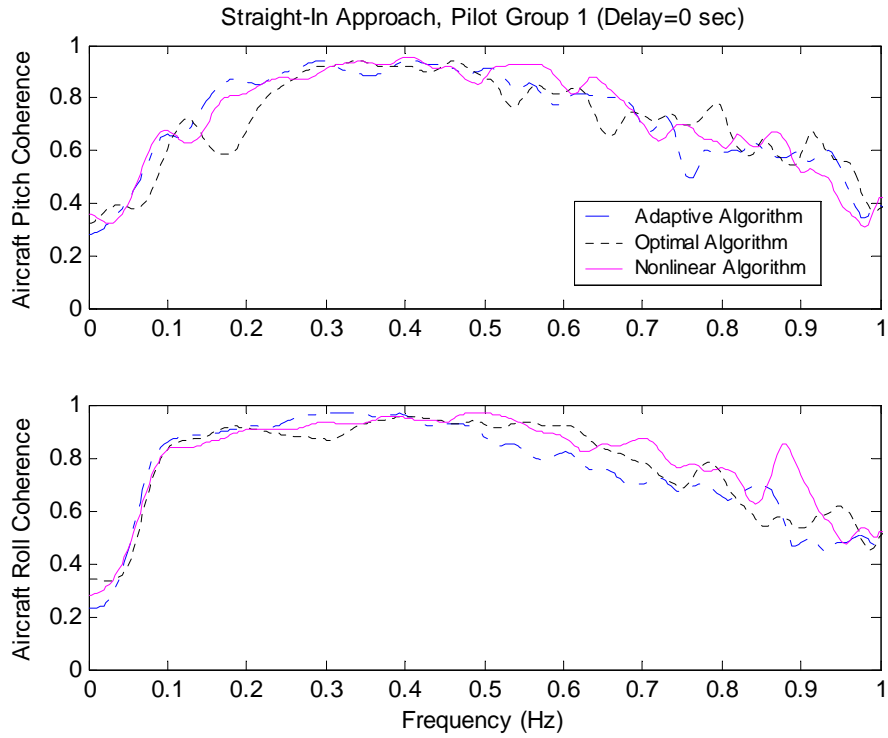


**Figure B.32. Straight-In Approach, Average Aircraft Coherence, Pilot Group 1.**

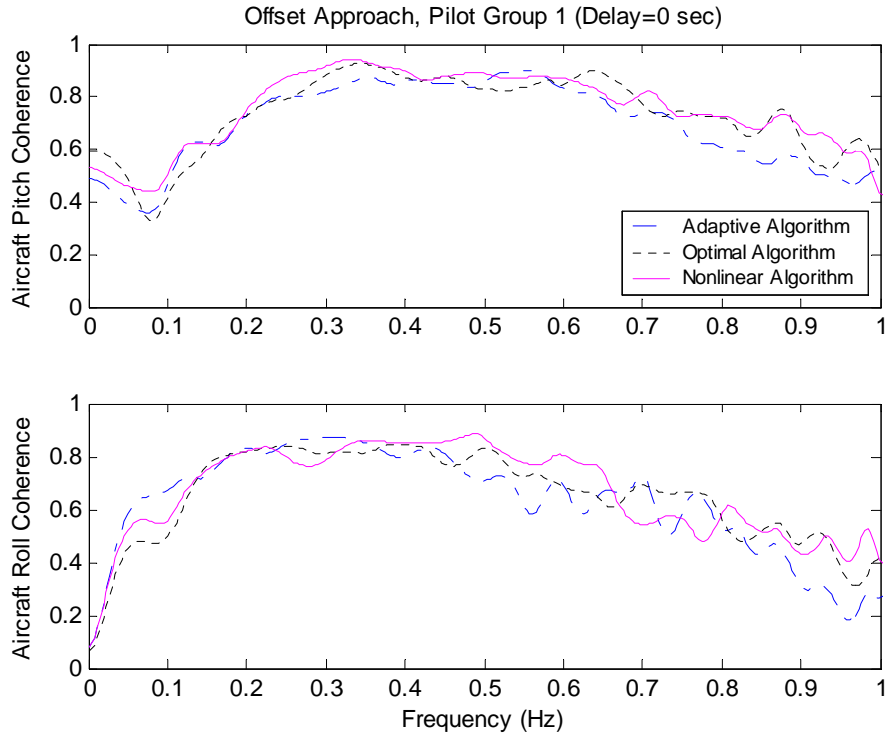


**Figure B.33. Offset Approach, Average Aircraft Coherence, Pilot Group 1.**

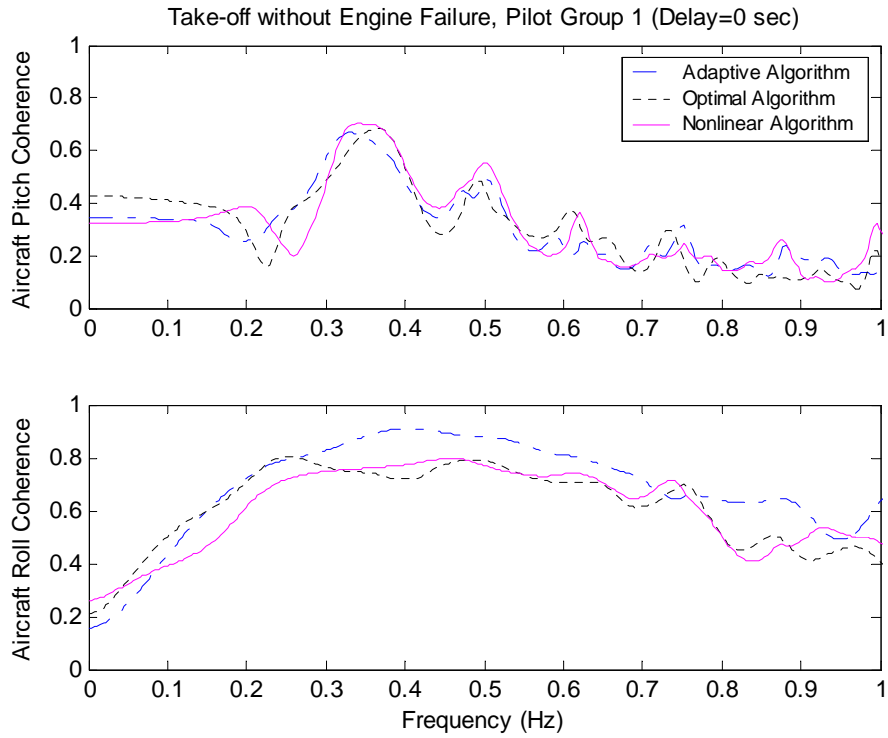


**Figure B.34. Takeoff w/o Engine Failure, Average Aircraft Coherence, Pilot Group 1.**

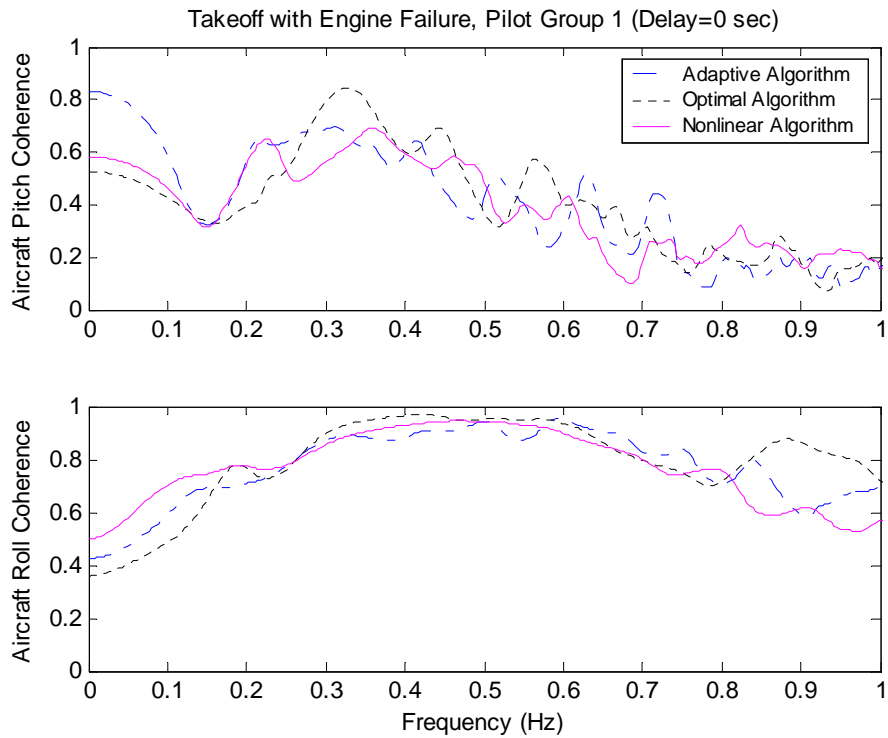


**Figure B.35. Takeoff with Engine Failure, Average Aircraft Coherence, Pilot Group 1.**

## References

- [1] Martin, D. J., Jr., *A Digital Program for Motion Washout on Langley's Six-degree-of-freedom Motion Simulator*. 1977, NASA CR-145219, NASA Langley Research Center, Hampton, VA.
- [2] Telban, R. J., and Cardullo, F. M., *Motion Cueing Algorithm Development: Human-Centered Linear and Nonlinear Algorithms*. 2005, NASA CR-2005-213747, NASA Langley Research Center, Hampton, VA.
- [3] Guo, L., Cardullo, F. M., Telban, R. J., Houck, J. A., and Kelly, L. C. *The Results of a Simulator Study to Determine the Effects on Pilot Performance of Two Different Motion Cueing Algorithms and Various Delays, Compensated and Uncompensated*. *AIAA Modeling and Simulation Technologies Conference*. 2003. Austin, TX.
- [4] Hart, S. G., and Staveland, L. E., *Development of a Multi-dimensional Workload Rating Scale: Results of Empirical and Theoretical Research*, in *Human Mental Workload*, P.A. Hancock, and Meshkati, N., Editor, 1988, Elsevier: Amsterdam, The Netherlands.
- [5] Parrish, R. V., Dieudonne, J. E., and Martin, D. J., Jr., *Motion Software for a Synergistic Six-Degree-of-Freedom Motion Base*. 1973, NASA TN D-7350, NASA Langley Research Center, Hampton, VA.
- [6] Telban, R. J., Cardullo, F. M., and Houck, J. A. *Developments in Human Centered Cueing Algorithms for Control of Flight Simulator Motion Systems*. *AIAA Modeling and Simulation Technologies Conference*. 1999. Portland. OR.
- [7] Ham, F. M., and Collins, E. G. *A Neurocomputing Approach for Solving the Algebraic Matrix Riccati Equation*. *IEEE International Conference on Neural Networks*. 1996.
- [8] Wu, W., *Development of Cueing Algorithm for the Control of Simulator Motion Systems*, 1997, M.S. Thesis, State University of New York at Binghamton, Binghamton, NY.
- [9] Reid, L.D., and Robinson, P. A., *Augmenting Flight Simulator Motion Response to Turbulence*. *Journal of Aircraft*, 1989. **27**(4): p. 306-311.
- [10] Telban, R. J., and Cardullo, F. M., and Kelly, L. C., *Motion Cueing Algorithm Development: New Motion Cueing Program Implementation and Tuning*. 2005, NASA CR-2005-213746, NASA Langley Research Center, Hampton, VA.
- [11] Levison, W. H., Baron, S., and Kleinman, D. L., *A Model for Human Controller Remnant*. *IEEE Transactions on Man-Machine Systems*, 1969. **10**(4): p. 101-108.
- [12] Ljung, L., *System Identification Theory for the User*. 1999, Upper Saddle River, NJ: Prentice-Hall, Inc.
- [13] Go, T. H., Burki-Cohen, J., Chung, W. W., Schroeder, J. A., Saillant, G., Jacobs, S., and Longridge, T. *The Effects of Simulated Hexapod Motion on Airline Pilot Recurrent Training and Evaluation*. *AIAA Modeling and Simulation Technologies Conference*. 2003. Austin, TX.
- [14] Smith, R. M. *A Description of the Cockpit Motion Facility and the Research Flight Deck Simulator*. *AIAA Modeling and Simulation Technologies Conference*. 2000. Denver, CO.

**REPORT DOCUMENTATION PAGE**

*Form Approved  
OMB No. 0704-0188*

The public reporting burden for this collection of information is estimated to average 1 hour per response, including the time for reviewing instructions, searching existing data sources, gathering and maintaining the data needed, and completing and reviewing the collection of information. Send comments regarding this burden estimate or any other aspect of this collection of information, including suggestions for reducing this burden, to Department of Defense, Washington Headquarters Services, Directorate for Information Operations and Reports (0704-0188), 1215 Jefferson Davis Highway, Suite 1204, Arlington, VA 22202-4302. Respondents should be aware that notwithstanding any other provision of law, no person shall be subject to any penalty for failing to comply with a collection of information if it does not display a currently valid OMB control number.  
**PLEASE DO NOT RETURN YOUR FORM TO THE ABOVE ADDRESS.**

<b>1. REPORT DATE (DD-MM-YYYY)</b> 01-05-2005		<b>2. REPORT TYPE</b> Contractor Report		<b>3. DATES COVERED (From - To)</b>	
<b>4. TITLE AND SUBTITLE</b> Motion Cueing Algorithm Development: Piloted Performance Testing of the Cueing Algorithms				<b>5a. CONTRACT NUMBER</b>	
				<b>5b. GRANT NUMBER</b>	
				<b>5c. PROGRAM ELEMENT NUMBER</b>	
<b>6. AUTHOR(S)</b> Telban, Robert J.; Cardullo, Frank M.; and Kelly, Lon C.				<b>5d. PROJECT NUMBER</b> L70823D	
				<b>5e. TASK NUMBER</b>	
				<b>5f. WORK UNIT NUMBER</b> 23-090-70-10	
<b>7. PERFORMING ORGANIZATION NAME(S) AND ADDRESS(ES)</b> State University of New York - Binghamton Binghamton, NY 13902-6000 Unisys Corporation Hampton, VA 23666				<b>8. PERFORMING ORGANIZATION REPORT NUMBER</b>	
<b>9. SPONSORING/MONITORING AGENCY NAME(S) AND ADDRESS(ES)</b> National Aeronautics and Space Administration Langley Research Center Hampton, VA 23681-2199				<b>10. SPONSOR/MONITOR'S ACRONYM(S)</b>  NASA	
				<b>11. SPONSOR/MONITOR'S REPORT NUMBER(S)</b>  NASA/CR-2005-213748	
<b>12. DISTRIBUTION/AVAILABILITY STATEMENT</b> Unclassified - Unlimited Subject Category 54 Availability: NASA CASI (301) 621-0390					
<b>13. SUPPLEMENTARY NOTES</b> Prepared by the State University of New York - Binghamton for NASA Langley Research Center under subcontract to Unisys Corporation. NASA Langley Research Center Technical Monitor: Jacob A. Houck. An electronic version can be found at <a href="http://ntrs.nasa.gov">http://ntrs.nasa.gov</a>					
<b>14. ABSTRACT</b> The relative effectiveness in simulating aircraft maneuvers with motion cueing algorithms was assessed with an eleven-subject piloted performance evaluation conducted on the NASA Langley Visual Motion Simulator. In addition to the NASA adaptive algorithm, two new cueing algorithms were evaluated: the optimal algorithm and the nonlinear algorithm. The test maneuvers included a straight-in approach with a rotating wind vector, an offset approach with severe turbulence, and a takeoff both with and without engine failure after liftoff. The maneuvers were executed with each cueing algorithm with added visual display delay conditions ranging from zero to 200 msec. Two methods, the quasi-objective NASA Task Load Index (TLX), and power spectral density analysis of pilot control, were used to assess pilot workload. TLX analysis reveals, in most cases, less workload and variation among pilots with the nonlinear algorithm. Control input analysis shows pilot-induced oscillations on a straight-in approach were less prevalent compared to the optimal algorithm. Augmented turbulence cues increased workload on an offset approach that the pilots deemed more realistic compared to the NASA adaptive algorithm. The takeoff with engine failure showed the least roll activity for the nonlinear algorithm, with the least rudder pedal activity for the optimal algorithm.					
<b>15. SUBJECT TERMS</b> Flight Simulation, Simulators, Motion Systems, Cueing Algorithms, Motion Perception					
<b>16. SECURITY CLASSIFICATION OF:</b>			<b>17. LIMITATION OF ABSTRACT</b>	<b>18. NUMBER OF PAGES</b>	<b>19a. NAME OF RESPONSIBLE PERSON</b>
<b>a. REPORT</b>	<b>b. ABSTRACT</b>	<b>c. THIS PAGE</b>			STI Help Desk (email: <a href="mailto:help@sti.nasa.gov">help@sti.nasa.gov</a> )
U	U	U	UU	102	<b>19b. TELEPHONE NUMBER (Include area code)</b> (301) 621-0390